# $d_{x^2-y^2}$-wave superconductivity and the Hubbard model

N. BULUT

Department of Physics, Koç University
Sariyer, 80910 Istanbul, Turkey

### Abstract

The numerical studies of $d_{x^2-y^2}$-wave pairing in the two-dimensional (2D) and the 2-leg Hubbard models are reviewed. For this purpose, the results obtained from the determinantal Quantum Monte Carlo and the density-matrix renormalization-group calculations are presented. These are calculations which were motivated by the discovery of the high-$T_c$ cuprates. In this review, the emphasis is placed on the microscopic many-body processes which are responsible for the $d_{x^2-y^2}$-wave pairing correlations observed in the 2D and the 2-leg Hubbard models. In order to gain insight into these processes, the results on the effective pairing interaction as well as the magnetic, density and the single-particle excitations will be reviewed. In addition, comparisons will be made with the other numerical approaches to the Hubbard model and the numerical results on the $t$-$J$ model. The results reviewed here indicate that an effective pairing interaction which is repulsive at $(\pi, \pi)$ momentum transfer and enhanced single-particle spectral weight near the $(\pi, 0)$ and $(0, \pi)$ points of the Brillouin zone create optimum conditions for $d_{x^2-y^2}$-wave pairing. These are two effects which act to enhance the $d_{x^2-y^2}$-wave pairing correlations in the Hubbard model. Finding additional ways is an active research problem.

# Contents

# 1   Introduction

Since the discovery of high-temperature superconductivity in the layered cuprates in 1986 [Bednorz and Müller 1986], it has been established that the superconducting order parameter has the $d_{x^2-y^2}$-wave symmetry in a number of these materials [Schrieffer 1994, Scalapino 1995, van Harlingen 1995, Tsuei and Kirtley 2000]. This is important, because the $d_{x^2-y^2}$-wave symmetry of the order parameter suggests the possibility of an electronically mediated pairing mechanism. Perhaps, the simplest model used for modelling the low-energy electronic correlations of the layered cuprates is the two-dimensional (2D) Hubbard model. Within this context, the nature of the pairing correlations in the Hubbard model as well as the nature of its low-lying electronic excitations has received considerable attention.

In 1987 Anderson suggested that the 2D Hubbard model is relevant to the cuprates [Anderson 1987]. However, even today questions remain about this model. In this article, what has been learned about the physical properties of the 2D and the 2-leg Hubbard models from the numerical studies will be reviewed. The emphasis will be placed on the $d_{x^2-y^2}$ pairing correlations seen in these models and their microscopic origin. The implications of these calculations for the $d_{x^2-y^2}$-wave pairing in the high-$T_c$ cuprates is of current interest. In particular, one is interested in knowing whether the $d_{x^2-y^2}$-wave superconducting order could exist in the ground state of the 2D Hubbard model, and, if it does, whether it would have sufficient strength to explain the superconducting transition temperatures as high as those seen in the cuprates. There is also much interest in finding ways of enhancing the strength of the $d_{x^2-y^2}$-wave pairing correlations observed in the Hubbard model. Within the past ten to fifteen years, the determinantal Quantum Monte Carlo (QMC) and the density-matrix renormalization-group (DMRG) techniques have been used to address these questions. These numerical studies are the subject of this review article.

For the 2D Hubbard model, the QMC data on the magnetic, charge and the single-particle excitations will be presented. In order to investigate the pairing correlations, the QMC data on the irreducible particle-particle interaction and the solutions of the particle-particle Bethe-Salpeter equation will be shown. Using the DMRG method, the equal-time pair-field correlation function has been calculated in the ground state of the 2-leg Hubbard ladder. These DMRG data along with the QMC results on the 2-leg ladder will be shown and compared with each other. In addition, these results will be compared with the numerical studies of the $t$-$J$ model.

Figure 1.1 shows a schematic drawing of the $CuO_2$ plane of the cuprates consisting of the one-electron $Cu(3d_{x^2-y^2})$ and $O(p_x, p_y)$ orbitals that give rise to the band in which the $d_{x^2-y^2}$-wave superconducting pairs form. In an electronic model of the $CuO_2$ plane, there would be an onsite Coulomb repulsion at the $Cu(3d_{x^2-y^2})$ and the $O(p_x, p_y)$ orbitals and one-electron hopping matrix elements between the neighbouring Cu-O and the O-O orbitals as well as longer-range hoppings and Coulomb interactions. A simplified approach is to use the single-band Hubbard model on the 2D square lattice which has an onsite Coulomb repulsion and one-electron hopping matrix elements between the nearest-neighbour sites, as illustrated in Fig. 1.2(a). To some extent, this is motivated by the notion that the nonperturbative effects due to the onsite Coulomb repulsion will dominate at low temperatures and low energies. Extensive numerical calculations have been carried out for studying the properties of the one-band 2D Hubbard model. Another model which has proven useful for studying $d_{x^2-y^2}$-wave pairing is the 2-leg Hubbard ladder illustrated in Fig. 1.2(b). This model has an onsite Coulomb repulsion $U$ and the intrachain and interchain hopping matrix elements $t$ and $t_\perp$, respectively. The 2-leg Hubbard ladder is an important model where the pairing correlations can be studied in detail in the ground state for systems with up to 32 rungs. Here, the numerical results on the 2D and the 2-leg Hubbard models will be used to discuss the nature of the $d_{x^2-y^2}$-wave
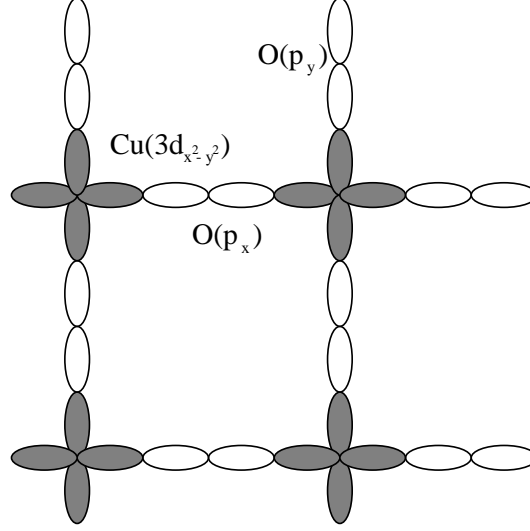
Figure 1.1: Schematic drawing of the CuO$_2$ lattice consisting of the one-electron Cu($3d_{x^2-y^2}$) and the O($p_x, p_y$) orbitals.

pairing found in the CuO$_2$ layers of the high-$T_c$ cuprates.

The Hubbard model was introduced for describing the Coulomb correlation effects in the $d$-bands of the transition metals, which show both band-like and atomic-like behaviour [Hubbard 1963]. The Hubbard Hamiltonian has a one-body kinetic term and an interaction term which represents the onsite Coulomb repulsion when two electrons occupy the same orbital. In spite of studies covering four decades, questions remain about the Hubbard model. In two dimensions, the Hubbard Hamiltonian with only nearest-neighbor hopping is given by

$$H = -t \sum_{\langle i,j \rangle, \sigma} (c_{i\sigma}^\dagger c_{j\sigma} + c_{j\sigma}^\dagger c_{i\sigma}) + U \sum_i n_{i\sigma} n_{i-\sigma} - \mu \sum_{i\sigma} n_{i\sigma}, \tag{1.1}$$

where the sum over $i$ and $j$ is done over the nearest-neighbour sites on a square lattice. The one-electron hopping matrix element is $t$, the onsite Coulomb repulsion is $U$ and the chemical potential $\mu$ is used for controlling the electron occupation in the grand canonical ensemble. Here, $c_{i\sigma}^\dagger$ ($c_{i\sigma}$) creates (annihilates) an electron of spin $\sigma$ at site $i$ and $n_{i\sigma} = c_{i\sigma}^\dagger c_{i\sigma}$ is the occupation number of electrons with spin $\sigma$ at site $i$. In addition to the 2D Hubbard model, the numerical results on the 2-leg Hubbard ladder with anisotropic hopping will be reviewed. In this case, the Hamiltonian is

$$H = -t \sum_{i,\lambda,\sigma} (c_{i,\lambda,\sigma}^\dagger c_{i+1,\lambda,\sigma} + c_{i+1,\lambda,\sigma}^\dagger c_{i,\lambda,\sigma}) - t_\perp \sum_{i,\sigma} (c_{i,1,\sigma}^\dagger c_{i,2,\sigma} + c_{i,2,\sigma}^\dagger c_{i,1,\sigma})$$
$$+ U \sum_{i,\lambda} n_{i,\lambda,\sigma} n_{i,\lambda,-\sigma} - \mu \sum_{i,\lambda,\sigma} n_{i,\lambda,\sigma}, \tag{1.2}$$

where $t$ is the hopping matrix element parallel to the chains and $t_\perp$ is the inter-chain hopping, as illustrated in Fig. 1.2(b). The operators $c_{i,\lambda,\sigma}^\dagger$ create an electron of spin $\sigma$ at site $i$ of the $\lambda$'th leg, and $n_{i,\lambda,\sigma} = c_{i,\lambda,\sigma}^\dagger c_{i,\lambda,\sigma}$ is the electron number operator with spin $\sigma$ at site $(i, \lambda)$.

The QMC and the DMRG are powerful numerical methods, which have been developed for studying strongly-correlated systems such as the Hubbard model. These techniques allow for the possibility to determine whether superconductivity exists in the ground state of an interacting
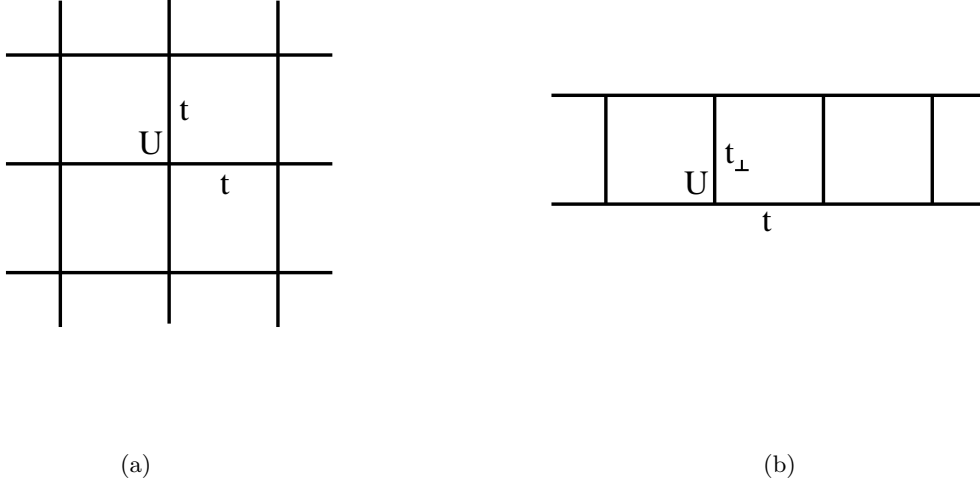
(a)                                    (b)

Figure 1.2:  (a) Sketch of the 2D Hubbard lattice with isotropic nearest-neighbour hopping $t$ and the onsite Coluomb repulsion $U$.  (b) Sketch of the 2-leg Hubbard ladder with onsite Coulomb repulsions $U$, and the intrachain and interchain hopping matrix elements $t$ and $t_\perp$, respectively.

system without first having to construct an approximate theoretical framework for describing its elementary excitations.  The determinantal QMC method was introduced in Ref. [Blankenbecler *et al.* 1981].  The QMC results reviewed here were obtained by using the algorithm described in Ref. [White *et al.* 1989b].  Reviews of this method can be found in Refs. [Scalapino 1993, Muramatsu 1999].  The DMRG method was developed by White [White 1992 and 1993], and since then has been used to calculate the equal-time correlation functions in the ground state of interacting systems. Here, in Sections 3 through 7, numerical results on the 2D and the 2-leg Hubbard models, which were obtained by using these two algorithms, will be presented.  In Appendix, the determinantal QMC and the DMRG techniques will be described briefly.

In Section 2, an introduction to the spin-fluctuation mediated $d_{x^2-y^2}$-wave superconductivity will be given.  In addition, here, the experimental evidence for $d_{x^2-y^2}$-wave superconductivity in the cuprates and the theoretical studies of $d_{x^2-y^2}$-wave pairing in the cuprates will be reviewed briefly.

In order to understand the microscopic many-body processes causing $d_{x^2-y^2}$-wave pairing correlations in the 2D Hubbard model, it is useful to first discuss the magnetic, density and the single-particle excitations.  The review of the numerical studies on the 2D Hubbard model will begin in Section 3 by presenting QMC data on the magnetic properties.  Here, QMC results on the magnetic susceptibility will be shown at and near half-filling.  In addition, an RPA-like model for the magnetic susceptibility will be introduced, and the effective particle-hole vertex will be discussed. The NMR experiments which support the existence of short-range AF fluctuations in the high-$T_c$ cuprates will also be reviewed briefly.

In Section 4, the QMC results on the charge susceptibility will be shown and its dependence on the strength of the Coulomb repulsion will be discussed.  Here, the possibility of any "$4\mathbf{k}_F$" charge-density-wave (CDW) fluctuations in the 2D Hubbard model will be investigated.  In this section, numerical results on the optical conductivity will also be discussed.

The nature of the single-particle excitations in the 2D Hubbard model has received much atten-

tion within the context of the cuprates. In Section 5, the single-particle density of states $N(\omega)$ and spectral weight $A(\mathbf{p}, \omega)$ obtained from the maximum-entropy analytic continuation of the QMC data on the single-particle Green's function will be reviewed. At half-filling, these calculations find a Mott-Hubbard gap, lower and upper Hubbard bands and quasiparticle bands. These quasiparticle bands are similar to those found in a spin-density-wave (SDW) insulator. It will be seen that, upon doping, a redistribution of the spectral weight takes place forming a narrow metallic band at the Fermi level. This band has unusually flat dispersion near the $(\pi, 0)$ and $(0, \pi)$ points of the Brillouin zone leading to large amount of single-particle spectral weight available for scatterings in the particle-particle channel. These results on $A(\mathbf{p}, \omega)$ will also be compared with the results of the angular-resolved photoemission spectroscopy (ARPES) measurements on the cuprates.

After reviewing the numerical results on the magnetic, density and the single-particle properties, in Section 6 the $d_{x^2-y^2}$-wave pairing correlations in the 2D Hubbard model will be discussed. The QMC simulations have found that when doped away from half-filling there are short-range $d_{x^2-y^2}$-wave pairing correlations in the 2D Hubbard model, but no long-range superconducting order has been observed in the parameter regime where the simulations are carried out. The irreducible particle-particle interaction $\Gamma_I$ has been also calculated with the QMC simulations and it gives information on the microscopic many-body processes causing the attraction in the $d_{x^2-y^2}$-wave pairing channel. In Section 6, these QMC results will be reviewed. It will be seen that $\Gamma_I$ is repulsive at $\mathbf{q} = (\pi, \pi)$ momentum transfers and that it is the short-range AF correlations which are responsible for this behavior. Comparisons with the various diagrammatic approaches will also be carried out, which indicate that in the intermediate-coupling regime the momentum and the Matsubara-frequency structure in $\Gamma_I$ can be described by a properly-renormalized single spin-fluctuation exchange interaction. Using the QMC data on $\Gamma_I$ and the single-particle Green's functions, the Bethe-Salpeter equation in the particle-particle channel has been solved. These calculations allow for a comparison of the strength of the pairing correlations in the various channels. Here, it will be seen that as the temperature is lowered, the fastest growing pairing correlations occur in the singlet $d_{x^2-y^2}$-wave channel.

While these calculations are not carried out at sufficiently low temperatures to determine whether the $d_{x^2-y^2}$-wave long-range superconducting order exists in the ground state of the doped 2D Hubbard model, the results on $\Gamma_I$ are useful in the following sense. Consider a phonon-mediated superconductor such as Pb, where the effective interaction mediating the pairing forms already at temperatures of order the characteristic phonon frequency $\omega_D$. Hence, in this case, at $T \sim \omega_D$ it would be possible to study the effective particle-particle interaction responsible for superconductivity, even though the superconducting long-range order takes place at much lower temperatures. Similarly, the QMC simulations are carried out at temperatures of order or less than the characteristic energy scale $J \sim 4t^2/U$ of the AF correlations. Hence, it is possible to probe $\Gamma_I$ in the temperature regime where short-range AF correlations have formed, and see what type of many-body processes are important in mediating the pairing and which pairing channels are favored.

The 2-leg Hubbard ladder is a model where the $d_{x^2-y^2}$-wave superconducting correlations can be studied in detail. In Section 7, the DMRG and the QMC results on the 2-leg Hubbard ladder will be reviewed. The DMRG calculations have found enhanced power-law decaying $d_{x^2-y^2}$-wave superconducting correlations in the ground state of the 2-leg Hubbard ladder. At the same time, with the QMC simulations, it is possible to calculate the magnetic susceptibility, the single-particle spectral weight and the particle-particle vertex $\Gamma_I$ at sufficiently low temperatures. The comparisons of the DMRG and the QMC results show that it is the strong short-range AF fluctuations which mediate the $d_{x^2-y^2}$-wave pairing correlations in this system. Furthermore, in this case, it is possible to study the dependence of the strength of the superconducting correlations on the

model parameters such as $t_\perp/t$ and $U/t$. It will be seen that the superconducting correlations are strongest in the intermediate-coupling regime and when $t_\perp/t$ is such that there is large amount of single-particle spectral weight pinned near the $(\pi, 0)$ and $(0, \pi)$ points of the Brillouin zone. In addition, the QMC calculations find that $\Gamma_I$ peaks at $(\pi, \pi)$ momentum transfer. These features of $A(\mathbf{p}, \omega)$ and $\Gamma_I$ create optimum conditions for $d_{x^2-y^2}$-wave superconducting correlations. In Section 7.3, these numerical results on the 2D and the 2-leg Hubbard models will be compared with each other. This comparison suggests that the $d_{x^2-y^2}$-wave pairing correlations seen in these models do not require a particularly sharp peak in $\Gamma_I$ but rather simply weight at momentum transfers near $(\pi, \pi)$.

In Section 8, the QMC and the DMRG results reviewed above will be compared with the diagrammatic and the other numerical approaches to the Hubbard model as well as with the numerical results on the $t$-$J$ model. First, in Section 8.1, the QMC results on the 2D Hubbard model will be compared with the results of the fluctuation exchange (FLEX) approach. Here, the purpose will be to make simple estimates for the maximum $T_c$ possible in the 2D Hubbard model, if a superconducting phase were to occur. In particular, the effects of the system being near an AF Mott-Hubbard insulator on the strength of the $d_{x^2-y^2}$-wave pairing will be explored. In Section 8.2, the results from the variational and the projector Monte Carlo studies of the Hubbard model will be reviewed briefly. Recently, the dynamical cluster approximation (DCA) and the one-loop renormalization-group (RG) technique employing a 2D Fermi surface were applied to study $d_{x^2-y^2}$ pairing in the 2D Hubbard model. The results of these calculations will be discussed in Section 8.3. The origin of the normal state properties of the cuprates in the pseudogap regime remains an important problem in this field. In Section 8.4, the findings of various calculations in the low-doping regime of the Hubbard model will be compared with the pseudogap regime of the cuprates.

The Hubbard model is closely related to the $t$-$J$ model, for which various Monte Carlo, exact diagonalization and DMRG calculations have been carried out. There is much interest in the ground-state phase diagram and the nature of the density and the pairing correlations in this model. In Section 8.5, the numerical studies on phase separation, stripe correlations and the $d_{x^2-y^2}$-wave pairing correlations in the $t$-$J$ model will be briefly reviewed and compared with the results on the Hubbard model. Comparisons will also be made with the 2-leg $t$-$J$ model.

In Section 8.6, the implications of the numerical results on the Hubbard model for the nature of the $d_{x^2-y^2}$-wave pairing in the high-$T_c$ cuprates will be discussed. In Section 9, the summary and the conclusions will be given.

# 2 $d_{x^2-y^2}$-wave superconductivity in the cuprates

## 2.1 Spin-fluctuation mediated $d_{x^2-y^2}$-wave superconductivity

Since the development of the BCS theory, it has been of interest to see whether the effective interaction which is responsible for pairing could be mediated by excitations other than phonons. The superfluidity of $^3$He is an example where it is believed that the pairing is due to the exchange of ferromagnetic spin fluctuations resulting in triplet $p$-wave superconductivity [Leggett 1975]. Within the context of organic superconductors, the possibility of the pairing being mediated by spin fluctuations had been noted in Ref. [Emery 1986]. For the heavy fermion materials, the possibility of $d$-wave superconductivity due to the exchange of AF spin fluctuations was proposed in Refs. [Scalapino *et al.* 1986, Miyake *et al.* 1986, Cyrot 1986]. For the high-$T_c$ superconductors, the possibility of $d_{x^2-y^2}$-wave superconductivity was first studied in Ref. [Bickers *et al.* 1987], where

the framework of the two-dimensional Hubbard model was used near an SDW phase.

Here, a discussion of these ideas on how the exchange of the AF spin-fluctuations leads to a $d_{x^2-y^2}$-wave gap function will be given, since this picture will be useful for the remainder of the article. In the paramagnetic phase of the 2D Hubbard model and within RPA, the single spin-fluctuation exchange interaction between opposite-spin particles at zero frequency transfer is given by [Berk and Schrieffer 1966, Doniach and Engelsberg 1966]

$$V(\mathbf{p}'|\mathbf{p}) = U + \frac{U^3\chi_0^2(\mathbf{p}'-\mathbf{p})}{1-U^2\chi_0^2(\mathbf{p}'-\mathbf{p})} + \frac{U^2\chi_0(\mathbf{p}'+\mathbf{p})}{1-U\chi_0(\mathbf{p}'+\mathbf{p})}, \tag{2.1}$$

where $\chi_0(\mathbf{q})$ is the usual Lindhard function. The longitudinal and the transverse spin fluctuations contributing to $V$ are illustrated in Fig. 2.1. Here, $V(\mathbf{p}'|\mathbf{p})$ is the interaction for the scattering of a pair of opposite-spin electrons at states $(\mathbf{p}, -\mathbf{p})$ to $(\mathbf{p}', -\mathbf{p}')$. Near half-filling and for a tight-binding band structure $\varepsilon_{\mathbf{p}} = -2t(\cos p_x + \cos p_y) - \mu$, where $\mu$ is the chemical potential, the Lindhard function peaks at $\mathbf{q} \sim (\pi, \pi)$. Consequently, for a system with Stoner-enhanced AF correlations, the spin-fluctuation exchange interaction $V(\mathbf{p}'|\mathbf{p})$ is large and repulsive at $\mathbf{p}' - \mathbf{p} \sim (\pi, \pi)$ momentum transfers. Now, consider the BCS gap equation

$$\Delta_{\mathbf{p}} = -\sum_{\mathbf{p}'} \frac{V(\mathbf{p}|\mathbf{p}')\Delta_{\mathbf{p}'}}{2E_{\mathbf{p}'}}, \tag{2.2}$$

where $\mathbf{p}$ and $\mathbf{p}'$ are restricted to being on the Fermi surface of the doped system as illustrated in Fig. 2.2. When this equation is solved, it is found that the leading superconducting instability occurs for a gap function with the $d_{x^2-y^2}$-wave symmetry,

$$\Delta_{\mathbf{p}} = \frac{\Delta_0}{2}(\cos p_x - \cos p_y). \tag{2.3}$$

In order to see why the $d_{x^2-y^2}$-wave form is a solution, consider a quasiparticle pair occupying $(\mathbf{p}, -\mathbf{p})$ with $\mathbf{p}$ near $(\pi, 0)$, as shown in Fig. 2.2. This pair can scatter to $(\mathbf{p}', -\mathbf{p}')$ where $\mathbf{p}' \sim (0, \pi)$ through the interaction $V(\mathbf{p}'|\mathbf{p})$, which is enhanced and positive for momentum transfers near $(\pi, \pi)$, because $\Delta_{\mathbf{p}}$ changes sign between $\mathbf{p}$ and $\mathbf{p}'$. This is basically the reason for why the $d_{x^2-y^2}$-wave gap symmetry is favored by the AF spin fluctuations. Since $V(\mathbf{p}'|\mathbf{p})$ is always positive, there is no singlet solution with the usual $s$-wave symmetry. For simplicity, these arguments were given at zero frequency, where $\mathbf{p}$ and $\mathbf{p}'$ are restricted to being on the Fermi surface, but the same arguments hold when the frequency dependencies of the gap equation and of the effective interaction are taken into account. In Section 6, the QMC data on the irreducible particle-particle interaction $\Gamma_I$ and the solutions of the Bethe-Salpeter equation will be reviewed for the 2D Hubbard model. There, it will be seen that $\Gamma_I$ is similar to the single spin-fluctuation exchange interaction and the leading singlet pairing instability occurs in the $d_{x^2-y^2}$-wave channel in the parameter regime where the QMC simulations are carried out.

## 2.2   Experimental evidence for $d_{x^2-y^2}$-wave superconductivity in the cuprates

Early experimental evidence for $d_{x^2-y^2}$-wave pairing in the cuprates arose from the measurement of the NMR longitudinal nuclear relaxation rate $T_1^{-1}$ for Cu(2) and O(2,3) nuclei in YBa$_2$Cu$_3$O$_7$. In particular, the anisotropy of $T_1^{-1}$ for Cu(2) below $T_c$ provided a signature for $d_{x^2-y^2}$-wave pairing in this compound [Takigawa *et al.* 1991, Martindale *et al.* 1992, Bulut and Scalapino 1992]. These NMR measurements provided evidence for both the phase and the nodes of the $d_{x^2-y^2}$-wave gap
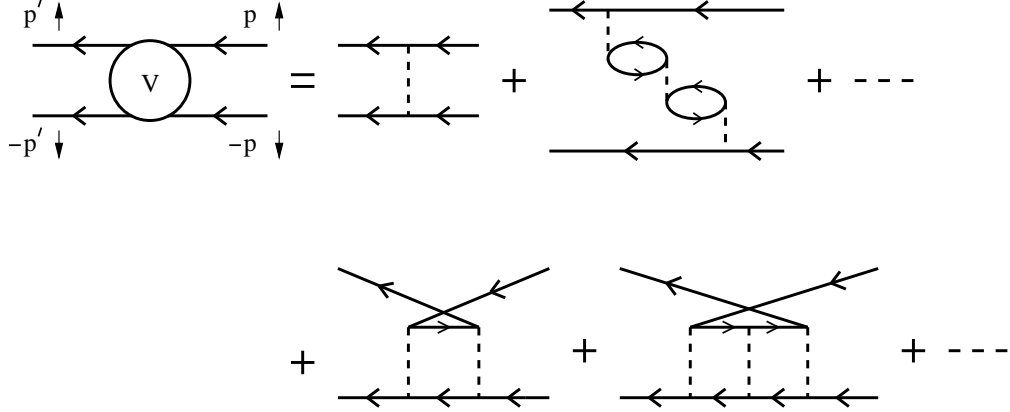
Figure 2.1: Feynman diagrams illustrating the effective particle-particle interaction $V(\mathbf{p}'|\mathbf{p})$ within the single spin-fluctuation exchange approximation.
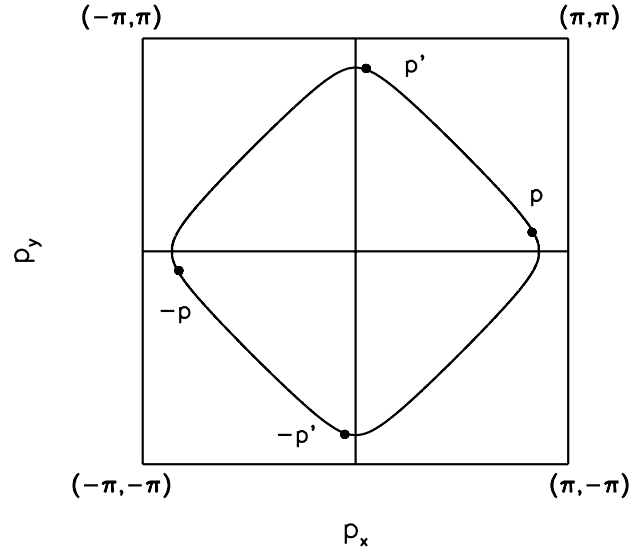


Figure 2.2: Sketch of the Fermi surface of the 2D tight-binding model doped near half-filling. The two-particle momentum states $(\mathbf{p}, -\mathbf{p})$ and $(\mathbf{p}', -\mathbf{p}')$ are indicated by the filled circles.

function. The temperature dependence of the Cu(2) transverse nuclear relaxation rate $T_2^{-1}$ was also used for the identification of the gap symmetry [Bulut and Scalapino 1991, Itoh *et al.* 1992]. These NMR measurements were also supported by the ARPES experiments which extracted the magnitude of the gap function $|\Delta_{\mathbf{p}}|$ on the Fermi surface [Shen *et al.* 1993]. The microwave cavity measurements of the superconducting penetration depth $\lambda(T)$ in single crystals of $YBa_2Cu_3O_7$ found a linear temperature variation which also gave support to a $d_{x^2-y^2}$-wave gap [Hardy *et al.* 1993]. The phase-coherence measurements on YBCO-Pb dc SQUIDS [Wollman *et al.* 1993] and the tricrystal experiments of Tsuei *et al.* [Tsuei *et al.* 1994] established that in $YBa_2Cu_3O_7$ the order parameter has the $d_{x^2-y^2}$-wave symmetry. Reviews of these results on the symmetry of the gap function are given in Refs. [Schrieffer 1994, Scalapino 1995, van Harlingen 1995, Tsuei and Kirtley 2000]. Today, it is established that in a number of the hole and the electron doped cuprates

the gap function has the $d_{x^2-y^2}$-wave symmetry [Tsuei and Kirtley 2000].

## 2.3   Theoretical studies of $d_{x^2-y^2}$-wave pairing in the cuprates

For the high-$T_c$ cuprates, the possibility of $d_{x^2-y^2}$-wave superconductivity was first studied by Bickers $et\ al.$ [Bickers $et\ al.$ 1987] using the framework of the 2D Hubbard model. In particular, the single spin-fluctuation exchange interaction was used for studying the $d_{x^2-y^2}$-wave pairing near an SDW instability within the random-phase approximation. In these calculations, the effect of the single-particle self-energy corrections due to the spin fluctuations was taken into account.

The next level of calculations for the $d_{x^2-y^2}$-wave superconductivity were carried out using the fluctuation-exchange approximation (FLEX) within the 2D Hubbard model [Bickers $et\ al.$ 1989]. This method self-consistently treats the fluctuations in the magnetic, density and the pairing channels. Within this approach it was found that the AF spin fluctuations lead to a $d_{x^2-y^2}$-wave superconducting phase which neighbors the SDW phase. In these calculations, superconducting transition temperatures as high as $0.025t$ were found [Bickers $et\ al.$ 1989, Bickers and White 1991]. Since the hopping matrix element within a one-band description of the cuprates is estimated to be about 0.45 eV [Hybertson $et\ al.$ 1990], this value of $T_c$ corresponds to about 130 K. However, the need to carry out exact calculations was also noted.

Another approach to $d_{x^2-y^2}$-wave pairing in the cuprates was from a phenomenological point of view [Moriya $et\ al.$ 1990]. In this approach, a spin-fluctuation exchange interaction was used to calculate the superconducting transition temperatures. The spin susceptibility and the parameters used in the model were obtained from fitting the NMR and the electrical resistivity data on the normal state of the cuprates within the self-consistent renormalization theory. In these calculations, the single-particle self-energy corrections due to the spin fluctuations were also included, and $T_c$'s as high as those in the cuprates were obtained. A review of these calculations can be found in Ref. [Moriya and Ueda 2000].

A similar phenomenological approach was taken in Ref. [Monthoux $et\ al.$ 1991]. In this approach, the spin susceptibility used in the effective interaction was also taken from fitting the NMR data, and $T_c$'s comparable to those in the cuprates were obtained. In these calculations, the $T_c$ was initially calculated without including the self-energy effects. Later, the self-energy corrections were included self-consistently [Monthoux and Pines 1992].

These spin-fluctuation theories for superconductivity differ from phonon-mediated superconductivity in a fundamental way. Here, the effective attractive interaction which is responsible for pairing the electrons is generated by the electronic correlations rather than by an external system such as the lattice vibrations. Hence, it is an important question whether in a microscopic model the electronic correlations can indeed produce an effective attractive interaction which leads to superconductivity, and, if so, what would be the nature and the strength of such pairing correlations. The QMC and the DMRG methods were developed to address these types of questions. The numerical studies of the Hubbard model carried out with this purpose are the subject of this review article.

## 3   Magnetic correlations in the 2D Hubbard model

The parent compounds of the cuprates are AF insulators, and the AF phase extends up to ~5% doping. For dopings beyond this, there is clear evidence from the NMR and the inelastic neutron scattering experiments that the system exhibits short-range AF spin fluctuations [Pennington and

Slichter 1990, Birgeneau 1990]. These are properties which support using the Hubbard framework for studying the electronic correlations of the cuprates.

The QMC calculations have found that the ground state of the Hubbard model at half-filling has AF long-range order [Hirsch and Tang 1989, White *et al.* 1989b]. Away from half-filling, the QMC calculations find short range AF correlations [Hirsch 1985]. In this section, the QMC results on the magnetic susceptibility $\chi$ of the 2D Hubbard model will be reviewed, and compared with an RPA-like approach for modelling it. In addition, the QMC results on the irreducible particle-hole vertex will be discussed. These will be useful for gaining a microscopic understanding of the magnetic correlations in the Hubbard model.



Figure 3.1: (a) Static magnetic susceptibility $\chi(\mathbf{q}, 0)$ versus $\mathbf{q}$. (b) Equal-time correlation function $|\langle m^z(\mathbf{r})m^z(0)\rangle|$ versus $\mathbf{r}$ along $(1,0)$. These results are for $U = 8t$ and $\langle n \rangle = 1.0$ on an $8 \times 8$ lattice.

## 3.1 Antiferromagnetic long-range order at half-filling

The transverse magnetic susceptibility is defined by

$$\chi(\mathbf{q}, \omega) = \frac{1}{N} \sum_{\ell} \int_0^{\beta} d\tau \, e^{i\omega_m \tau} e^{-i\mathbf{q}\cdot\ell} \langle m^-(i+\ell, 0)m^+(i, 0)\rangle. \tag{3.1}$$

Here, $m^+(i, 0) = c_{i\uparrow}^{\dagger}c_{i\downarrow}$, and $m^-(i, \tau) = e^{H\tau}m^-(i, 0)e^{-H\tau}$, where $m^-(i, 0)$ is the hermitian conjugate of $m^+(i, 0)$. Ref. [Mahan 1981] can be consulted for the finite-temperature Green's function formalism. In the following, $\chi$ will be plotted in units of $t^{-1}$. Figure 3.1(a) shows $\chi(\mathbf{q}, i\omega_m = 0)$ versus $\mathbf{q}$ along various cuts in the Brillouin zone as the temperature is lowered. Here, it is seen that as $T$ is lowered, $\chi(\mathbf{q}, 0)$ develops a sharp peak at the antiferromagnetic wave vector $\mathbf{q} = (\pi, \pi)$.

Figure 3.1(b) shows the equal-time correlation function

$$|\langle m^z(\mathbf{r})m^z(0)\rangle|, \tag{3.2}$$

11

where $m^z(\mathbf{r}) = c^\dagger_{\mathbf{r}\uparrow}c_{\mathbf{r}\uparrow} - c^\dagger_{\mathbf{r}\downarrow}c_{\mathbf{r}\downarrow}$, versus $\mathbf{r}$ as the temperature is lowered on an $8 \times 8$ lattice at half-filling. In this figure, it is seen that as $T$ is lowered below $0.5t$, the AF correlation length $\xi_{AF}$ reaches the size of the system and long-range AF order is established on the $8 \times 8$ lattice. For an infinite lattice, the long-range AF order would take place at $T = 0$.
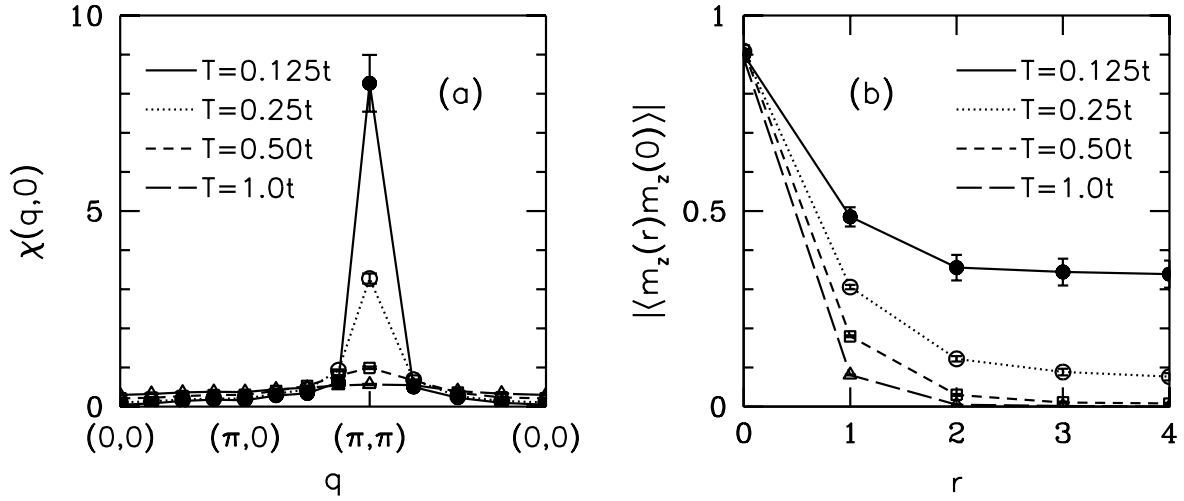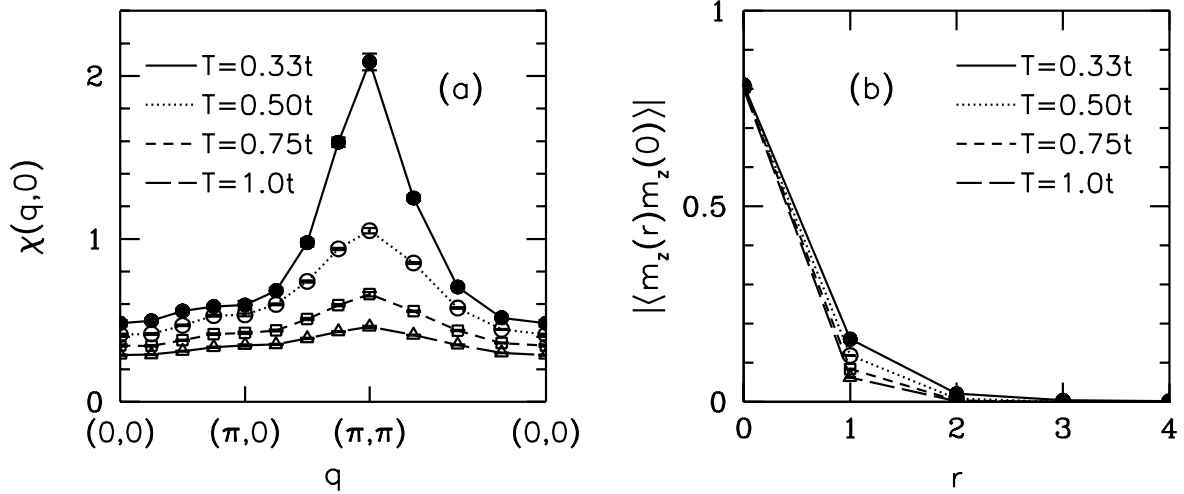


Figure 3.2: (a) Static magnetic susceptibility $\chi(\mathbf{q}, 0)$ versus $\mathbf{q}$. (b) Equal-time correlation function $|\langle m^z(\mathbf{r})m^z(0)\rangle|$ versus $\mathbf{r}$ along $(1, 0)$. These results are for $U = 8t$ and $\langle n \rangle = 0.87$ on an $8 \times 8$ lattice.

## 3.2 Short-range antiferromagnetic fluctuations away from half-filling

Figure 3.2(a) shows $\chi(\mathbf{q}, 0)$ versus $\mathbf{q}$ for $\langle n \rangle = 0.87$ and $U = 8t$ on the $8 \times 8$ lattice. Here, as $T$ decreases, the development of a broad peak centred at $\mathbf{q} = (\pi, \pi)$ is seen. Figure 3.2(b) shows the corresponding $|\langle m^z(\mathbf{r})m^z(0)\rangle|$ versus $\mathbf{r}$. At the lowest temperature of $0.33t$, the AF correlation length $\xi$ is about $0.6$ lattice spacing for this filling. Here, $\xi$ was obtained by fitting the decay of $|\langle m^z(\mathbf{r})m^z(0)\rangle|$ to $e^{-|\mathbf{r}|/\xi}$.

The Monte Carlo results on $\chi(\mathbf{q}, i\omega_m)$ have been analytically continued to the real frequency axis using the Pade approximation. The results on the spin-fluctuation spectral weight $\mathrm{Im}\,\chi(\mathbf{q}, \omega)$ versus $\omega$ at $\mathbf{q} = (\pi, \pi)$ obtained in this way are shown in Fig. 3.3(a). While the Pade approximation can only resolve the crude features of the spectrum, the softening of the AF spin fluctuations at low temperatures is clearly seen.

Another quantity which can be used for characterising the low-frequency magnetic correlations is

$$F(\mathbf{q}) = \left.\frac{\mathrm{Im}\,\chi(\mathbf{q}, \omega)}{\omega}\right|_{\omega \to 0}. \tag{3.3}$$

This quantity is of interest because it is used to calculate the longitudinal nuclear relaxation rates of the planar Cu and O nuclear spins in the layered cuprates. Figure 3.3(b) shows $F(\mathbf{q})$ versus $\mathbf{q}$ for $\langle n \rangle = 0.87$ and $U = 8t$. As $T$ is lowered, $F(\mathbf{q})$ gets enhanced at $(\pi, \pi)$, and more weakly at $\mathbf{q} \sim 0$.
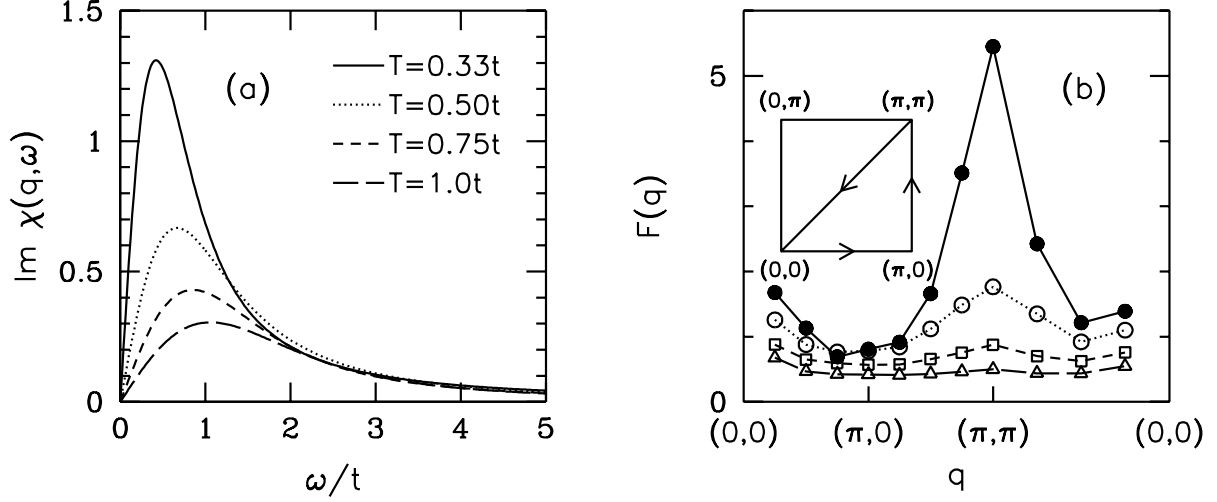
12

Figure 3.3: (a) Spin-fluctuation spectral weight $\mathrm{Im}\,\chi(\mathbf{q},\omega)$ versus $\omega$ at $\mathbf{q} = (\pi,\pi)$. (b) $F(\mathbf{q})$ versus $\mathbf{q}$ for the same temperatures as in (a). These results are for $U = 8t$ and $\langle n \rangle = 0.87$ on an $8 \times 8$ lattice.

## 3.3  RPA-like model for the magnetic susceptibility

An RPA-like approach has been used for modelling $\chi(\mathbf{q},\omega)$ in the intermediate coupling regime with the form [Bulut *et al.* 1990, Bulut 1990, Chen *et al.* 1991, Bulut *et al.* 1993]

$$\chi(\mathbf{q},\omega) = \frac{\chi_0(\mathbf{q},\omega)}{1 - \overline{U}\chi_0(\mathbf{q},\omega)} \tag{3.4}$$

where $\chi_0(\mathbf{q},\omega)$ is the Lindhard function for the band electrons

$$\chi_0(\mathbf{q},\omega) = \frac{1}{N}\sum_{\mathbf{p}} \frac{f(\varepsilon_{\mathbf{p+q}}) - f(\varepsilon_{\mathbf{p}})}{\omega - (\varepsilon_{\mathbf{p+q}} - \varepsilon_{\mathbf{p}}) + i\delta}, \tag{3.5}$$

$\varepsilon_{\mathbf{p}} = -2t(\cos p_x + \cos p_y) - \mu$ and $f(\varepsilon_{\mathbf{p}})$ is the usual Fermi factor. The parameter $\overline{U}$ entering Eq. (3.4) represents the reduced Coulomb repulsion, which is assumed to be renormalized due to the electronic correlations. In this simple approach, $\overline{U}$ is taken to be independent of momentum and temperature. This turns out to be a reasonable approximation in the temperature range where the Monte Carlo simulations have been carried out.

Figure 3.4(a) compares this RPA-like approximation for $\chi(\mathbf{q},0)$ with the Monte Carlo data for $U = 4t$, $T = 0.25t$ and $\langle n \rangle = 0.87$. A similar comparison is given in Fig. 3.4(b) for the $T$ dependence of $\chi(\mathbf{q} = (\pi,\pi),0)$. In these figures $\overline{U} = 2t$ has been used. This choice will be discussed further in the following subsection, where results on the irreducible particle-hole vertex will be reviewed.
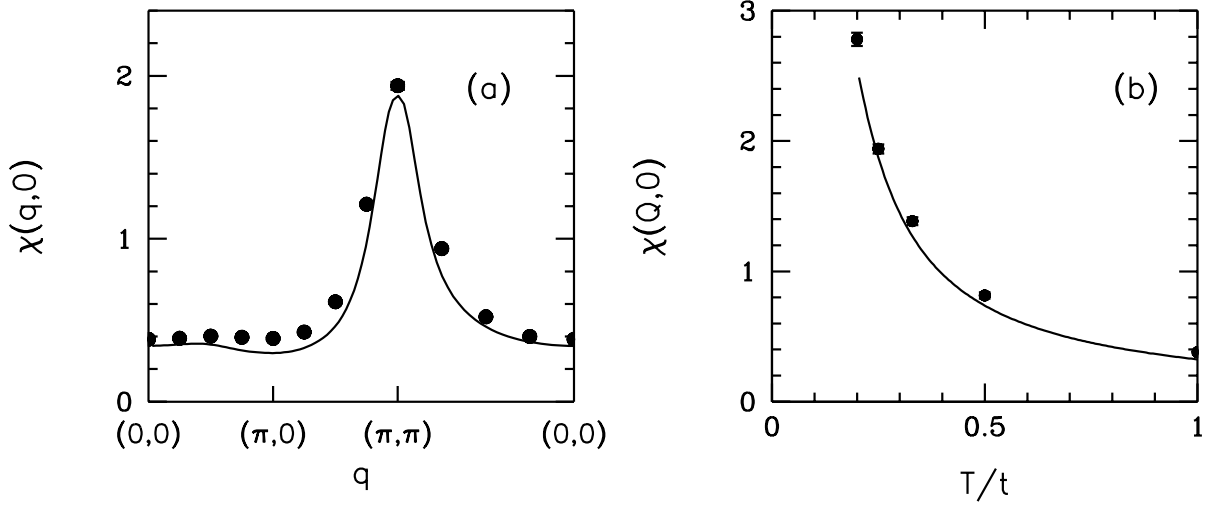
13

Figure 3.4: (a) Comparison of the QMC and the RPA results on $\chi(\mathbf{q}, 0)$ versus $\mathbf{q}$ at $T = 0.25t$. (b) Comparison of the QMC and the RPA results on $\chi(\mathbf{Q} = (\pi, \pi), 0)$ versus $T/t$. Here, the QMC data (filled circles) are for $U = 4t$ and the RPA results (solid curves) were obtained using $\overline{U} = 2t$. In both figures, the results are shown for $\langle n \rangle = 0.87$.

## 3.4 Irreducible particle-hole interaction

In the RPA form discussed above, a reduced Coulomb repulsion $\overline{U}$ which is independent of $\mathbf{q}$ is used. In order to test this approximation, the effective particle-hole vertex defined by

$$\overline{U}(\mathbf{q}, i\omega_m) = \frac{1}{\overline{\chi}(\mathbf{q}, i\omega_m)} - \frac{1}{\chi(\mathbf{q}, i\omega_m)}, \tag{3.6}$$

was calculated in Ref. [Bulut *et al.* 1995]. Here, $\overline{\chi}(\mathbf{q}, i\omega_m)$ is the piece of the magnetic susceptibility which does not include the reducible particle-hole vertex, and it is defined by

$$\overline{\chi}(\mathbf{q}, i\omega_m) = -\frac{T}{N} \sum_{\mathbf{p}, i\omega_m} G(\mathbf{p} + \mathbf{q}, i\omega_n + i\omega_m) G(\mathbf{p}, i\omega_n), \tag{3.7}$$

where $G(\mathbf{p}, i\omega_n)$ is the exact single-particle Green's function calculated with QMC. In Fig. 3.5(a), the QMC data on $\overline{\chi}(\mathbf{q}, 0)$ versus $\mathbf{q}$ is compared with the Lindhard function $\chi_0(\mathbf{q}, 0)$ at $T = 0.25t$. Here, one sees that $\overline{\chi}(\mathbf{q}, 0)$ is suppressed with respect to $\chi_0(\mathbf{q}, 0)$, and this is because of the single-particle self-energy effects. The effective irreducible vertex $\overline{U}(\mathbf{q}, 0)$ obtained from the QMC data on $\chi(\mathbf{q}, 0)$ and $\overline{\chi}(\mathbf{q}, 0)$ is plotted in Fig. 3.5(b) as a function of $\mathbf{q}$ at various temperatures. In this figure it is seen that $\overline{U}(\mathbf{q}, 0)$ shows little dependence on $\mathbf{q}$ and $T$. This is the reason for the good agreement between the QMC data and the RPA results obtained using a reduced $\overline{U}$ in Eq. (3.4). However, the values of $\overline{U}(\mathbf{q}, 0)$ are larger than $\overline{U} = 2t$ used in the RPA. For instance, at $T = 0.25t$ one has $\overline{U}(\mathbf{q} = (\pi, \pi), 0) = 3.2t$. This is because in the RPA form the Lindhard susceptibility $\chi_0$ is used rather than $\overline{\chi}$, which has the effects of the single-particle self-energy corrections. At this point,
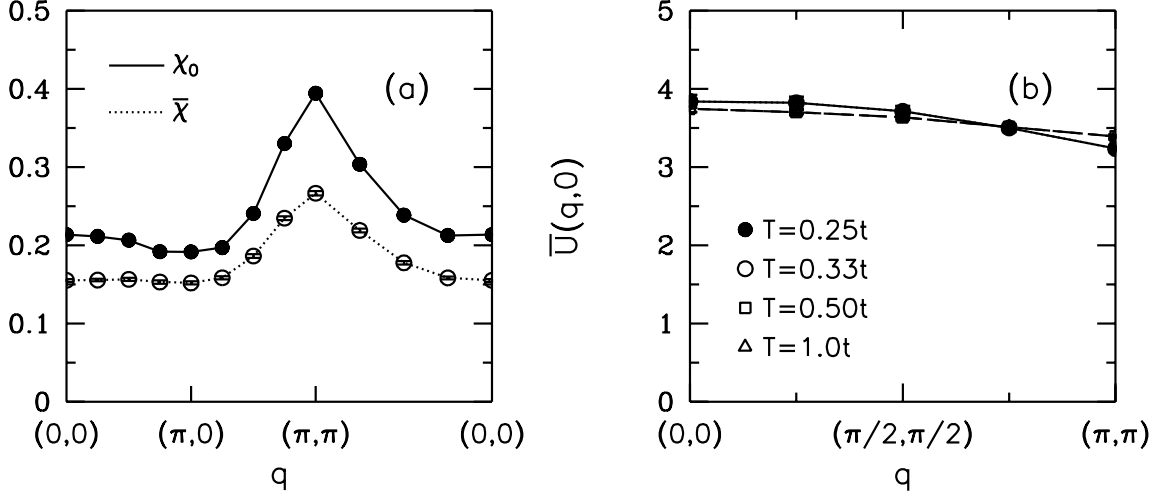
14

Figure 3.5: (a) Comparison of the QMC data on $\overline{\chi}(\mathbf{q}, 0)$ versus $\mathbf{q}$ with the Lindhard function $\chi_0(\mathbf{q}, 0)$ at $T = 0.25t$. (b) Effective particle-hole vertex $\overline{U}(\mathbf{q}, 0)$ versus $\mathbf{q}$ along $(1, 1)$. These results were obtained for $U = 4t$ and $\langle n \rangle = 0.87$ on an $8 \times 8$ lattice.

it should be noted that the momentum dependence of the effective particle-hole vertex within the context of the cuprates was also discussed in Ref. [Anderson 1997].

With the QMC simulations the irreducible particle-hole vertex $\overline{\Gamma}_I$ was also calculated [Bulut *et al.* 1995]. The calculation of $\overline{\Gamma}_I$ is similar to that of the irreducible particle-particle vertex $\Gamma_I$, which will be discussed in Section 6. In this approach, $\overline{\Gamma}_I$ is obtained from the solution of the particle-hole $t$-matrix equation illustrated in Fig. 3.6. These calculations showed that the QMC data on $\overline{\Gamma}_I$ are in agreement with the results on the effective particle-hole vertex $\overline{U}(\mathbf{q}, 0)$ discussed in this section. In particular, $\overline{\Gamma}_I$ with the center-of-mass momentum $\mathbf{q} = (\pi, \pi)$ and frequency $\omega_m = 0$ was averaged over the incoming and outgoing momenta near the Fermi surface, and it was found that this average $\langle \overline{\Gamma}_I \rangle$ is $3.6t \pm 0.7t$ for $U = 4t$, $T = 0.25t$ and $\langle n \rangle = 0.87$. This agrees with $\overline{U}(\mathbf{q} = (\pi, \pi), 0) = 3.2t$ found above. Hence, the effective particle-hole vertex for center-of-mass momentum $\mathbf{q} = (\pi, \pi)$ and frequency $\omega_m = 0$ is about $3.2t$ for a bare Coulomb repulsion of $U = 4t$. The difference reflects the renormalization of the bare Coulomb repulsion in the particle-hole channel due to the higher-order many-body processes such as the Kanamori type of particle-particle scatterings [Kanamori 1963]. However, in the RPA form of Eq. (3.4), $\overline{U} = 2t$ needs to be used in order to take into account the single-particle self-energy corrections which are neglected within RPA.

These results on the effective particle-hole vertex will also be useful when the irreducible particle-particle interaction $\Gamma_I$ is compared with the single spin-fluctuation exchange interaction $\Gamma_{Is}^{SF}$ in Section 6.4. There, it will be seen that when the effective coupling $gU$ between the electrons and the spin fluctuations is taken to be about $3.2t$, the resulting $\Gamma_{Is}^{SF}$ agrees with the QMC data on $\Gamma_I$. One expects $gU$ to be closely related to $\overline{\Gamma}_I$ and, hence, the QMC data on the effective particle-particle and particle-hole vertices are consistent.
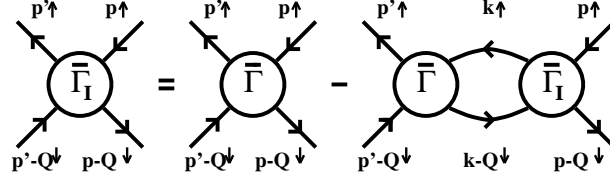
Figure 3.6: Feynman diagrams for the particle-hole $t$-matrix equation.

## 3.5 Comparison with the NMR experiments on the cuprates

The measurements of the longitudinal NMR rate $T_1^{-1}$ have provided evidence for the existence of short-range AF fluctuations in the normal state of the high-$T_c$ cuprates. These experiments are reviewed in Refs. [Pennington and Slichter 1990, Takigawa 1990]. The relaxation rate $T_1^{-1}$ is given by

$$T_1^{-1} = \frac{T}{N} \sum_{\mathbf{q}} |A(\mathbf{q})|^2 F(\mathbf{q}), \tag{3.8}$$

where $|A(\mathbf{q})|^2$ is the hyperfine form factor of the particular nuclear spin, and $F(\mathbf{q})$ has been defined in Section 3.2. The hyperfine form factors used in calculating the various NMR rates for the cuprates were derived in Ref. [Mila and Rice 1989].

An additional experimental quantity which supports the existence of the short-range AF correlations in the cuprates is the transverse relaxation rate $T_2^{-1}$, which is given by [Pennington and Slichter 1991]

$$\left( \frac{1}{T_2} \right)^2 = \frac{1}{N} \sum_{\mathbf{q}} |A(\mathbf{q})|^4 \chi^2(\mathbf{q}, 0) - \left( \frac{1}{N} \sum_{\mathbf{q}} |A(\mathbf{q})|^2 \chi(\mathbf{q}, 0) \right)^2. \tag{3.9}$$

The measurements of $T_2^{-1}$ for $^{63}$Cu(2) in the normal state of the YBa$_2$Cu$_3$O$_7$, YBa$_2$Cu$_4$O$_8$ and the La$_{2-x}$Sr$_x$CuO$_4$ systems have provided evidence for the presence of the short-range AF correlations in these compounds. [Pennington and Slichter 1991, Itoh *et al.* 1992, Imai *et al.* 1993].

Since the Monte Carlo calculations cannot be carried out at low temperatures, it is difficult to make direct comparisons with the $T_1^{-1}$ and the $T_2^{-1}$ measurements on the cuprates using the Monte Carlo data. However, the RPA-like model described above in Section 3.3 has been used to calculate the NMR rates in the normal state. Even though it is a simple approximation, this approach has been useful for analysing the $T_1^{-1}$ and the $T_2^{-1}$ data on YBa$_2$Cu$_3$O$_7$ [Bulut *et al.* 1990, Bulut and Scalapino 1991]. These calculations imply that the low-energy AF spin fluctuations estimated for the 2D Hubbard model have the right order of magnitude for describing the general features of the AF correlations in optimally doped YBa$_2$Cu$_3$O$_7$. The NMR data on YBa$_2$Cu$_3$O$_7$ were also fit phenomenologically [Millis *et al.* 1990] and by using self-consistent renormalization theory [Moriya *et al.* 1990].

## 4 Charge fluctuations in the 2D Hubbard model

In this section, the QMC data on the charge susceptibility and the optical conductivity of the 2D Hubbard model will be reviewed.

## 4.1 Charge susceptibility

The momentum and frequency dependent charge susceptibility is defined by

$$\Pi(\mathbf{q}, i\omega_m) = \int_0^\beta d\tau \, e^{i\omega_m \tau} \, S(\mathbf{q}, \tau) \qquad (4.1)$$

where

$$S(\mathbf{q}, \tau) = -\langle T\rho(\mathbf{q}, \tau)\rho^\dagger(\mathbf{q}, 0)\rangle, \qquad (4.2)$$

with $\rho^\dagger(\mathbf{q}) = \frac{1}{\sqrt{N}}\sum_{\mathbf{p}\sigma} c^\dagger_{\mathbf{p}+\mathbf{q}\sigma} c_{\mathbf{p}\sigma}$ and $\rho(\mathbf{q}, \tau) = e^{H\tau}\rho(\mathbf{q})e^{-H\tau}$. The equal-time density-density correlation function $S(\mathbf{q}) \equiv S(\mathbf{q}, \tau = 0)$ and the charge compressibility $\kappa = \partial\langle n\rangle/\partial\mu$ given by $\Pi(\mathbf{q} \to 0, 0)$ are also of interest. In the following $\Pi$ and $S$ will be plotted in units of $t^{-1}$. The nature of the density correlations in the 2D Hubbard model was studied with various numerical techniques. The QMC [Moreo and Scalapino 1991, Moreo $et\ al.$ 1991] and the exact diagonaliza-tion [Dagotto $et\ al.$ 1992b] calculations did not find any indication of phase separation in the 2D Hubbard model. The charge compressibility of the Hubbard model near half-filling was calculated by zero-temperature QMC simulations [Furukawa and Imada 1991 and 1992]. At fillings $\langle n\rangle = 0.5$ and 0.2, $S(\mathbf{q})$ was calculated with the determinantal QMC for $U = 4t$ and $8t$ on up to $16 \times 16$ lattices [Chen $et\ al.$ 1994]. The Green's function Monte Carlo (GFMC) method was also used for calculating $S(\mathbf{q})$ for the 2D Hubbard model on lattices with up to 162 sites in the ground state [Becca $et\ al.$ 2000]. These calculations were carried out for $U = 4t$ and $10t$ at and near half-filling. In this section, the QMC results on $\Pi(\mathbf{q}, \omega)$ and $S(\mathbf{q})$ from Ref. [Bulut 1996] will be shown for various values of $U/t$ near half-filling.

Extensive numerical calculations have been also carried out for studying the density correlations in the ground state of the $t$-$J$ model. These calculations have found phase-separated, striped, and uniform phases, and they will be briefly described in Section 8. The results on $\Pi(\mathbf{q}, \omega)$ and $S(\mathbf{q})$ presented here were obtained at relatively high temperatures and it is difficult to reach conclusions about the ground state of the Hubbard model using them. Nevertheless, here, the QMC data on the density correlations will be compared with the results on the $t$-$J$ model obtained with the high-temperature series expansions [Putikka $et\ al.$ 1994]. This gives valuable information on the dynamics of the density fluctuations in the 2D Hubbard model

The high-temperature series expansions have found that the structure in $S(\mathbf{q})$ can be described by the noninteracting spinless-fermion model. This is due to the fact that the double-occupancy of the sites is not allowed in the $t$-$J$ model, and once this constraint is taken into account, the density correlations are similar to those of the noninteracting particles. Consequently, for a filling $\langle n\rangle$, $S(\mathbf{q})$ has structure at wave vectors which are associated with the Fermi surface corresponding to a filling of $2\langle n\rangle$. In other words, the structure in $S(\mathbf{q})$ follows the "$4\mathbf{k}_F$" wave vectors rather than the "$2\mathbf{k}_F$" wave vectors of the system.

First, results at half-filling will be presented. Figure 4.1 shows QMC results on $\Pi(\mathbf{q}, 0)$ versus $\mathbf{q}$ at various temperatures for $U = 8t$. Here, $\Pi(\mathbf{q}, 0)$ is rather featureless in $\mathbf{q}$, and it gets further suppressed as $T$ is lowered. This is due to the Mott-Hubbard gap which exists at half-filling. Next, results for $\langle n\rangle = 0.87$ are shown. Figure 4.2(a) shows the temperature evolution of $\Pi(\mathbf{q}, 0)$ versus $\mathbf{q}$ for $U = 8t$. In this case, the $\mathbf{q} \sim 0$ component of $\Pi(\mathbf{q}, 0)$ gets enhanced as $T$ decreases. The $T$ dependence of $\Pi(\mathbf{q} \to 0, 0)$ seen in Fig. 4.2(a) is consistent with the results of the zero-temperature QMC calculations of the charge compressibility [Furukawa and Imada 1991 and 1992]. Figure 4.2(b) shows $\text{Im}\,\Pi(\mathbf{q}, \omega)$ versus $\omega$ for $\mathbf{q} = (\pi/4, 0)$, where it is seen that the density fluctuations soften as $T$ is lowered. The spectral weight $\text{Im}\,\Pi$ was obtained by the Pade analytic continuation of the QMC data.
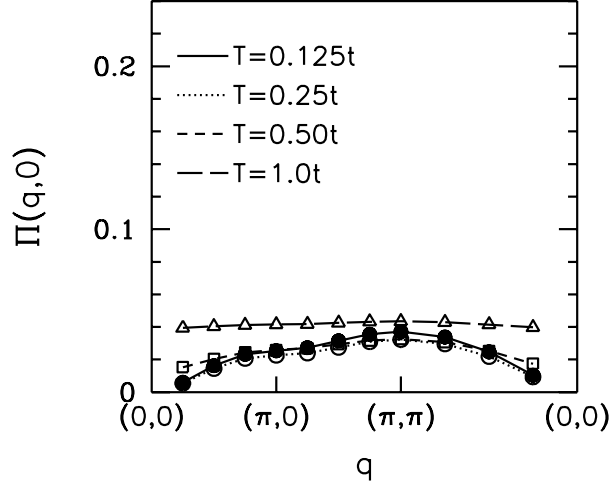
Figure 4.1: Momentum dependence of $\Pi(\mathbf{q}, 0)$ at half-filling for $U = 8t$ and various temperatures.

The evolution of the $\mathbf{q}$ structure in $\Pi(\mathbf{q}, 0)$ with $U/t$ is shown in Fig. 4.3(a) for $T = 0.5t$ and $\langle n \rangle = 0.87$. For comparison, in Fig. 4.3(b) results are shown for $\Pi_0(\mathbf{q}, i\omega_m = 0)$ of the $U = 0$ system given by

$$\Pi_0(\mathbf{q}, i\omega_m) = 2\frac{1}{N} \sum_{\mathbf{p}} \frac{f(\varepsilon_{\mathbf{p}+\mathbf{q}}) - f(\varepsilon_{\mathbf{p}})}{i\omega_m - (\varepsilon_{\mathbf{p}+\mathbf{q}} - \varepsilon_{\mathbf{p}}) + i\delta}. \tag{4.3}$$

In this figure, the solid curve represents $\Pi_0(\mathbf{q}, 0)$ for $\langle n \rangle = 0.87$ and the dotted curve is for $\langle n \rangle = 1.74$, which corresponds to $\Pi(\mathbf{q}, 0)$ of the noninteracting spinless-fermion system for $\langle n \rangle = 0.87$. As $U/t$ increases, it is seen that $\Pi(\mathbf{q}, 0)$ develops features which are more similar to those seen for the noninteracting spinless-fermion system. In Fig. 4.3(a), it is seen that the peak in $\Pi(\mathbf{q}, 0)$ shifts from $\mathbf{q} = (\pi, \pi)$ to $\mathbf{q} \sim 0$ as $U/t$ increases. It is not possible to obtain this type of momentum dependence for $\Pi(\mathbf{q}, 0)$ from the simple RPA form

$$\Pi_{\text{RPA}}(\mathbf{q}, i\omega_m) = \frac{\Pi_0(\mathbf{q}, i\omega_m)}{1 + \frac{1}{2}\overline{U}\Pi_0(\mathbf{q}, i\omega_m)}, \tag{4.4}$$

where $\overline{U}$ is a constant representing the effective coupling in the density channel.

Next, QMC results on $S(\mathbf{q})$ will be discussed. Figure 4.4 shows $S(\mathbf{q})$ versus $\mathbf{q}$ at various temperatures for $U = 8t$. Here, it is seen that $S(\mathbf{q})$ exhibits small variation with $T/t$. Figure 4.5(a) shows the evolution of $S(\mathbf{q})$ with $U/t$ for $T = 0.5t$ and $\langle n \rangle = 0.87$. Here, it is seen that with $U/t$ increasing, $S(\mathbf{q})$ gets suppressed. However, in contrast to the case of $\Pi(\mathbf{q}, 0)$, there is no qualitative change in the $\mathbf{q}$ structure of $S(\mathbf{q})$ as $U/t$ increases, and the peak remains at $(\pi, \pi)$. It is useful to compare these QMC results with $S_0(\mathbf{q})$ of the noninteracting system. Figure 4.5(b) shows $S_0(\mathbf{q})$ versus $\mathbf{q}$ at $T = 0.5t$ for $\langle n \rangle = 0.87$ (solid curve) and $\langle n \rangle = 1.74$ (dotted curve). Comparing Figs. 4.5(a) and (b), one observes that the QMC data on $S(\mathbf{q})$ is more similar to $S_0(\mathbf{q})$ for $\langle n \rangle = 0.87$, and the $\mathbf{q}$ structure in $S(\mathbf{q})$ does not follow that of the noninteracting spinless-fermion system. These results on $S(\mathbf{q})$ are consistent with those found by the GFMC technique for the ground state [Becca *et al.* 2000], and by the QMC method at finite temperatures [Chen *et al.* 1994].
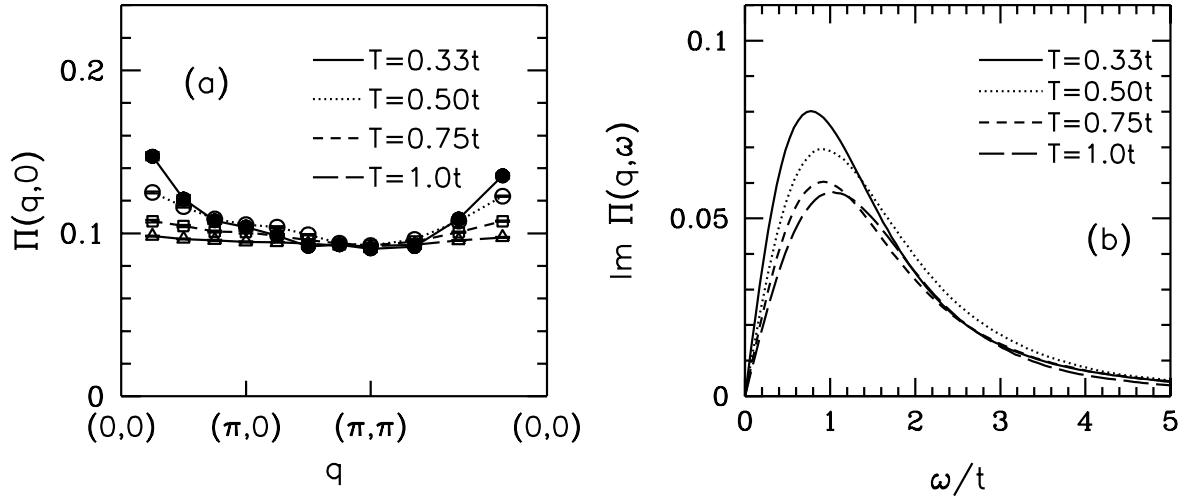
Figure 4.2: (a) Momentum dependence of $\Pi(\mathbf{q}, 0)$. (b) $\text{Im}\,\Pi(\mathbf{q}, \omega)$ versus $\omega$ at $\mathbf{q} = (\pi/4, 0)$. These results are for $\langle n \rangle = 0.87$, $U = 8t$ and various temperatures.
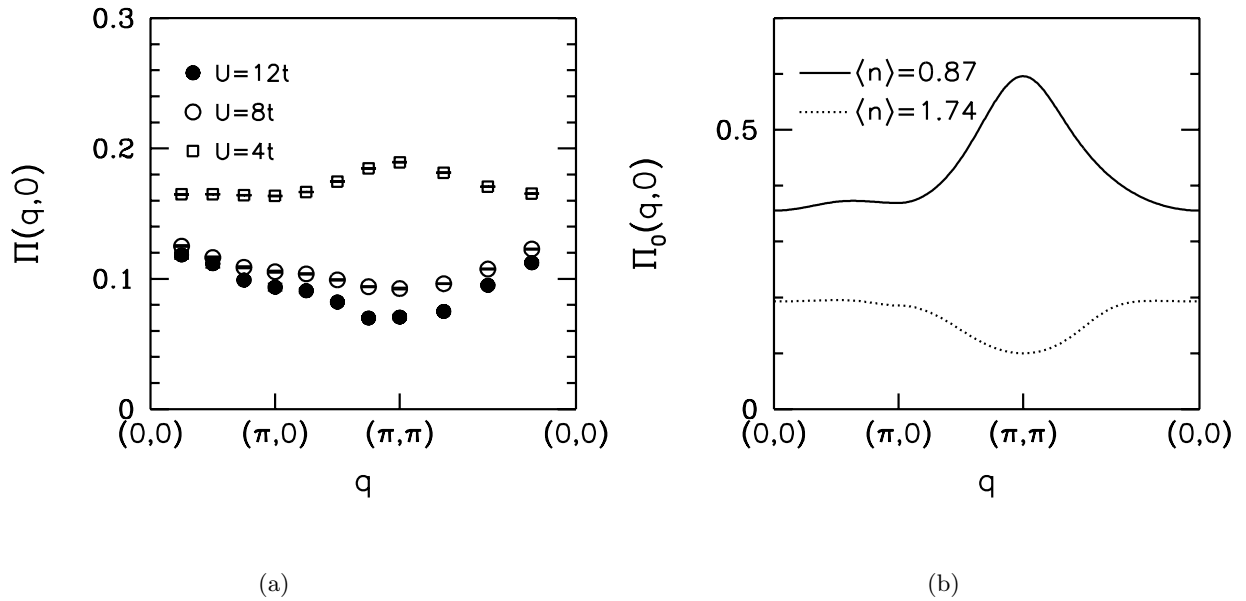


Figure 4.3: (a) $\Pi(\mathbf{q}, 0)$ versus $\mathbf{q}$ at $\langle n \rangle = 0.87$ for various values of $U$. (b) $\Pi_0(\mathbf{q}, 0)$ versus $\mathbf{q}$ for the $U = 0$ system at $\langle n \rangle = 0.87$ (solid curve) and $\langle n \rangle = 1.74$ (dotted curve). These results are for $T = 0.5t$.

19
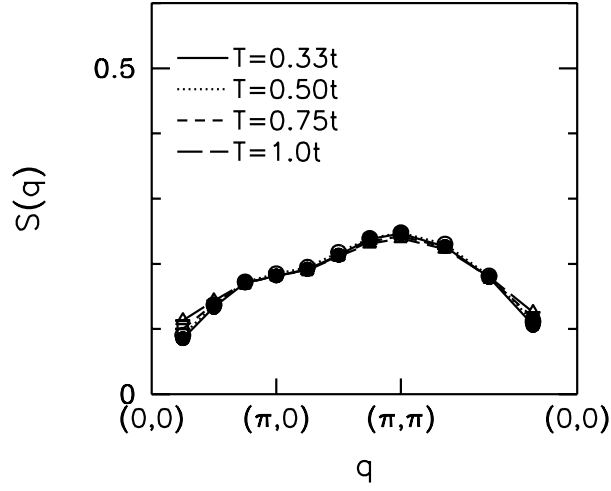
Figure 4.4: Equal-time density correlation function $S(\mathbf{q})$ versus $\mathbf{q}$ at $\langle n \rangle = 0.87$ for $U = 8t$ and various temperatures.



(a)



(b)
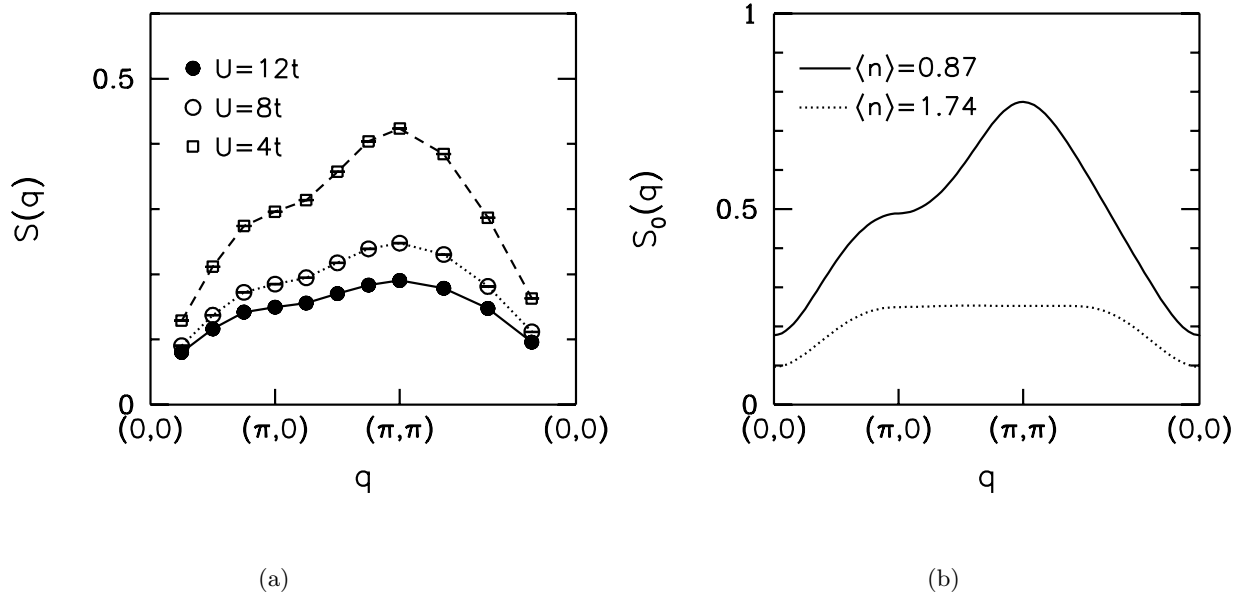
Figure 4.5: (a) $S(\mathbf{q})$ versus $\mathbf{q}$ at $\langle n \rangle = 0.87$ for various values values of $U$. (b) $S_0(\mathbf{q})$ versus $\mathbf{q}$ of the $U = 0$ system for $\langle n \rangle = 0.87$ (solid curve) and $\langle n \rangle = 1.74$ (dotted curve). These results are for $T = 0.5t$.

Here, it has been seen that the results on $S(\mathbf{q})$ for the 2D Hubbard model are quite different from those calculated for the 2D $t$-$J$ model for $J \sim 0.5t$ with the high-temperature series expansion [Putikka *et al.* 1994] or by the GFMC technique [Calandra *et al.* 1998]. In the 2D Hubbard model near half-filling, $S(\mathbf{q})$ does not exhibit obvious features which might be associated with the "$4\mathbf{k}_F$" wave vectors of the Fermi surface. However, $\Pi(\mathbf{q}, 0)$ has structure, which might be associated with the "$4\mathbf{k}_F$" wave vectors, when $U/t$ is large. Hence, the dynamical density fluctuations in 2D Hubbard model with large $U/t$ have features which might be related to the "$4\mathbf{k}_F$" wave vectors, while the static density correlations appear to follow the "$2\mathbf{k}_F$" wave vectors. However, results on $\Pi(\mathbf{q}, \omega)$ at lower temperatures and on bigger lattices are necessary before reaching conclusions.

The nature of the density correlations in the Hubbard model will be discussed further in the remainder of the article. In Section 7.3, comparisons will be made with the 2-leg Hubbard ladder, in which case power-law decaying "$4\mathbf{k}_F$" CDW correlations have been found [Noack *et al.* 1996]. In addition, in Section 8 there will be further comparisons with the density correlations in the 2D $t$-$J$ model.

## 4.2 Optical conductivity

In this section, the results of the numerical calculations on the optical conductivity $\sigma_1(\omega)$ of the 2D Hubbard model will be discussed. The optical conductivity for the 2D Hubbard model was calculated with the exact diagonalization technique for a $4 \times 4$ lattice with $U = 10t$ at half-filling and in the doped case [Dagotto *et al.* 1992c]. In these calculations, the insulating gap in $\sigma_1(\omega)$ at half-filling is clearly seen. Upon doping to $\langle n \rangle = 0.875$, the amount of the spectral weight above the insulating gap is reduced. In this case, the additional features found in $\sigma_1(\omega)$ are a Drude peak at $\omega = 0$ and spectral weight induced at intermediate energies. The Drude weight of the Hubbard model was also calculated with the QMC simulations [Scalapino *et al.* 1992 and 1993]. A review of the exact diagonalization calculations for $\sigma_1(\omega)$ and of comparisons with the experimental data on the cuprates can be found in Ref. [Dagotto 1994].

The real part of the frequency-dependent $\mathbf{q} = 0$ conductivity is given by

$$\sigma_1(\omega) = \mathrm{Re} \left. \frac{\Lambda_{xx}(i\omega_m)}{i\omega_m} \right|_{i\omega_m \to \omega + i\delta} \tag{4.5}$$

where the current-current correlation function $\Lambda_{xx}$ is defined as

$$\Lambda_{xx}(i\omega_m) = \int_0^\beta d\tau \, e^{-i\omega_m \tau} \langle j_x(\tau) j_x(0) \rangle \tag{4.6}$$

with

$$j_x = -itea \sum_{is} (c_{is}^\dagger c_{i+xs} - c_{i+xs}^\dagger c_{is}). \tag{4.7}$$

The analytic continuation in Eq. (4.5) is carried out using the maximum entropy procedure. In the following, the hopping $t$, the electron charge $e$ and the lattice constant $a$ are set to unity.

The solid curve in Fig. 4.6 shows $\sigma_1(\omega)$ versus $\omega$ at half-filling for $U = 8t$, $T = 0.125t$ and an $8 \times 8$ lattice. These are data from Ref. [Bulut *et al.* 1994a]. Here, in spite of the limited resolution of the analytic continuation procedure, the insulating gap in $\sigma_1(\omega)$ is clearly seen. The dotted curve in this graph is the mean-field SDW result given by

$$\sigma_1(\omega) = \frac{2\pi}{N} \sum_{\mathbf{p}} \frac{1}{2} \left( 1 - \frac{\varepsilon_{\mathbf{p}}^2 - \Delta^2}{E_{\mathbf{p}}^2} \right) \left( \frac{1 - 2f(E_{\mathbf{p}})}{E_{\mathbf{p}}} \right) \sin^2 p_x \tag{4.8}$$
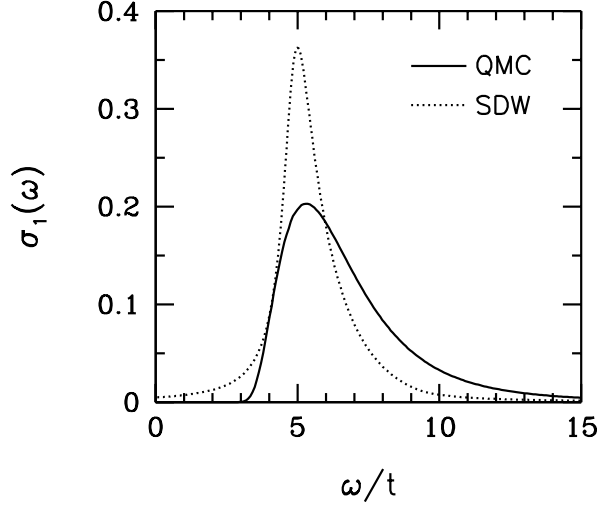
Figure 4.6: Real part of the frequency dependent conductivity of the half-filled Hubbard model with $U = 8t$ (solid curve). These results were obtained for an $8 \times 8$ lattice at $T = 0.125t$. The dotted curve is the mean-field SDW result with $\Delta = 2.4t$. A finite broadening of $\Gamma = 0.5t$ has been used in plotting the SDW result.

which was calculated using $\Delta = 2.4t$. Near the threshold $\omega \simeq 2\Delta$, the SDW coherence factor $\frac{1}{2}[1 - (\varepsilon_{\mathbf{p}}^2 - \Delta^2)/E_{\mathbf{p}}^2]$ in Eq. 4.8 goes to 1 for $\varepsilon_{\mathbf{p}}$ near zero, and hence the peak at the threshold does not vanish within SDW. A check of the maximum entropy analytic continuation is the $f$-sum rule which has the form

$$\int_0^\infty d\omega\, \sigma_1(\omega) = \frac{\pi}{2}\langle -k_x \rangle, \tag{4.9}$$

where $\langle k_x \rangle$ is the average kinetic energy per site associated with hopping in the $x$ direction. The area under the solid curve in Fig. 4.6 is 0.74, where the separate QMC measurement of $\frac{\pi}{2}\langle -k_x \rangle$ gives 0.77. The difference reflects the difficulty in analytically continuing the numerical data. When the system is doped, it is difficult to estimate the accuracy of the analytic continuation procedure for $\sigma_1(\omega)$, especially in the limit $\omega \to 0$. Hence, away from half-filling, the maximum entropy or the Pade techniques were not used to extract $\sigma_1(\omega)$ or the dc resistivity $\rho(T)$ from the QMC data on the current-current correlation function $\Lambda_{xx}$.

Even though it has not been possible to reliably extract $\rho(T)$ for the 2D Hubbard model, for 2D $t$-$J$ clusters $\sigma_1(\omega)$ and $\rho(T)$ were calculated at various fillings by using the finite-temperature Lanczos technique [Jaklic and Prelovsek 2000]. For $J/t = 0.3$, the results for $\sigma_1(\omega)$ and $\rho(T)$ were compared with the experimental data on cuprates in various doping regimes. In some cases, the agreement obtained with the experimental data was at a quantitative level. In the intermediate doping regime, where $0.75 < \langle n \rangle < 0.85$, it was shown that $\sigma_1(\omega)$ is not consistent with the usual Drude form but rather with the marginal Fermi liquid concept where the only $\omega$ scale is given by $T$ [Varma *et al.* 1989]. The finite-temperature Lanczos calculations find also that $\rho(T)$ is proportional to $T$ in this regime but the slope of $\rho(T)$ changes at $T \sim J$. The underdoped and the overdoped regimes were also studied with this technique. Jaklic and Prelovsek concluded that the main features of the unusual normal state properties of the cuprates could be attributed to the

large degeneracy of states and the frustration induced by doping the antiferromagnet.

# 5  Single-particle properties of the 2D Hubbard model

The angular-resolved photoemission spectroscopy (ARPES) measurements on the high-$T_c$ cuprates probe the single-particle properties of these compounds and have found a number of interesting features. In the normal state of the optimally doped cuprates, the ARPES experiments have found that there are quasiparticle-like bands which cross the Fermi level leading to a large Fermi surface. An unusual feature is that these bands have extended flat dispersion near the $(\pi, 0)$ and $(0, \pi)$ points in the Brillouin zone [Dessau *et al.* 1993, Gofron *et al.* 1993]. The ARPES experiments have also provided valuable information about the evolution of the single-particle spectral weight with doping in the underdoped regime as the insulating state is approached. Reviews of these experiments can be found in Refs. [Shen and Dessau 1995, Damascelli *et al.* 2001]. Below, the numerical studies of the single-particle spectral weight in the 2D Hubbard model will be reviewed. In particular, the origin of the correlated metallic band which develops at the Fermi level upon doping the AF Mott-Hubbard insulator will be investigated. It will be seen that the 2D Hubbard model provides an explanation for some of the features found in the ARPES data.

The single-particle properties of the 2D Hubbard model were studied with various many-body techniques. The single-particle spectral weight was calculated phenomenologically by taking into account the scattering of the quasiparticles by the AF spin fluctuations [Kampf and Schrieffer 1990a and 1990b]. The evolution of the single-particle spectral weight with doping was also studied with the exact diagonalization technique [Dagotto *et al.* 1991]. There have been extensive numerical calculations of $A(\mathbf{p}, \omega)$ by analytically continuing the QMC data on the imaginary-time single-particle Green's function [White *et al.* 1989c, White 1991, Vekic and White 1993, Bulut *et al.* 1994a, Bulut and Scalapino 1995, Moreo *et al.* 1995, Haas *et al.* 1995, Duffy and Moreo 1995, Preuss *et al.* 1995 and 1997, Gröber *et al.* 2000]. In these studies, the maximum-entropy technique has been the main algorithm for the analytic continuation procedure. This technique was also used for calculating $A(\mathbf{p}, \omega)$ for the three-band $CuO_2$ model [Dopf *et al.* 1992b] and the one-dimensional Hubbard model [Preuss *et al.* 1994, Zacher *et al.* 1998]. These studies have provided valuable information about the single-particle spectral weight in the Hubbard model. In the following, the maximum-entropy results on the 2D Hubbard model will be reviewed. Here, the emphasis will be on the narrow correlated band which forms at the Fermi level upon doping the insulator, and on the flat bands which are observed near the $(\pi, 0)$ and $(0, \pi)$ points in the Brillouin zone.

The single-particle spectral weight $A(\mathbf{p}, \omega)$ is given by

$$A(\mathbf{p}, \omega) = -\frac{1}{\pi} \text{Im}\, G(\mathbf{p}, i\omega_n \to \omega + i\delta) \tag{5.1}$$

where

$$G(\mathbf{p}, i\omega_n) = \int_0^\beta d\tau\, e^{i\omega_n \tau}\, G(\mathbf{p}, \tau) \tag{5.2}$$

and

$$G(\mathbf{p}, \tau) = -\langle T\, c_{\mathbf{p}\sigma}(\tau) c_{\mathbf{p}\sigma}^\dagger(0) \rangle. \tag{5.3}$$

With the maximum-entropy technique, one uses the QMC data on $G(\mathbf{p}, \tau)$ to invert the integral equation

$$G(\mathbf{p}, \tau) = -\int_{-\infty}^\infty d\omega\, \frac{e^{-\omega\tau}}{1 + e^{-\beta\omega}}\, A(\mathbf{p}, \omega), \tag{5.4}$$

in order to obtain $A(\mathbf{p}, \omega)$. By applying the same procedure to

$$G_{ii}(\tau) = -\langle T\, c_{i\sigma}(\tau)c_{i\sigma}^\dagger(0)\rangle, \tag{5.5}$$

the single-particle density of states $N(\omega)$ is obtained. The maximum-entropy technique for analytically continuing QMC data is described in Refs. [Silver *et al.* 1990, Jarrell and Gubernatis 1996]. The statistical errors for $G_{ii}(\tau)$ are smaller than for $G(\mathbf{p}, \tau)$, hence the results for $N(\omega)$ shown below have higher resolution. Here, first the results on the evolution of $N(\omega)$ with doping will be reviewed, and later $A(\mathbf{p}, \omega)$ will be discussed. In the following, $N(\omega)$ and $A(\mathbf{p}, \omega)$ will be plotted in units of $t^{-1}$. The data which will be shown in this section are from Refs. [Bulut *et al.* 1994a, Bulut and Scalapino 1995].
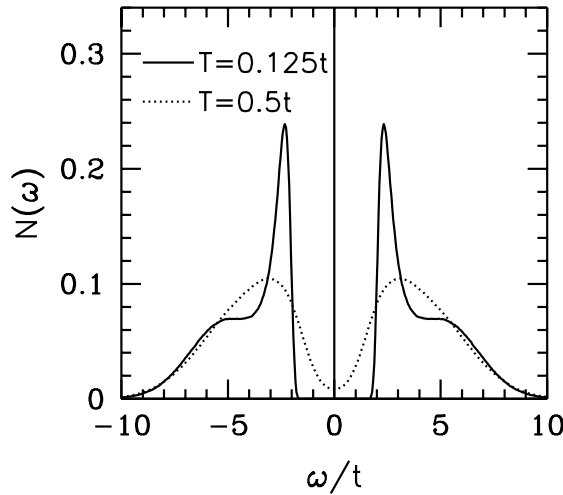


Figure 5.1: Single-particle density of states $N(\omega)$ versus $\omega$. These results were obtained for $U = 8t$ and $\langle n \rangle = 1.0$ on a $12 \times 12$ lattice.

## 5.1 Single-particle density of states

Figure 5.1 shows the single-particle density of states $N(\omega)$ versus $\omega$ at half-filling for $U = 8t$ on a $12 \times 12$ lattice at $T = 0.5$ and $0.125t$. Here, the chemical potential $\mu$ is located at $\omega = 0$. In this figure, it is seen that at $T = 0.5t$, $N(\omega)$ consists of two peaks corresponding to the lower and the upper Hubbard bands, which are separated by the Mott-Hubbard pseudogap. At this temperature, the AF correlation length is still less than the system size, as it was seen in Section 3.1. As $T$ is lowered down to $0.125t$, the AF correlation length reaches the system size, and in this case additional sharp peaks appear at the upper edge of the lower Hubbard band and at the lower edge of the upper Hubbard band. At $T = 0.125t$, the pseudogap has become a full gap in the single-particle spectrum with a magnitude of $2\Delta \approx 4.5t$. The size of the gap $2\Delta$ was also calculated within an SDW approach where the single-particle self-energy corrections were included [Schrieffer *et al.* 1989]. Within this approach, for $U = 8t$, $2\Delta$ is found to be about $4.8t$, while for $U = 4t$, $2\Delta$ is about $2t$.

The sharp peaks which are located below and above the Mott-Hubbard gap appear when the system has long-range AF order. These narrow bands have a bandwidth of about $1t$, corresponding to $\approx 2J$ where $J = 4t^2/U$, and they exhibit SDW-like dispersion, which will be discussed in the next section. It is known that in the half-filled 2D $t$-$J$ model the quasiparticle bandwidth is about $2J$ [Liu and Manousakis 1992]. The exact diagonalization calculations for the 2D $t$-$J$ model also find SDW-like quasiparticle excitations with a bandwidth of about $2.2J$ at half-filling [Dagotto 1994]. In the $t$-$J$ model at half-filling, one doped hole propagates by flipping the spins in the AF background around it. For this reason, the bandwidth for the hole motion is determined by the magnetic exchange $J$ rather than the hopping matrix element $t$. The QMC data implies that the hole propagation is accompanied by similar many-body processes in the half-filled 2D Hubbard model.
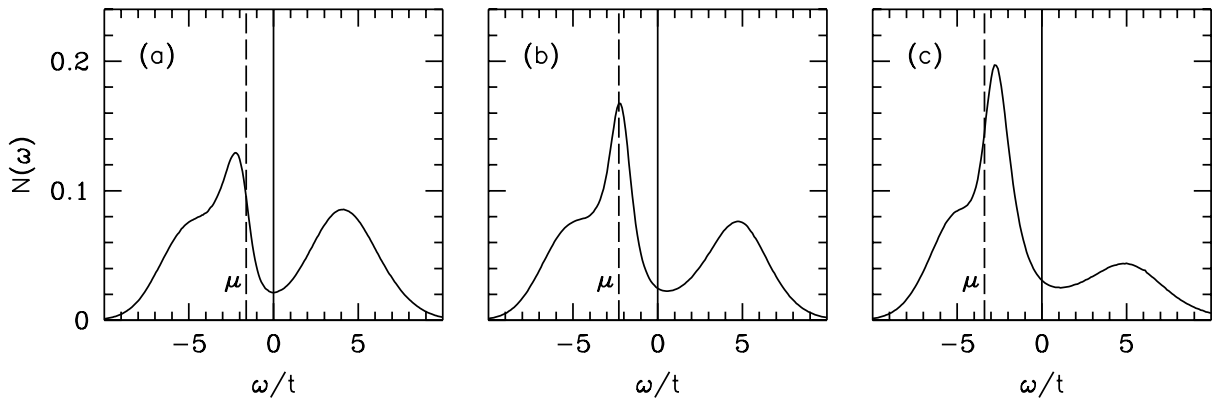


Figure 5.2: Single-particle density of states $N(\omega)$ versus $\omega$ at fillings (a) $\langle n \rangle = 0.94$, (b) 0.87 and (c) 0.70. These results are for $T = 0.5t$ and $U = 8t$.

Next, results on the evolution of $N(\omega)$ with doping are shown. Figure 5.2 shows $N(\omega)$ versus $\omega$ at fillings $\langle n \rangle = 0.94$, 0.87 and 0.70 for $U = 8t$ and $T = 0.5t$. Upon hole doping, the chemical potential moves rapidly from $\omega = 0$ to the top of the lower Hubbard band. This is accompanied with a gradual transfer of spectral weight from above the Mott-Hubbard gap to the Fermi level. The transferred spectral weight goes into forming a narrow metallic band at the Fermi level. These data are in agreement with the exact diagonalization calculations [Dagotto $et$ $al.$ 1991]. In the overdoped regime at $\langle n \rangle = 0.70$, the Fermi level lies below the metallic band. The temperature variation of $N(\omega)$ is shown in Fig. 5.3 for $\langle n \rangle = 0.87$ and $U = 8t$. Here, the build up of a narrow band with a width between $4J$ and $5J$ is clearly seen as $T$ decreases. The comparison of Figs. 5.3 and 5.1 indicates that this correlated metallic band forms out of the SDW-like bands of the half-filled case.

At this point, it should be noted that the general features of $N(\omega)$ seen in Fig. 5.3 are similar to what is found for the infinite-dimensional Hubbard model away from half-filling [Jarrell 1992]. $N(\omega)$ for the infinite-dimensional Hubbard model is calculated by first mapping the model to an Anderson impurity problem, which is then solved exactly. In this case, a narrow peak at the Fermi level is also found in addition to the lower and upper Hubbard bands.

It is useful to compare these results on $N(\omega)$ for $U = 8t$ with the results for $U = 4t$ and $12t$, which are shown in Fig. 5.4. For $U = 12t$, the narrow metallic band is further separated from the lower and the upper Hubbard bands, and the pseudogap is bigger. On the other hand, for $U = 4t$, the pseudogap is not observed at these temperatures, even though there are hump-like structures
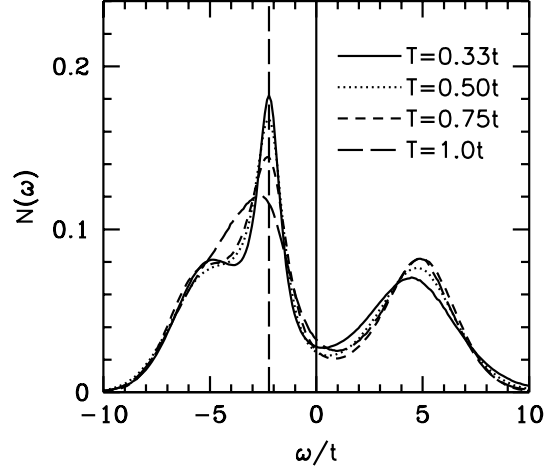
Figure 5.3: Development of the single-particle density of states $N(\omega)$ as the temperature is lowered for $\langle n \rangle = 0.87$ and $U = 8t$.
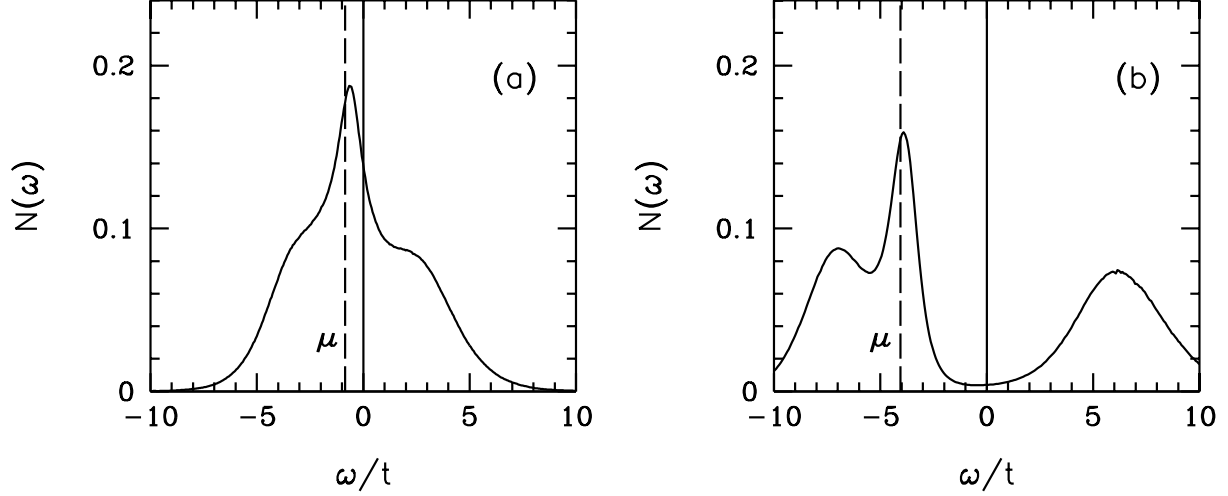


Figure 5.4: $N(\omega)$ versus $\omega$ for (a) $U = 4t$ and (b) $U = 12t$ at $\langle n \rangle = 0.87$ and $T = 0.5t$.

which might be attributed to the lower and the upper Hubbard bands. In addition, the peak at the Fermi level is broader. Hence, as $U$ increases from $4t$ to $12t$, the distribution of the weight in $N(\omega)$ changes considerably. However, the density of states at the Fermi level $N(\mu)$ varies by a small amount.

It is also useful to discuss how $N(\mu)$ varies with doping at fixed $U$ and $T$. Figure 5.5 shows

26

$N(\mu)$ versus $\langle n \rangle$ for $U = 8t$ at $T = 0.5t$ (filled circles) and $1.0t$ (open circles). It is clearly seen that at these temperatures $N(\mu)$ has a peak at finite doping, and a depression in $N(\mu)$ exists near half-filling. However, it is not possible to extract the $T \to 0$ behavior.
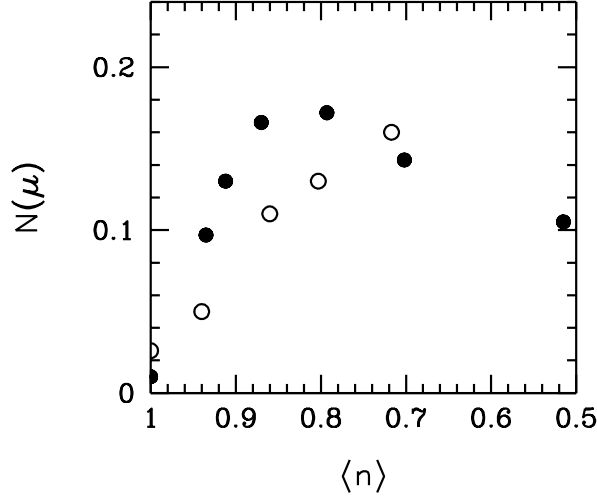


Figure 5.5:    Filling dependence of the density of states at the Fermi level $N(\mu)$ for $U = 8t$ at temperatures $T = 0.5t$ (filled circles) and $1.0t$ (open circles).

## 5.2   Single-particle spectral weight

In this section, results on the single-particle spectral weight $A(\mathbf{p}, \omega)$ will be discussed. It is useful to first study the effects of varying $U$ on $A(\mathbf{p}, \omega)$. Figure 5.6 shows $A(\mathbf{p}, \omega)$ versus $\omega$ at various temperatures for $U = 8t$ and $4t$. These results were obtained for the $\mathbf{p} = (\pi/2, \pi/2)$ point on an $8 \times 8$ lattice. For both values of $U$, a heavily-damped quasiparticle-like peak develops near the Fermi level as the temperature decreases. However, for $U = 8t$ this peak is broader and it has reduced weight. In addition, in this case, the peak location varies with the temperature. Even though the maximum-entropy technique has an intrinsic broadening which is difficult to estimate, these results suggest that the damping of the quasiparticles is stronger for larger $U/t$.

In the previous section, it was seen that for $U = 8t$ a narrow metallic band develops at the Fermi level upon doping. In order to gain insight into the origin of this band, in Fig. 5.7, $A(\mathbf{p}, \omega)$ versus $\omega$ is plotted for $\mathbf{p}$ taken along various cuts in the Brillouin zone as indicated in the insets. These data were obtained on a $12 \times 12$ lattice for $U = 8t$, $\langle n \rangle = 0.87$ and T= $0.5t$. In this figure, spectral weight representing the upper and the lower Hubbard bands are seen in addition to a quasiparticle band which crosses the Fermi level. The quasiparticle peak is especially of interest. When $\mathbf{p}$ is on the Fermi surface, this peak is centred at $\omega = 0$. As $\mathbf{p}$ moves outside of the Fermi surface, the quasiparticle peak is clearly resolved. However, when $\mathbf{p}$ is below the Fermi surface, for instance at $\mathbf{p} = (0, 0)$, the quasiparticle peak is obscured by the lower Hubbard band, even though the exact diagonalization calculations [Dagotto $et$ $al.$ 1992a] find a quasiparticle peak at this momentum in addition to the lower Hubbard band. This is because the maximum-entropy algorithm used here has poor resolution when $\omega$ is away from the Fermi level. Indeed, similar calculations with higher
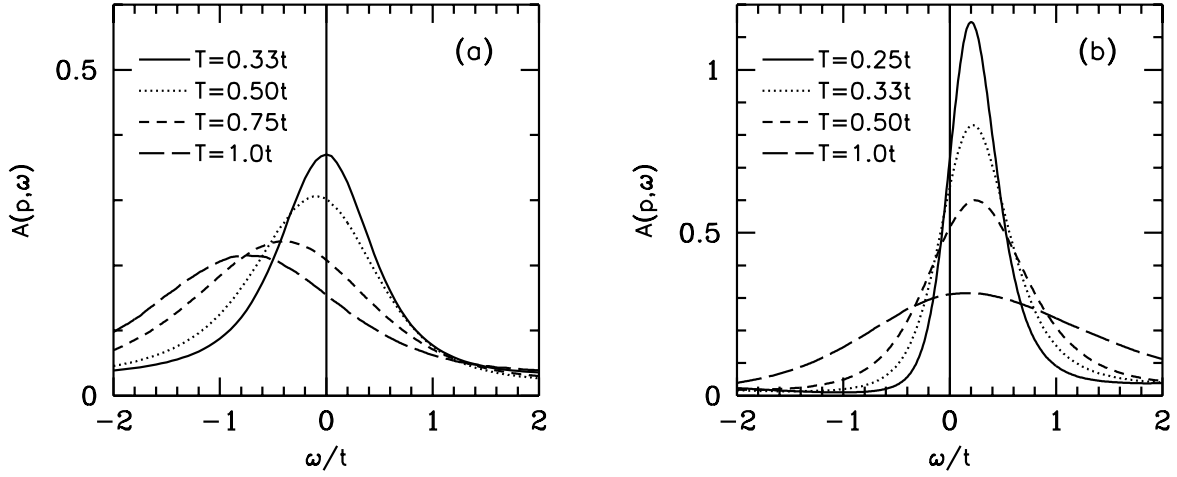
Figure 5.6: Comparison of $A(\mathbf{p} = (\pi/2, \pi/2), \omega)$ versus $\omega$ for (a) $U = 8t$ and (b) $U = 4t$. Here results are shown at various temperatures for $\langle n \rangle = 0.87$, and the frequency axis is shifted such that the Fermi level occurs at $\omega = 0$.

resolution were able to observe the quasiparticle peak below the Fermi surface [Preuss *et al.* 1995]. An unresolved issue is whether the dispersing band near the Fermi level corresponds to a true quasiparticle band. However, the exact determination of the energy and the temperature scaling of the spectral weight cannot be carried out because the maximum-entropy technique has finite resolution and, in addition, bigger lattices and lower temperatures are required.

An important feature of the quasiparticle band is that it is unusually flat near the $(\pi, 0)$ and $(0, \pi)$ points of the Brillouin zone. This causes large amount of spectral weight to be near the Fermi level. Even though the weight in the quasiparticle peak near the Fermi level decreases as $U$ increases from $4t$ to $8t$, the density of states at the Fermi level stays nearly the same. This is because of the flat bands which are pinned near the Fermi level. The presence of the flat bands is especially important because they generate phase space for the scattering of the quasiparticles in the $d_{x^2-y^2}$-wave pairing channel. These features found in the 2D Hubbard model are similar to the ARPES data on the cuprates [Dessau *et al.* 1993, Gofron *et al.* 1993].

In addition to the QMC data, in Ref. [Dagotto *et al.* 1994], the relation with the flat bands seen in the ARPES data were noted by using the dispersion of one hole in the half-filled *t-J* model calculated on a $16 \times 16$ lattice. It should also be noted that Beenen and Edwards have found good agreement with the main features of the QMC data using a two-pole approximation in calculating the single-particle Green's function [Beenen and Edwards 1995]. Dorneich *et al.* have extended this type of calculations for the Hubbard model for the case of $\langle n \rangle = 1$ [Dorneich *et al.* 2000]. Finally, it should be noted that a number of transport measurements on the cuprates have been interpreted in terms of the Fermi level being close to a van Hove singularity [Tsuei *et al.* 1992, Newns *et al.* 1994]. Here, it is seen that in the 2D Hubbard model there can be extended flat bands near the Fermi level and they are produced by the many-body effects rather than being due to the one-electron band structure.
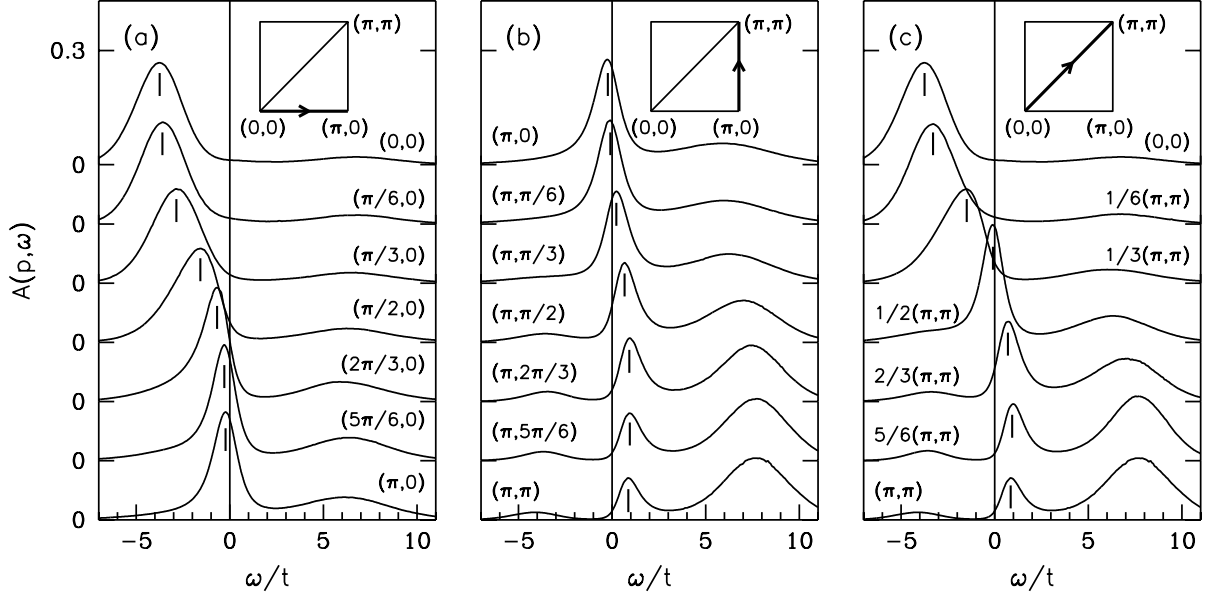
Figure 5.7: Single-particle spectral weight $A(\mathbf{p}, \omega)$ versus $\omega$ for various momentum cuts through the Brillouin zone for $U = 8t$ and $\langle n \rangle = 0.87$. Here, the frequency axis is shifted such that the Fermi level occurs at $\omega = 0$.

These calculations for $A(\mathbf{p}, \omega)$ were also carried out at half-filling, and the results were fitted with the SDW form [Bulut *et al.* 1994a],

$$A(\mathbf{p}, \omega) = u_\mathbf{p}^2 \delta(\omega - E_\mathbf{p}) + v_\mathbf{p}^2 \delta(\omega + E_\mathbf{p}) \tag{5.6}$$

where $u_\mathbf{p}^2 = \frac{1}{2}(1 + \gamma_\mathbf{p}/E_\mathbf{p})$, $v_\mathbf{p}^2 = \frac{1}{2}(1 - \gamma_\mathbf{p}/E_\mathbf{p})$, $\gamma_\mathbf{p} = -2t(\cos p_x + \cos(p_y))$, and $E_\mathbf{p} = \sqrt{\gamma_\mathbf{p}^2 + \Delta^2}$, For large $\Delta/t$,

$$E_\mathbf{p} = \sqrt{\gamma_\mathbf{p}^2 + \Delta^2} \simeq \Delta + J(\cos p_x + \cos p_y)^2. \tag{5.7}$$

Similar calculations with higher resolution [Preuss *et al.* 1995] were carried out, which showed that, in fact, the spectrum is better described by $E_\mathbf{p} \simeq \Delta + \frac{J}{2}(\cos p_x + \cos p_y)^2$, hence, the quasiparticle band at half-filling has a width of $2J$ in agreement with the results on $N(\omega)$ at half-filling and with the calculations on the $t$-$J$ model with one hole.

Based on the results discussed above, schematic dispersion relations were constructed for the 2D Hubbard model, which are shown in Fig. 5.8 for $\langle n \rangle = 0.87$ and $\langle n \rangle = 1.0$. In Fig. 5.8(a), the dashed horizontal line represents the chemical potential, and the solid curve denotes the narrow metallic band located at the Fermi level. The shaded regions represent the lower and the upper Hubbard bands. The width of the quasiparticle band is of order $4J$. Figure 5.8(b) illustrates the distribution of the spectral weight at half-filling. Here, the solid and the dotted lines denote the SDW-like quasiparticle bands. The picture which emerges from these calculations is that the narrow metallic band which lies at the Fermi level for $\langle n \rangle = 0.87$ forms out of the SDW-like bands which exist in the half-filled case.

The QMC results seen in Fig. 5.7 were obtained at $T = 0.5t$ for $\langle n \rangle = 0.87$, where the AF correlation length $\xi$ is less than one lattice spacing. The QMC simulations were also carried out

29

at $T = 0.25t$ for $\langle n \rangle = 0.93$, where $\xi$ is about 1.2 lattice spacing [Preuss *et al.* 1997]. In this case, spectral weight has been observed at wave vectors which are displaced by $\mathbf{Q} = (\pi, \pi)$ with respect to the narrow metallic band at the Fermi level. These results are consistent with the calculations where "shadow bands" due to the scattering of the quasiparticles by the AF spin fluctuations were found [Kampf and Schrieffer 1990b]. This type of shadow structures were also observed in the photoemission experiments [Aebi *et al.* 1995]. Detailed single-particle spectra in the low-doping regime of the 2D Hubbard model were obtained recently [Gröber *et al.* 2000].



(a)                                                                (b)
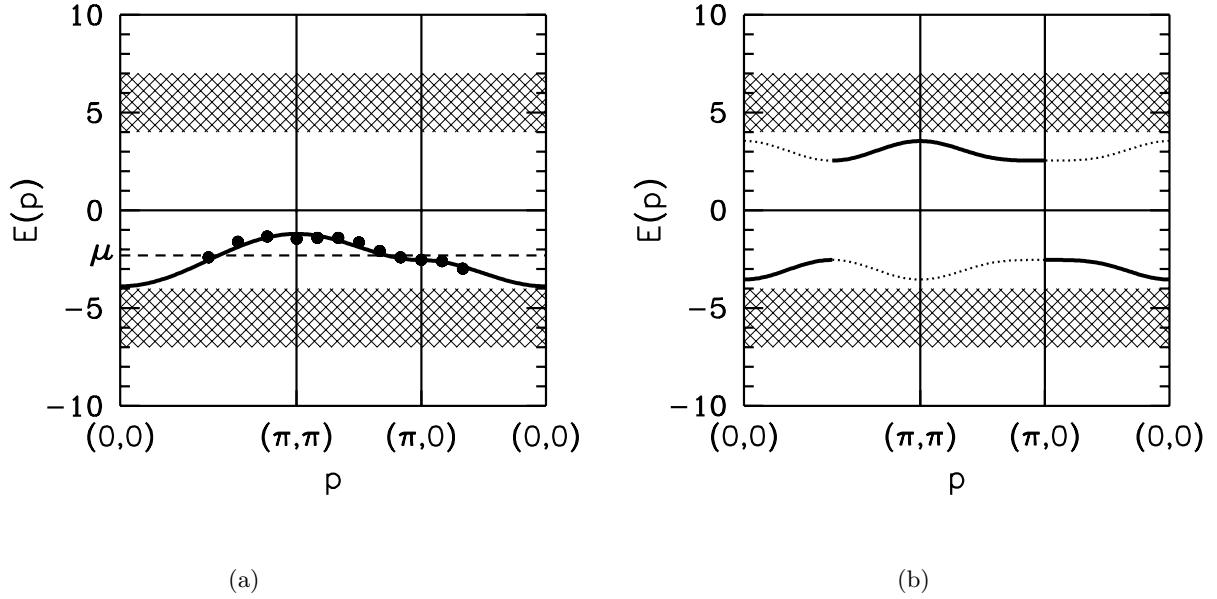
Figure 5.8:   Schematic drawing of $E_{\mathbf{p}}$ versus $\mathbf{p}$ at $U = 8t$ for (a) $\langle n \rangle = 0.87$ and (b) $\langle n \rangle = 1.0$. Here, the shaded areas represent the lower and the upper Hubbard bands, and the solid and the dotted curves indicate the quasiparticle bands. In (a), the solid points indicate the position of the quasiparticle peak obtained from Fig. 5.7 when the quasiparticle peak is not obscured by the lower Hubbard band, and the horizontal dashed line denotes the chemical potential $\mu$.

In this section, it was seen that the single-particle properties in the 2D Hubbard model are determined by the AF spin fluctuations and the Coulomb correlations. An especially important feature of the single-particle spectral weight is the flat bands near $\mathbf{p} = (\pi, 0)$ and $(0, \pi)$. They create large amount of phase space for the scattering of the quasiparticles in the $d_{x^2-y^2}$-wave pairing channel. In Section 7, it will be seen that similar flat bands exist in the 2-leg Hubbard ladder, and they play a key role in determining the strength of the $d_{x^2-y^2}$-like superconducting correlations in this system. In Section 8.1, these QMC results on the single-particle spectral weight will be compared with those obtained from the FLEX approximation, and the implications for the $d_{x^2-y^2}$-wave pairing in the 2D Hubbard model will be discussed.

# 6 Pairing correlations in the 2D Hubbard model

An important question for the high-$T_c$ cuprates is whether the 2D Hubbard model exhibits super-conductivity, and if does, what is the nature of the pairing. Various views were expressed on this subject, and some of them are as follows. In one view, the effective interaction between the particles is dominated by the exchange of an AF spin fluctuation, and this leads to $d_{x^2-y^2}$-wave pairing [Bickers *et al.* 1987]. In an alternative view, the magnetic correlations are responsible for the pairing, but it is because of the "bag effect" which leads to pairing with the extended $s$ or the $d_{x^2-y^2}$-wave symmetry [Schrieffer *et al.* 1988 and 1989]. In this approach, the effective pairing interaction is qualitatively different than the single spin-fluctuation exchange interaction. Another view is that in the ground state of the doped 2D Hubbard model there are no single-particle excitations carrying both charge and spin and the one-layer Hubbard model does not exhibit superconductivity [Anderson 1987, Anderson *et al.* 1987, Anderson and Zou 1988]. In this view, the pairing is mediated by interlayer hopping. In order to differentiate among these theories, QMC simulations were carried out for the 2D Hubbard model. In this section, these QMC calculations will be reviewed.

In Section 6.1, the QMC results on the pair-field susceptibilities will be reviewed. These calculations have found that there is an effective attractive interaction in the singlet $d_{x^2-y^2}$-wave channel [White *et al.* 1989a]. In addition, it is found that there is an attractive interaction in the extended $s$-wave channel. However, at the temperatures where the simulations are carried out, the pairing correlations are short range and do not show scaling with the lattice size [Moreo and Scalapino 1991, Moreo 1992]. QMC simulations were also carried out for the pair-field susceptibilities in the three-band $CuO_2$ model and similar results were found [Scalettar *et al.* 1991, Dopf *et al.* 1992a].

Using QMC simulations, the irreducible particle-particle interaction $\Gamma_I$ was calculated [Bulut *et al.* 1993, 1994b, 1995] and these results will be reviewed in Section 6.2. In these calculations, it is found that the momentum and the Matsubara-frequency structure in $\Gamma_I$ follows closely that of the magnetic susceptibility, which means that the AF spin fluctuations dominate the effective interaction in the parameter regime where the simulations are carried out. In Section 6.3, the Bethe-Salpeter equation in the particle-particle channel will be solved using the QMC data on $\Gamma_I$ and the single-particle Green's function $G$. The solution of the Bethe-Salpeter equation makes it possible to determine the strength of the various pairing channels quantitatively. Finite-size scaling of these results shows that as $T$ is lowered, the fastest growing pairing instability is in the singlet $d_{x^2-y^2}$-wave channel. Here, it is also found that as $U/t$ increases from 4 to 8, the strength of the $d_{x^2-y^2}$ pairing correlations grows. Later in Section 8.1, these calculations will be compared with the results of the FLEX approximation. In Section 6.4, the results on $\Gamma_I$ will be compared with the single spin-fluctuation exchange approximation. In Section 6.5, comparisons will be made with the perturbation theory results for $\Gamma_I$, which are third order in $U$. These comparisons are useful for gaining insight into the effects of the various subgroups of many-body scattering processes contributing to $\Gamma_I$.

## 6.1 Pair-field susceptibilities

In order to study the pairing correlations in the 2D Hubbard model, the pair-field susceptibilities defined by

$$P_\alpha = \int_0^\beta d\tau \, \frac{1}{N} \sum_\ell \langle \Delta_\alpha(\ell, \tau) \Delta_\alpha^\dagger(0, 0) \rangle, \tag{6.1}$$

where $\Delta_\alpha^\dagger$ is a pair creation operator with $\alpha$ symmetry, were calculated. The QMC calculations of the pair-field susceptibilities for the Hubbard model were first carried out in Ref. [Hirsch 1985]. In
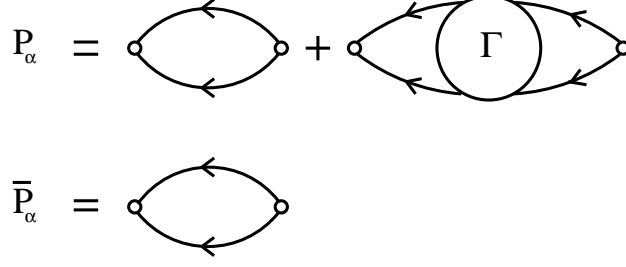
Figure 6.1: Feynman diagrams illustrating the pair-field susceptibilities (a) $P_\alpha$ and (b) $\overline{P}_\alpha$. Here, $\Gamma$ represents the reducible particle-particle interaction.

these calculations, it was found that there is an attractive effective interaction between two electrons with antiparallel spins when they are separated by one lattice spacing. In this reference, the pair-field susceptibilities in the singlet $s$ and extended $s$-wave ($s^*$) channels and the triplet channels were calculated, however the singlet $d_{x^2-y^2}$-wave channel was not considered. Later in Ref. [White $et$ $al.$ 1989a], various pair-field susceptibilities including the one with the singlet $d_{x^2-y^2}$-wave symmetry were calculated with QMC. In this section, results from Ref. [White $et$ $al.$ 1989a] will be shown for $P_\alpha$ which were calculated using the following pair-field operators in the $d_{x^2-y^2}$, $s$, extended $s$ ($s^*$) and $p$-wave channels,

$$\Delta_d^\dagger = \frac{1}{4}\sum_{\ell=1}^{4}(-1)^\ell c_{i+\ell\uparrow}^\dagger c_{i\downarrow}^\dagger, \tag{6.2}$$

$$\Delta_s^\dagger = c_{i\uparrow}^\dagger c_{i\downarrow}^\dagger, \tag{6.3}$$

$$\Delta_{s^*}^\dagger = \frac{1}{4}\sum_{\ell=1}^{4} c_{i+\ell\uparrow}^\dagger c_{i\downarrow}^\dagger, \tag{6.4}$$

$$\Delta_{p_x}^\dagger = \frac{1}{2}(c_{i+\mathbf{x}\uparrow}^\dagger c_{i\downarrow}^\dagger - c_{i-\mathbf{x}\uparrow}^\dagger c_{i\downarrow}^\dagger). \tag{6.5}$$

Here $\ell$ sums over the four neighbours of site $i$.

In order to see whether a given pairing channel with the symmetry $\alpha$ is attractive, $P_\alpha$ was compared with $\overline{P}_\alpha$, where $\overline{P}_\alpha$ is the component of $P_\alpha$ which does not include the reducible particle-particle interaction $\Gamma$ as illustrated in Fig. 6.1. Figure 6.2 compares $P_\alpha$ and $\overline{P}_\alpha$ as a function of $T/t$ for $U = 4t$ and $\langle n \rangle = 0.87$ on an $8 \times 8$ lattice. Here, it is seen that $P_\alpha$ is enhanced with respect to $\overline{P}_\alpha$ by the particle-particle reducible vertex for the $d_{x^2-y^2}$-wave and weakly for the extended $s$-wave symmetries. On the other hand, in the $s$- and $p$-wave channels the pair-field susceptibility is suppressed with respect to $\overline{P}_\alpha$. This means that the effective particle-particle interaction is attractive in the $d_{x^2-y^2}$ and $s^*$ channels, and it is repulsive in the $s$ and $p$-wave channels. However, at the lowest temperatures where the QMC simulations can be carried out, the $d_{x^2-y^2}$-wave pairing correlations are only short range: $P_d$ does not grow as the system size increases. Furthermore, while $P_d$ is enhanced with respect to $\overline{P}_d$, it is suppressed with respect to $P_d^0$, the $d_{x^2-y^2}$-wave pair-field susceptibility of the $U = 0$ system, as seen in Fig. 6.2(a). So, at these temperatures, the $d_{x^2-y^2}$-wave pair-field susceptibility gets suppressed when the Coulomb repulsion is turned on, which is not encouraging for $d_{x^2-y^2}$-wave superconductivity in the 2D Hubbard model.
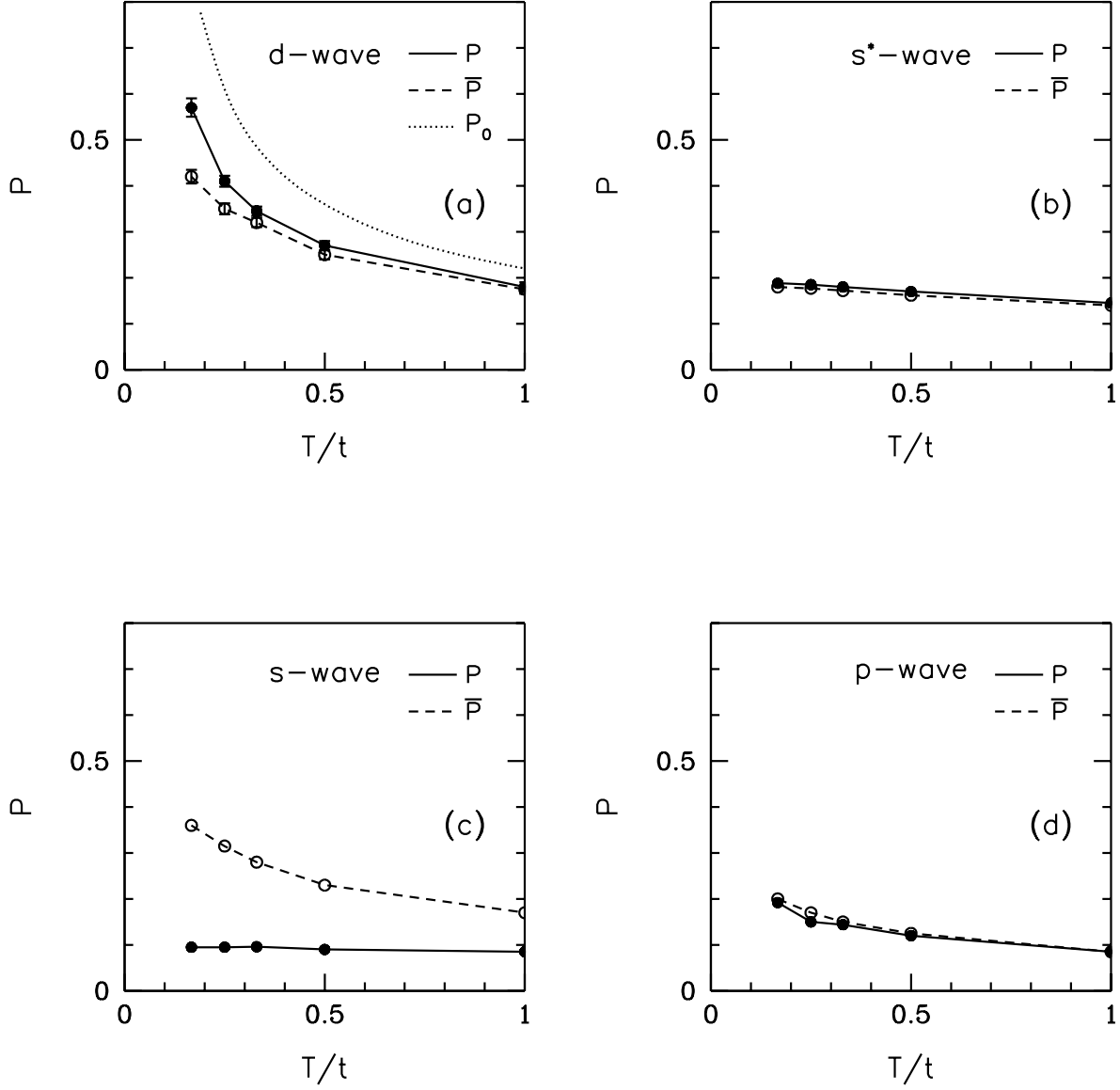
Figure 6.2: Pair-field susceptibilities $P_\alpha$ and $\overline{P}_\alpha$ versus $T/t$ for the $d_{x^2-y^2}$, $s^*$, $s$ and $p$-wave pairing channels. These results are for $U = 4t$ and $\langle n \rangle = 0.87$ on an $8 \times 8$ lattice. In (a), $P_0$ denotes the $d_{x^2-y^2}$-wave pair-field susceptibility of the $U = 0$ system. From [White $et$ $al.$ 1989a].
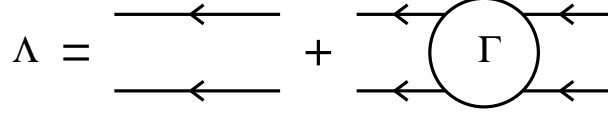
Figure 6.3: Feynman diagrams illustrating the correlation function $\Lambda(p', k'|p, k)$ in terms of the single-particle Green's functions $G$ and the reducible particle-particle interaction $\Gamma$.

## 6.2 Irreducible particle-particle interaction

In this section, the QMC data on the irreducible particle-particle vertex $\Gamma_I$ from Ref. [Bulut *et al.* 1993, 1994b, 1995] will be reviewed. Using QMC simulations it is possible to calculate the two-particle Green's function

$$\Lambda(x_4, x_3|x_2, x_1) = -\langle T\, c_\uparrow(x_4) c_\downarrow(x_3) c_\downarrow^\dagger(x_2) c_\uparrow^\dagger(x_1)\rangle, \tag{6.6}$$

where $c_\sigma^\dagger(x_i)$ with $x_i = (\mathbf{x}_i, \tau_i)$ creates an electron with spin $\sigma$ at site $\mathbf{x}_i$ and imaginary time $\tau_i$. By Fourier transforming on both the space and the imaginary-time variables one obtains

$$\Lambda(p', k'|p, k) = -\delta_{pp'}\delta_{kk'}G_\uparrow(p)G_\downarrow(k) + \frac{T}{N}\delta_{k', p+k-p'}G_\uparrow(p')G_\downarrow(k')\Gamma(p', k'|p, k)G_\uparrow(p)G_\downarrow(k), \tag{6.7}$$

where $p = (\mathbf{p}, i\omega_n)$, $G_\sigma(p)$ is the single-particle Green's function, and $\Gamma(p', k'|p, k)$ is the reducible particle-particle vertex. Hence, using the QMC data on $\Lambda$ and $G$, $\Gamma$ can be calculated. This equation is illustrated in Fig. 6.3 in terms of the Feynman diagrams. Here, the particle-particle interaction will be studied in the zero center-of-mass momentum and energy channel, and hence $k$ and $k'$ will be set to $-p$ and $-p'$, respectively. At the next stage, the irreducible particle-particle vertex $\Gamma_I$ is obtained from the Monte Carlo results on $\Gamma$ and $G$ by solving the particle-particle $t$-matrix equation,

$$\Gamma_I(p'|p) = \Gamma(p'|p) + \frac{T}{N}\sum_k \Gamma_I(p'|k)G_\uparrow(k)G_\downarrow(-k)\Gamma(k|p), \tag{6.8}$$

which is illustrated in Fig. 6.4. In Eq. (6.8), $\Gamma(p'|p)$ is used as a short notation for $\Gamma(p', -p'|p, -p)$. This procedure for calculating $\Gamma_I$ is essentially the opposite of the usual diagrammatic approach in which $\Gamma_I$ is used to solve for $\Gamma$. In solving the $t$-matrix equation, an upper frequency cut-off of order the bandwidth is used. Finally, the singlet component of the irreducible vertex is obtained from

$$\Gamma_{Is}(p'|p) = \frac{1}{2}\left[\Gamma_I(p'|p) + \Gamma_I(-p'|p)\right]. \tag{6.9}$$

In the following, the QMC data on $\Gamma_{Is}$ and $\Gamma_s$ will be plotted in units of $t$ as a function of the momentum transfer $\mathbf{q} = \mathbf{p}' - \mathbf{p}$ and of the Matsubara-frequency transfer $\omega_m = \omega_{n'} - \omega_n$. Here, $\mathbf{p}$ will be kept fixed at $(\pi, 0)$ and $\omega_n$ at $\pi T$.

It is useful to start the discussion by first showing results on the singlet reducible vertex $\Gamma_s$. In Fig. 6.5, $\Gamma_s(\mathbf{q}, i\omega_m = 0)$ versus $\mathbf{q}$ is shown for $U = 4t$ and $8t$. As the temperature is lowered, the $\mathbf{q} \sim (\pi, \pi)$ component of $\Gamma_s$ increases, and the $\mathbf{q} \sim 0$ component is suppressed. Here, it is seen that $\Gamma_s$ becomes quite large especially for $U = 8t$. In Fig. 6.5(b), the $\mathbf{q} = (0, 0)$ point is not shown because of large error bars for this point due to the way $\Gamma$ is calculated from $\Lambda$. It is also not possible to show results at lower temperatures since the error bars grow rapidly. For instance, at
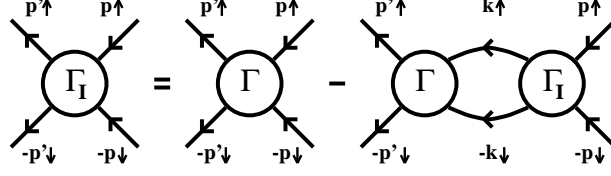
Figure 6.4: Feynman diagrams illustrating the $t$-matrix equation which relates the irreducible particle-particle interaction $\Gamma_I$ to the reducible particle-particle interaction $\Gamma$.
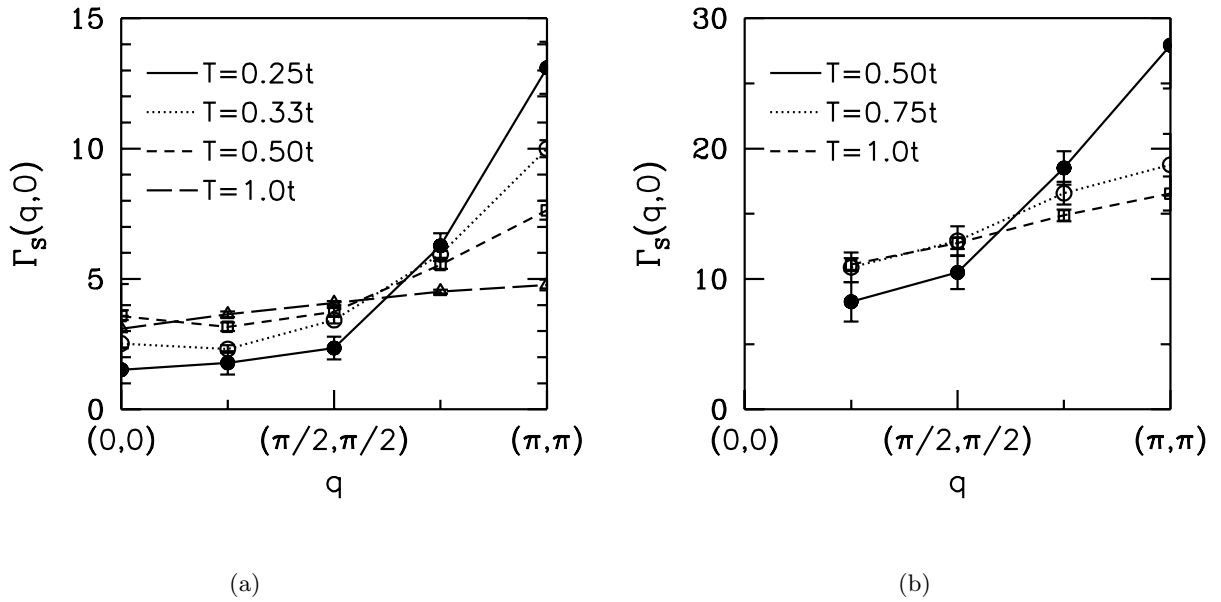


Figure 6.5: Reducible particle-particle scattering vertex in the singlet channel $\Gamma_s(\mathbf{q}, i\omega_m = 0)$ versus $\mathbf{q}$ for (a) $U = 4t$ and (b) $U = 8t$. Here, $\mathbf{q} = \mathbf{p}' - \mathbf{p}$ and $\mathbf{p}$ is kept fixed at $(\pi, 0)$. These results were obtained at $\langle n \rangle = 0.87$ on an $8 \times 8$ lattice. For $U = 8t$, $\Gamma_s(\mathbf{q}, 0)$ at $\mathbf{q} = (0,0)$ is not shown because of large error bars in the data in this case.

$T = 0.33t$ and $U = 8t$, $\Gamma_s(\mathbf{q} = (\pi, \pi), 0)$ was calculated to be $60t \pm 20t$ after long simulation times, while $\Gamma_s(\mathbf{q} = (\pi/4, \pi/4), 0)$ was $10t \pm 10t$.

Next, in Fig. 6.6(a) and (b), the momentum and the Matsubara-frequency dependence of the irreducible particle-particle vertex $\Gamma_{Is}(\mathbf{q}, i\omega_m)$ is shown for $U = 4t$. At $\mathbf{q} = (\pi, \pi)$ momentum transfer, $\Gamma_{Is}(\mathbf{q}, 0)$ reaches values larger than twice the bandwidth. It is useful to compare Figs. 6.6(a) and 6.5(a) in order to understand the effect of the repeated particle-particle scatterings on $\Gamma_{Is}$. At these temperatures, the effect of these scatterings is basically to suppress the momentum and frequency-independent background in $\Gamma_{Is}$. For instance, at $T = 0.25t$ the difference in the magnitude of $\Gamma_{Is}(\mathbf{q}, 0)$ between $\mathbf{q} = (\pi, \pi)$ and $(\pi/4, \pi/4)$ is about $10t$, which is the same as in $\Gamma_s(\mathbf{q}, 0)$. This is similar to the suppression of the screened Coulomb repulsion, which varies more slowly in frequency compared to the phonon propagator, in the usual phonon-mediated pairing. As a $d_{x^2-y^2}$-

Figure 6.6: (a) Momentum and (b) the Matsubara-frequency dependence of the irreducible particle-particle scattering vertex in the singlet channel $\Gamma_{Is}(\mathbf{q}, i\omega_m)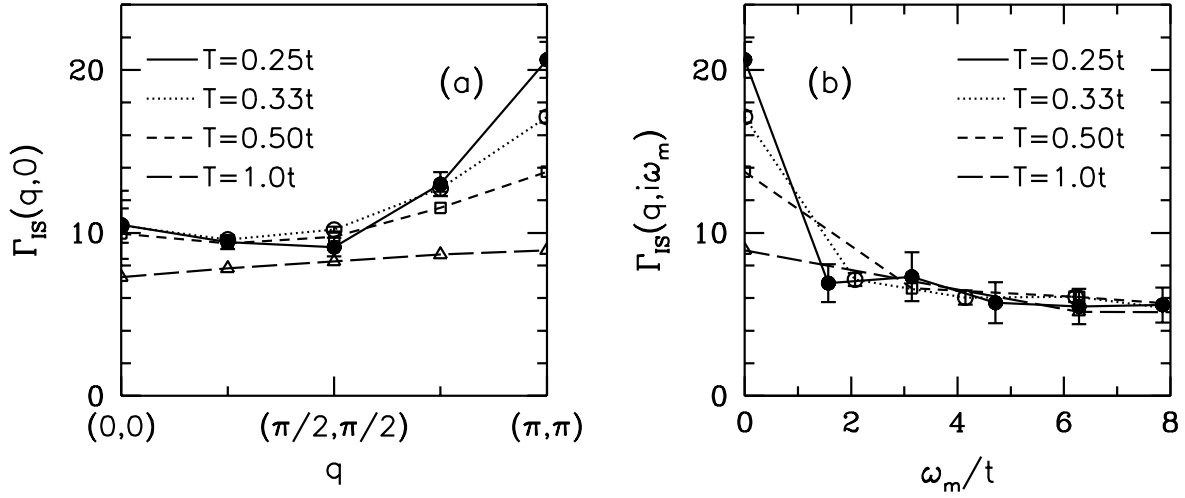$. In (a), $\Gamma_{Is}$ versus $\mathbf{q} = \mathbf{p}' - \mathbf{p}$ is plotted where $\mathbf{p}$ is kept fixed at $(\pi, 0)$. In (b), $\Gamma_{Is}$ versus $\omega_m$ is plotted for $\mathbf{q} = (\pi, \pi)$. Here, $\omega_m = \omega_{n'} - \omega_n$ and $\omega_n$ is kept fixed at $\pi T$. These results are for $U = 4t$ and $\langle n \rangle = 0.87$ on an $8 \times 8$ lattice.

wave superconducting instability is approached, the expected behaviour for an infinite system is that $\Gamma_s(\mathbf{q} = (\pi, \pi), 0) \to +\infty$ while $\Gamma_s(\mathbf{q} = (0, 0), 0) \to -\infty$. These QMC data show that such resonant scattering in the $d_{x^2-y^2}$-wave channel is not taking place at these temperatures.

It is desirable to know how $\Gamma_{Is}$ varies as $U/t$ increases. However, it has not been possible to obtain $\Gamma_{Is}$ for $U = 8t$ from the $t$-matrix equation because of the larger error bars for this case. Nevertheless, in Fig. 6.5(b) it is seen that $\Gamma_s(\mathbf{q}, 0)$ for $U = 8t$ and $T = 0.5t$ exhibits large variation of order $20t$ between points $(\pi/4, \pi/4)$ and $(\pi, \pi)$. If at these temperatures the effect of the $t$-matrix scattering is only to suppress the $\mathbf{q}$ and $\omega_m$ independent background in $\Gamma_{Is}$, then this means that $\Gamma_{Is}$ grows considerably as $U/t$ increases from 4 to 8.

Next, the temperature evolution of $\Gamma_{Is}(\mathbf{q}, i\omega_m)$ for $U = 4t$ is compared with that of the magnetic susceptibility $\chi(\mathbf{q}, i\omega_m)$. Figure 6.7(a) shows Monte Carlo data on $\chi(\mathbf{q}, 0)$ versus $\mathbf{q}$ at the same temperatures as in Fig. 6.6. The Matsubara frequency dependence of $\chi(\mathbf{q} = (\pi, \pi), i\omega_m)$ is shown in Fig. 6.7(b). Comparing Figs. 6.6 and 6.7, one sees that the temperature evolution of $\Gamma_{Is}(\mathbf{q}, i\omega_m)$ closely follows that of $\chi(\mathbf{q}, i\omega_m)$. Both of these quantities peak at $\mathbf{q} = (\pi, \pi)$, and as $\omega_m$ increases $\Gamma_{Is}$ goes to the bare $U$ value while $\chi$ decays to zero. The relation between $\Gamma_{Is}$ and the spin fluctuations will be studied in more detail in Section 6.4, where the QMC results on $\Gamma_{Is}$ will be compared with the single spin-fluctuation exchange interaction.

At this point, it should be noted that the $\mathbf{q}$ dependence of the effective pairing interaction for the cuprates was also studied within the spin-bag approach where a dip at $\mathbf{q} \sim 0$ is found in addition to the peak at $\mathbf{q} \sim (\pi, \pi)$ [Kampf and Schrieffer 1990a]. The dip is due to the cross-exchange of two AF spin fluctuations and it is responsible for the effective attraction between two spin bags. At $T = 0.25t$, which is the lowest temperature where the QMC calculation of $\Gamma_{Is}$ can be carried out, a dip in $\Gamma_{Is}$ at $\mathbf{q} \sim 0$ is not found.

<p style="text-align:center">(a)</p>



<p style="text-align:center">(b)</p>
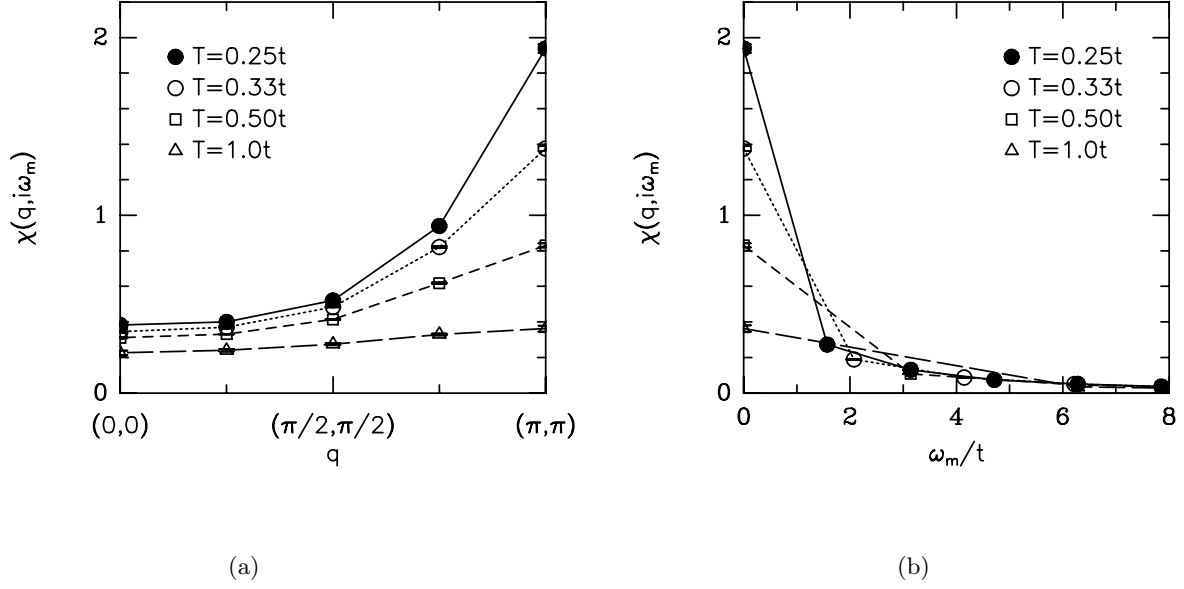
Figure 6.7: (a) Momentum and (b) the Matsubara-frequency dependence of the magnetic suscep-tibility $\chi(\mathbf{q}, i\omega_m)$ at various temperatures. In (a), $\chi(\mathbf{q}, i\omega_m)$ versus $\mathbf{q}$ is plotted for $\omega_m = 0$. In (b), $\chi(\mathbf{q} = (\pi, \pi), i\omega_m)$ versus $\omega_m$ is plotted. These results are for $U = 4t$ and $\langle n \rangle = 0.87$ on an $8 \times 8$ lattice.
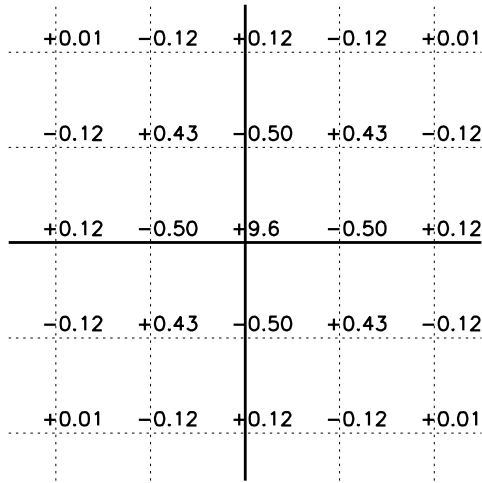


Figure 6.8: Real-space pattern of $\Gamma_{Is}(\mathbf{R})$ for $U = 4t$, $T = 0.25t$ and $\langle n \rangle = 0.87$. Here, it is seen that for $\mathbf{R} = 0$, $\Gamma_{Is}(\mathbf{R})$ is strongly repulsive while being attractive when the singlet electron pair is separated by one lattice spacing.

<p style="text-align:center">37</p>

In order to gain insight into the real-space structure of the effective particle-particle interaction, it is useful to consider the Fourier transform

$$\Gamma_{Is}(\mathbf{R}) = \frac{1}{N^2} \sum_{\mathbf{p},\mathbf{p}'} e^{i(\mathbf{p}-\mathbf{p}')\cdot\mathbf{R}} \Gamma_{Is}(\mathbf{p}', i\omega_{n'}|\mathbf{p}, i\omega_n) \qquad (6.10)$$

for the lowest Matsubara frequencies $\omega_n = \omega_{n'} = \pi T$. Figure 6.8 shows the Monte Carlo data on $\Gamma_{Is}(\mathbf{R})$ as a function of $\mathbf{R}$ for $T = 0.25t$. At $\mathbf{R} = 0$, $\Gamma_{Is}$ is strongly repulsive, as expected, but for a singlet electron pair separated by one lattice spacing, $\Gamma_{Is}$ is attractive. As the pair separation increases further, $\Gamma_{Is}$ oscillates in sign and its magnitude decreases rapidly, reflecting the short-range nature of the interaction. Pairing correlations with the proper space-time structure can avoid the large onsite repulsion while taking advantage of the near-neighbour attraction. Thus, the interaction $\Gamma_{Is}$ is attractive in the $d_{x^2-y^2}$-wave channel.

In Fig. 6.8, it is seen that the effective attractive interaction is $-0.5t$ at the nearest-neighbour site. Here, one might argue that the long-range Coulomb repulsion between the electrons, which is not taken into account in the Hubbard model, could overcome this attraction. However, one would expect the long-range Coulomb repulsion to have weak $\omega_m$ dependence compared to that seen in Fig. 6.6(b), and after the $t$-matrix scatterings it should have weak influence on the strength of the pairing in the $d_{x^2-y^2}$-wave channel.

## 6.3   Bethe-Salpeter equation in the particle-particle channel

In this section, the particle-particle Bethe-Salpeter equation will be solved using the QMC data on the irreducible interaction $\Gamma_I$ and the one-electron Green's function. This way one can determine the magnitude of the eigenvalues and the $(\mathbf{p}, i\omega_n)$ structure of the leading pair-field eigenfunctions. This approach is useful for studying the leading scattering channels in the $t$-matrix quantitatively. For instance, one can determine how close the system is to a Kosterlitz-Thouless superconducting transition, and compare the strength of the pairing in various channels. The particle-particle Bethe-Salpeter equation is

$$\lambda_\alpha \phi_\alpha(p) = -\frac{T}{N} \sum_{p'} \Gamma_I(p|p')G_\uparrow(p')G_\downarrow(-p')\phi_\alpha(p'), \qquad (6.11)$$

where $\phi_\alpha(p)$ is the pair-field eigenfunction and $\lambda_\alpha$ is the corresponding eigenvalue. The Feynman diagram representing Eq. (6.11) is shown in Fig. 6.9. When the leading eigenvalue reaches one, the superconducting transition takes place, and the Bethe-Salpeter equation for the corresponding eigenfunction becomes equivalent to the superconducting gap equation.
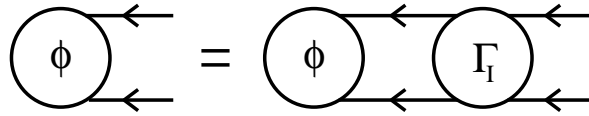


Figure 6.9:   Feynman diagram representing the Bethe-Salpeter equation.

Here, data from Refs. [Bulut *et al.* 1993] will be shown. Both the triplet and the singlet solutions of the Bethe-Salpeter equation will be considered. The momentum and the Matsubara-frequency structures of the leading eigenfunctions will be presented. In addition to the singlet $d_{x^2-y^2}$-wave eigenfunction $\phi_d(\mathbf{p}, i\omega)$, solutions which are odd in $\omega_n$ and have $s$ and $p$-wave symmetries are found. The odd-frequency eigenfunctions with $s$-wave and $p$-wave symmetries correspond to triplet

and singlet solutions, respectively. The finite-size scaling of the eigenvalues indicates that as $T$ is lowered the singlet $d_{x^2-y^2}$-wave eigenvalue grows fastest, and at low $T$ the dominant singlet pairing channel has the $d_{x^2-y^2}$-wave symmetry. In these calculations, the even-frequency extended $s$-wave channel was not found to be one of the leading pairing channels.

The case of the odd-frequency pairing channel is interesting. The possibility of pairing in the triplet odd-frequency $s$-wave channel was first studied within the context of ${}^3$He in Ref. [Berezinskii 1974]. The singlet odd-frequency $p$-wave channel was studied initially by using an effective interaction which is mediated by phonons [Balatsky and Abrahams 1992]. The possibility that an effective attraction in the singlet odd-frequency $p$-wave channel could be generated by the spin fluctuations was noted in Ref. [Abrahams et al. 1993] at about the same time the QMC calculations reviewed here were carried out. The general properties of the odd-frequency superconductors were discussed in Ref. [Abrahams et al. 1995].

In addition, here the effects of increasing $U/t$ on the leading pairing channels will be discussed. As seen in the previous section, it was not possible to calculate $\Gamma_{Is}$ for $U = 8t$. However, if $\Gamma$ is used rather than $\Gamma_I$ in Eq. (6.11), then the corresponding eigenvalues are given by $\lambda_\alpha/(1 - \lambda_\alpha)$, where $\lambda_\alpha$ are the eigenvalues for the irreducible vertex. Hence, through this indirect way it is possible to study the leading Bethe-Salpeter eigenvalues for $U = 8t$. It will be shown that as $U/t$ increases from 4 to 8, the leading eigenvalues grow, since the effective particle-particle interaction gets stronger, but the momentum and the frequency structure of their eigenfunctions does not exhibit qualitative changes.

In general, the Bethe-Salpeter equation can have both singlet and triplet solutions corresponding to a pair-wave function that has overall even or odd parity when $p = (\mathbf{p}, i\omega_n)$ goes to $(-\mathbf{p}, -i\omega_n)$. Here, the pair wave functions are characterized by its symmetry in momentum and spin space. The usual singlet $s$ and $d_{x^2-y^2}$-wave states are even in frequency and even in momentum, $\phi(\mathbf{p}, -i\omega_n) = \phi(\mathbf{p}, i\omega_n)$ and $\phi(-\mathbf{p}, i\omega_n) = \phi(\mathbf{p}, i\omega_n)$, while the usual triplet $p_x$ or $(p_y)$ state is even in frequency and odd when $p_x$ goes to $-p_x$. There are also odd-frequency pair-wave functions. In this case, one can have an odd-frequency $s$-wave triplet for which $\phi(\mathbf{p}, -i\omega_n) = -\phi(\mathbf{p}, i\omega_n)$ and $\phi(-\mathbf{p}, i\omega_n) = \phi(\mathbf{p}, i\omega_n)$, or an odd-frequency $p_x$ (or $p_y$)-wave singlet with $\phi(\mathbf{p}, -i\omega_n) = -\phi(\mathbf{p}, i\omega_n)$ and $\phi(-\mathbf{p}, i\omega_n) = -\phi(\mathbf{p}, i\omega_n)$. In the regime of the Hubbard model that is being studied, the $s$-wave triplet, and the $p$ and $d_{x^2-y^2}$-wave singlet solutions are dominant.

The temperature evolution of the four largest eigenvalues for $U = 4t$ and $\langle n \rangle = 0.87$ are given in Table 1. The momentum and the frequency dependence of the corresponding pair-wave functions are shown in Figs. 6.10 and 6.11 for $T = 0.5t$. At this temperature, an $s$-wave triplet state has the largest eigenvalue $\lambda_s \approx 0.23$. As seen in Figs. 6.10(a) and 6.11(a) (solid circles), the pair-wave function $\phi_s(\mathbf{p}, i\omega_n)$ of the $s$-wave triplet state is even in $\mathbf{p}$ and odd in $\omega_n$. The open circles in Figs. 6.10(a) and 6.11(a) represent the pair-wave function $\phi_{s'}(\mathbf{p}, i\omega_n)$ which has the second largest eigenvalue. This is also an odd-frequency $s$-wave triplet state. The $d_{x^2-y^2}$-wave singlet state shown as the solid circles in Figs. 6.10(b) and 6.11(b) has the third largest eigenvalue. The fourth largest eigenvalue corresponds to a state which is odd in both $\omega_n$ and $\mathbf{p}$, having $p_y$ (or $p_x$) symmetry [open circles in Figs. 6.10(b) and 6.11(b)], hence it is also a singlet.

As $T$ is lowered from $1.0t$ down to $0.25t$, the largest eigenvalue $\lambda_s$ stays nearly the same, while $\lambda_d$ increases by about a factor of seven. This can be understood in terms of the temperature dependence of $\Gamma_I(p'|p)$ which enters the Bethe-Salpeter equation. The pair-wave functions which are smooth in $\mathbf{p}$ but odd in $\omega_n$ make optimum use of the $(\omega_n, \omega_{n'})$ frequency structure of the repulsive $\Gamma_I(p'|p)$ for pairing. However, as the temperature is lowered and $\Gamma_I(p'|p)$ for $\mathbf{p}' - \mathbf{p} = (\pi, \pi)$ grows, the $d_{x^2-y^2}$ and $p$-wave solutions can make better use of the momentum structure in $\Gamma_I$, and their eigenvalues get enhanced.
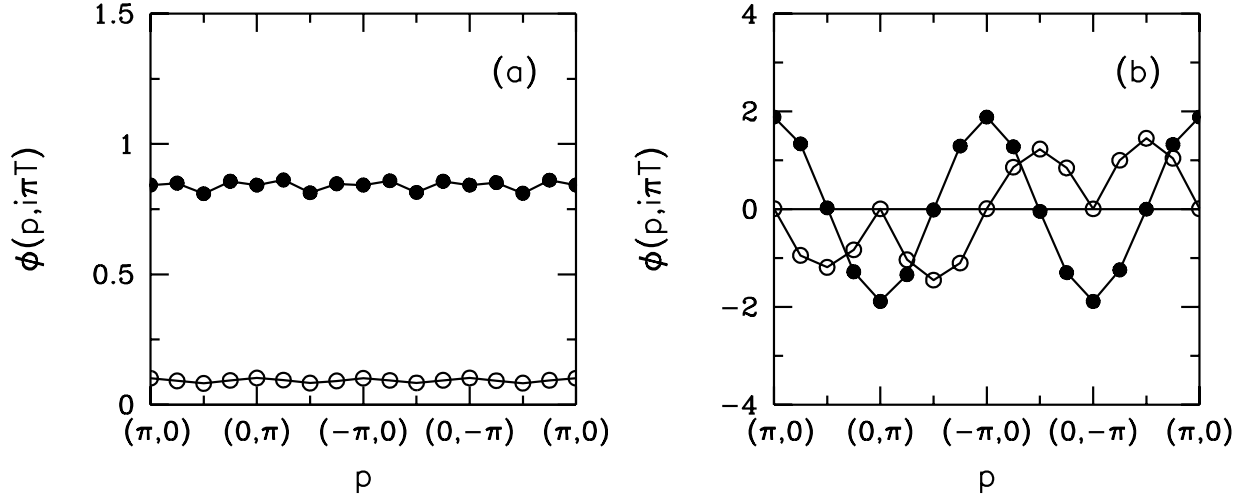
Figure 6.10: Momentum dependence of the leading Bethe-Salpeter eigenfunctions $\phi_\alpha(\mathbf{p}, i\omega_n)$. These results are for $\omega_n = \pi T$, $U = 4t$, $T = 0.5t$ and $\langle n \rangle = 0.87$ on an $8 \times 8$ lattice. In (a), two odd-frequency $s$-wave eigenfunctions are plotted, and in (b) the $d_{x^2-y^2}$-wave (filled circles) and $p_y$-wave (open circles) are plotted.
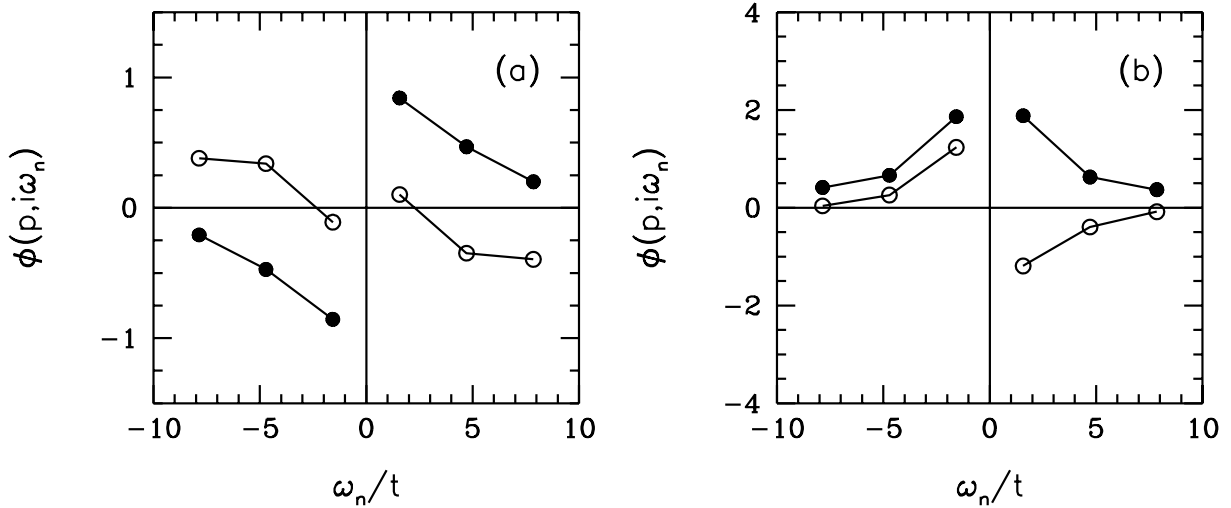


Figure 6.11: Matsubara frequency dependence of the leading Bethe-Salpeter eigenfunctions $\phi_\alpha(\mathbf{p}, i\omega_n)$. These results are for $U = 4t$, $T = 0.5t$ and $\langle n \rangle = 0.87$ on an $8 \times 8$ lattice. In (a), $\phi(\mathbf{p} = (\pi, 0), i\omega_n)$ is shown for the odd-$\omega_n$ $s$ and $s'$ channels. In (b), $\phi(\mathbf{p}, i\omega_n)$ is shown for the singlet $d_{x^2-y^2}$-wave channel at $\mathbf{p} = (\pi, 0)$ and for the singlet $p_y$-wave channel at $\mathbf{p} = (\pi/2, \pi/2)$.

| $T/t$ | $\lambda_s$ | $\lambda_{s'}$ | $\lambda_p$ | $\lambda_d$ |
|---|---|---|---|---|
| 1.0 | 0.261 | 0.037 | 0.023 | 0.022 |
| 0.50 | 0.228 | 0.090 | 0.066 | 0.076 |
| 0.33 | 0.251 | 0.104 | 0.095 | 0.130 |
| 0.25 | $0.264 \pm 0.007$ | $0.124 \pm 0.006$ | $0.129 \pm 0.007$ | $0.182 \pm 0.006$ |

Table 1: Temperature dependence of the Bethe-Salpeter eigenvalues for $U = 4t$ and $\langle n \rangle = 0.87$ on an $8 \times 8$ lattice. The error bars represent the uncertainty due to the Monte Carlo sampling. The error bars were not calculated at all temperatures, since it requires considerably more computer time. When the error bars are not indicated, they are estimated to be less than 10%.

| $L \times L$ | $\lambda_s$ | $\lambda_p$ | $\lambda_d$ |
|---|---|---|---|
| $4 \times 4$ | $0.296 \pm 0.010$ | $0.204 \pm 0.014$ | $0.184 \pm 0.016$ |
| $8 \times 8$ | $0.264 \pm 0.007$ | $0.129 \pm 0.007$ | $0.182 \pm 0.006$ |

Table 2: Finite-size dependence of the Bethe-Salpeter eigenvalues for $T = 0.25t$, $U = 4t$ and $\langle n \rangle = 0.87$.
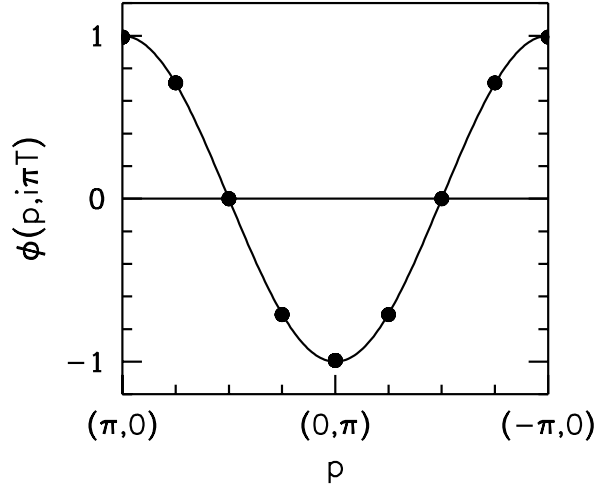


Figure 6.12: Comparison of the $d_{x^2-y^2}$-wave eigenfunction $\phi_d(\mathbf{p}, i\pi T)$ with the usual $d_{x^2-y^2}$-wave form $\Delta_{\mathbf{p}} = (\Delta_0/2)(\cos p_x + \cos p_y)$ for $U = 4t$, $T = 0.25t$ and $\langle n \rangle = 0.87$. Here, both $\phi_d(\mathbf{p}, i\pi T)$ and $\Delta_{\mathbf{p}}$ have been normalised to 1 at $\mathbf{p} = (\pi, 0)$.

Table 2 shows the finite-size effects on the leading eigenvalues at $T = 0.25t$. Here, it is seen that the finite-size effects are especially large for the $p$-wave channel, and $\lambda_p$ decreases as the system size grows from $4 \times 4$ to $8 \times 8$. The finite size effects for the $d_{x^2-y^2}$-wave case are small. Hence, these results show that as $T$ is lowered, $\lambda_d$ grows fastest and at low $T$ the dominant singlet pairing channel has the $d_{x^2-y^2}$-wave symmetry.

It is useful to compare the momentum dependence of the $d_{x^2-y^2}$-wave eigenvalue $\phi_d(\mathbf{p}, i\omega_n)$ at $\omega_n = \pi T$ with the usual $d_{x^2-y^2}$-wave gap form $\Delta_{\mathbf{p}} = (\Delta_0/2)(\cos p_x - \cos p_y)$, since this is often used in modelling the superconducting state of the cuprates. Figure 6.12 shows that the QMC data on
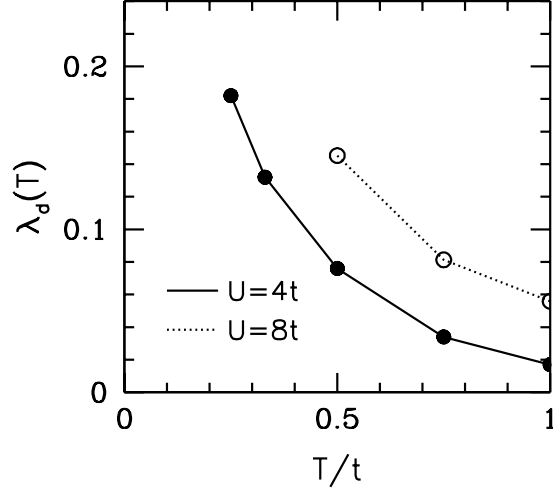
Figure 6.13: Temperature dependence of the $d_{x^2-y^2}$-wave eigenvalue $\lambda_d$ for $U = 4t$ and $8t$ at $\langle n \rangle = 0.87$.

$\phi_d(\mathbf{p}, i\pi T)$ taken at $T = 0.25t$ follow the usual $d_{x^2-y^2}$-wave form closely.

Finally, the filled circles in Fig. 6.13 show the growth of $\lambda_d$ for $U = 4t$ as the temperature is lowered, while the open circles represent $\lambda_d$ for $U = 8t$. The results on $\lambda_d$ for $U = 8t$ were obtained as described above. Here, it is seen that $\lambda_d$ increases with $U/t$.

At the lowest temperature where $\lambda_d$ can be calculated, the system is far from a Kosterlitz-Thouless superconducting transition which would be signalled by $\lambda_d \to 1$. Hence, while these data imply that at the temperatures where the QMC simulations are carried out, the singlet $d_{x^2-y^2}$-wave pairing correlations are becoming dominant, it is not known whether $\lambda_d \to 1$ at lower temperatures. Below in Section 8.1, these results on $\lambda_d$ will be compared with the results of the FLEX calculations.

The QMC calculation of $\lambda_d$ for the doped case cannot be carried out at any lower temperatures. However, for half-filling it is possible to calculate the various pairing eigenvalues at low $T$ and compare them with the eigenvalues of the Bethe-Salpeter equation in the AF particle-hole channel, $\overline{\lambda}_\alpha$. The leading magnetic eigenvalue $\overline{\lambda}_1$ occurs in an even-frequency $s$-wave channel with center-of-mass momentum $\mathbf{Q} = (\pi, \pi)$. In Fig. 6.14, $\overline{\lambda}_1$ is compared with the various pairing eigenvalues for $U = 4t$ and $8t$ at half-filling. As expected, at low temperatures $\overline{\lambda}_1$ reaches 1 asymptotically, signalling the phase transition to the AF order state on the $8 \times 8$ lattice. Here, it is also seen that as the AF correlations develop at half-filling, $\lambda_d$ becomes the leading pairing eigenvalue while always staying smaller than the magnetic eigenvalue $\overline{\lambda}_1$.

## 6.4   Comparison with the spin-fluctuation exchange approximation

Various spin-fluctuation exchange theories have been used for studying $d_{x^2-y^2}$-wave pairing for the cuprates [Bickers *et al.* 1987 and 1989, Moriya *et al.* 1990, Monthoux *et al.* 1991]. In this context, it is of interest to see to what extent the Monte Carlo results for the irreducible vertex can be modelled by a single spin-fluctuation exchange interaction. For this purpose, here we compare the
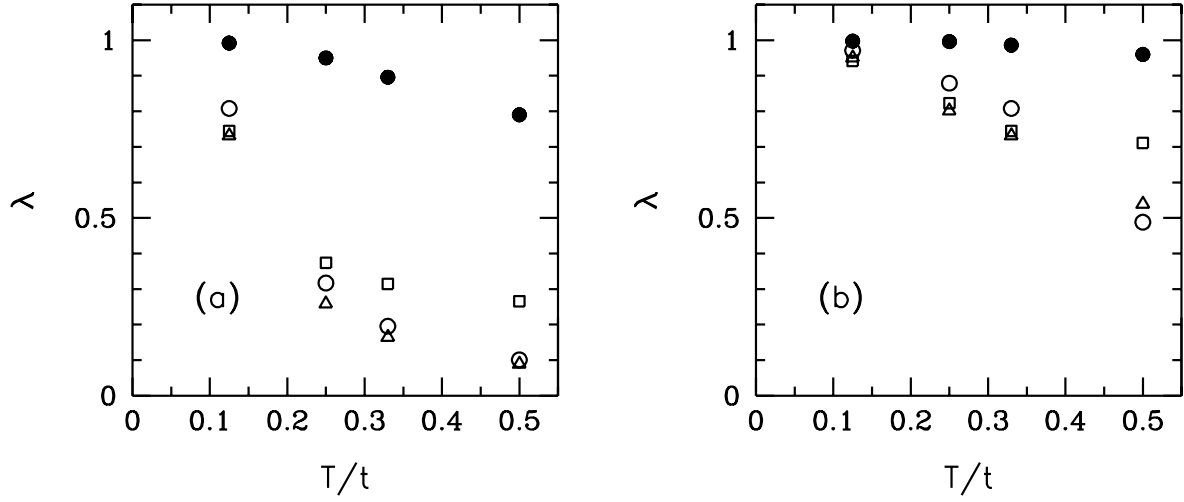
Figure 6.14: Eigenvalues of the particle-hole and the particle-particle Bethe-Salpeter equations versus $T$ for (a) $U = 4t$ and (b) $U = 8t$ for an $8 \times 8$ half-filled lattice. The solid points ($\bullet$) are for the leading eigenvalue $\overline{\lambda}_1$ of the Bethe-Salpeter equation in the AF particle-hole channel with the center-of-mass momentum $\mathbf{Q} = (\pi, \pi)$. The open symbols denote the even-frequency $d_{x^2-y^2}$-wave ($\circ$), and the odd-frequency $p$ ($\triangle$) and $s$-wave ($\square$) eigenvalues of the particle-particle Bethe-Salpeter equation.

Monte Carlo data with the approximate form

$$\Gamma_I^{SF}(\mathbf{q}, i\omega_m) = U + \frac{3}{2} g^2 U^2 \chi(\mathbf{q}, i\omega_m). \tag{6.12}$$

This form is motivated by the single spin-fluctuation exchange interaction [Berk and Schrieffer 1966, Doniach and Engelsberg 1966], which basically has this form with $g = 1$ near the antiferromagnetic instability. The Feynman diagrams illustrating the single spin-fluctuation exchange interaction were shown in Fig. 2.1. The factor of $3/2$ arises from the two transverse and one longitudinal spin fluctuations. In calculating $\Gamma_{Is}^{SF}$ with Eq. (6.12), we will use Monte Carlo results for $\chi(\mathbf{q}, i\omega_m)$ and also set $g = 0.8$. The corresponding value of $3.2t$ for the effective coupling $gU$ is consistent with the results of the Monte Carlo calculations of the effective irreducible vertex in the particle-hole channel, $\overline{U}(\mathbf{q}, 0)$, which were discussed in Section 3.4. Formally, Eq. (6.12) is analogous to the effective interaction in the electron-phonon superconductor

$$V(\mathbf{q}, i\omega_m) = U + \sum_{\lambda} |g_{\mathbf{q}\lambda}|^2 D_{\lambda}(\mathbf{q}, i\omega_m), \tag{6.13}$$

where $D_{\lambda}(\mathbf{q}, i\omega_m)$ is the dressed phonon propagator and $|g_{\mathbf{q}\lambda}|^2$ is the renormalised electron-phonon coupling.

Figure 6.15(a) shows the single spin-fluctuation interaction in the singlet channel $\Gamma_{Is}^{SF}(\mathbf{q}, i\omega_m)$ versus $\mathbf{q}$ at various temperatures. These results compare well with $\Gamma_{Is}(\mathbf{q}, i\omega_m = 0)$ seen in Fig. 6.6(a). Likewise, the comparison of Fig. 6.15(b) with Fig. 6.6(b) shows that the frequency

43
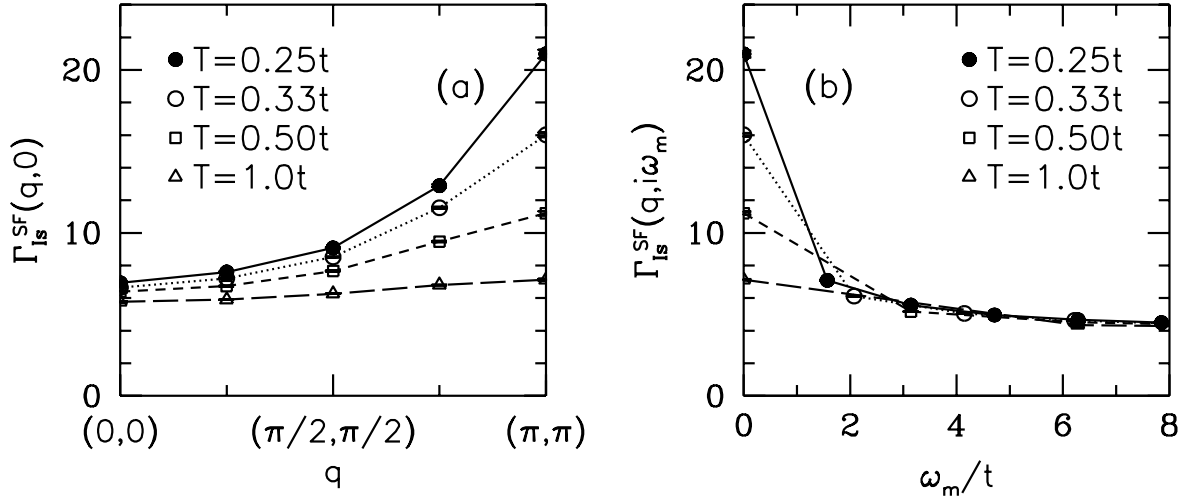
Figure 6.15: Single-spin-fluctuation exchange approximation for the irreducible particle-particle scattering vertex in the singlet channel $\Gamma_{Is}(\mathbf{q}, i\omega_m)$. In (a), $\Gamma_{Is}$ versus $\mathbf{q}$ is plotted. In (b), $\Gamma_{Is}$ versus $\omega_m$ is plotted for $\mathbf{q} = (\pi, \pi)$. These results have been obtained for $U = 4t$ and $\langle n \rangle = 0.87$ using the Monte Carlo data on $\chi(\mathbf{q}, i\omega_m)$.

dependence of $\Gamma_{Is}^{SF}$ is in agreement with the Monte Carlo data. Considering the simplicity of Eq. (6.12), this agreement with the Monte Carlo data is quite good. These comparisons suggest that a properly renormalized single-spin-fluctuation exchange interaction is capable of reproducing the basic features of the effective particle-particle interaction in the weak-to-intermediate coupling Hubbard model at temperatures greater or of order $J/2$.

## 6.5 Comparison with the perturbation theory

In this section, the perturbation theory results for $\Gamma_{Is}$ through third order in $U$ from Ref. [Bulut *et al.* 1995] will be shown. These provide insight into the various subprocesses contributing to $\Gamma_{Is}$. Figure 6.16 shows the diagrams contributing to $\Gamma_{Is}$ up to third order in $U$. The dashed line in this figure represents the bare Coulomb repulsion. The diagrams (a) and (h) represent the first two terms in an RPA series corresponding to the exchange of a longitudinal spin fluctuation. Similarly, the low-order contributions arising from the exchange of a transverse spin fluctuation are represented by the diagrams (b) and (e). The diagrams (c) and (d) can be considered as corrections to diagram (b), where the bare particle-hole irreducible vertex is renormalized through Kanamori type of particle-particle scatterings [Kanamori 1963]. The diagrams (f) and (g) represent vertex corrections to the bare interaction (a).

These diagrams have been evaluated on an $8 \times 8$ lattice with $U = 4t$, and the results of the various contributions are shown as a function of $\mathbf{q}$ for $\omega_m = 0$ in Fig. 6.17(a). The frequency dependence for $\mathbf{q} = (\pi, \pi)$ is shown similarly in Fig. 6.17(b). Here, the results on $\Gamma_{Is}$ are plotted in the same way as in the previous section. In these figures, the filled circles represent the diagrams (a) and (h) in Fig. 6.16, and the open circles are for the diagrams (b) and (e). The triangles and the
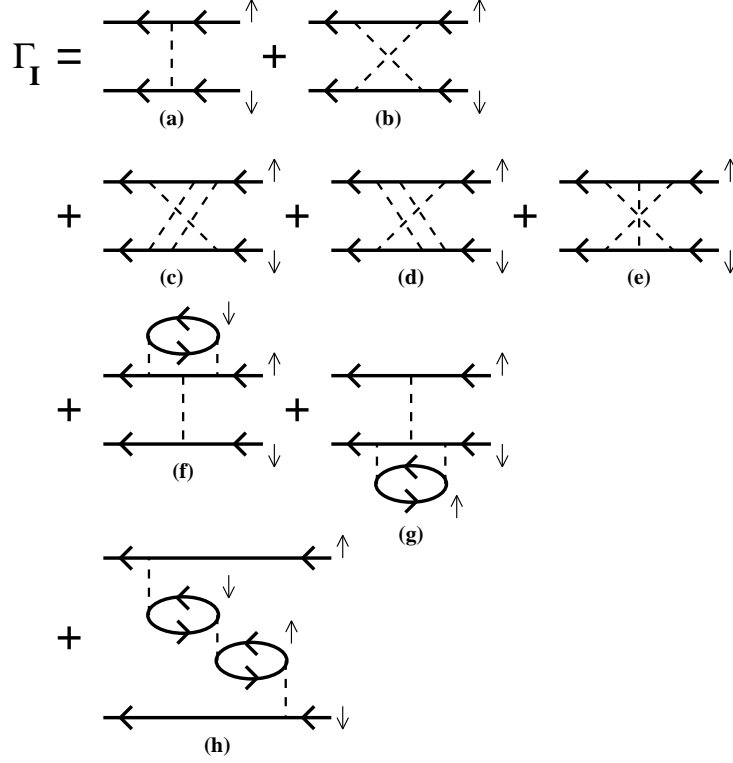
Figure 6.16: Feynman diagrams contributing to the irreducible particle-particle interaction through third order in $U$.

squares in Figs. 6.17(a) and (b) represent the contributions of the (c)-(d) and (f)-(g), respectively. The dominant contributions arise from the leading contributions to the spin-fluctuation exchange processes (a), (b), (e) and (h), and they give contributions which peak at $\mathbf{q} = (\pi, \pi)$. For $\omega_m = 0$, both the Kanamori renormalization graphs and the vertex corrections act to reduce the strength of the $\mathbf{q} = (\pi, \pi)$ interaction by about one-third. In Fig. 6.18, the results obtained by summing the diagrams shown in Fig. 6.16 are compared with the Monte Carlo results for $T = 0.25t$. At this temperature, the low-order graphs in Fig. 6.16 are not adequate to represent the large momentum behaviour of the effective interaction.

The importance of the vertex corrections to the single spin-fluctuation exchange interaction was pointed out in Ref. [Schrieffer 1995]. In particular, it was noted that for large values of the ratio $\chi(\mathbf{q} = (\pi, \pi), 0)/\chi(\mathbf{q} \to 0, 0)$, the vertex corrections should suppress the spin-fluctuation exchange interaction at $\mathbf{q} = (\pi, \pi)$ momentum transfer. The diagrams (f) and (g) in Fig. 6.16 are the lowest order vertex corrections, and, indeed, at this level they act to suppress the $\mathbf{q} = (\pi, \pi)$ component of $\Gamma_{Is}$ as seen in Fig. 6.17. However, the QMC data indicates that the suppression of the peak at $\mathbf{q} = (\pi, \pi)$ in $\Gamma_{Is}$ is partial. This is because the ratio $\chi(\mathbf{q} = (\pi, \pi), 0)/\chi(\mathbf{q} \to 0, 0)$ is about 5 rather than being of order 100 at the lowest temperature $\Gamma_{Is}$ was calculated with QMC. Hence, a large AF correlation length is not necessary, and simply weight in $\Gamma_{Is}$ at large momentum transfers is sufficient to yield a sizeable attractive interaction in the $d_{x^2-y^2}$-wave channel.

The results reviewed in this section constitute what has been learned about $d_{x^2-y^2}$-wave pairing in the 2D Hubbard model from the determinantal QMC simulations. These simulations are not carried out at lower temperatures because of the sign problem, and, hence, it is not possible to know whether superconducting long-range order develops at lower $T$ [Loh *et al.* 1990]. In Fig. 6.19(a),

(a)                    (b)
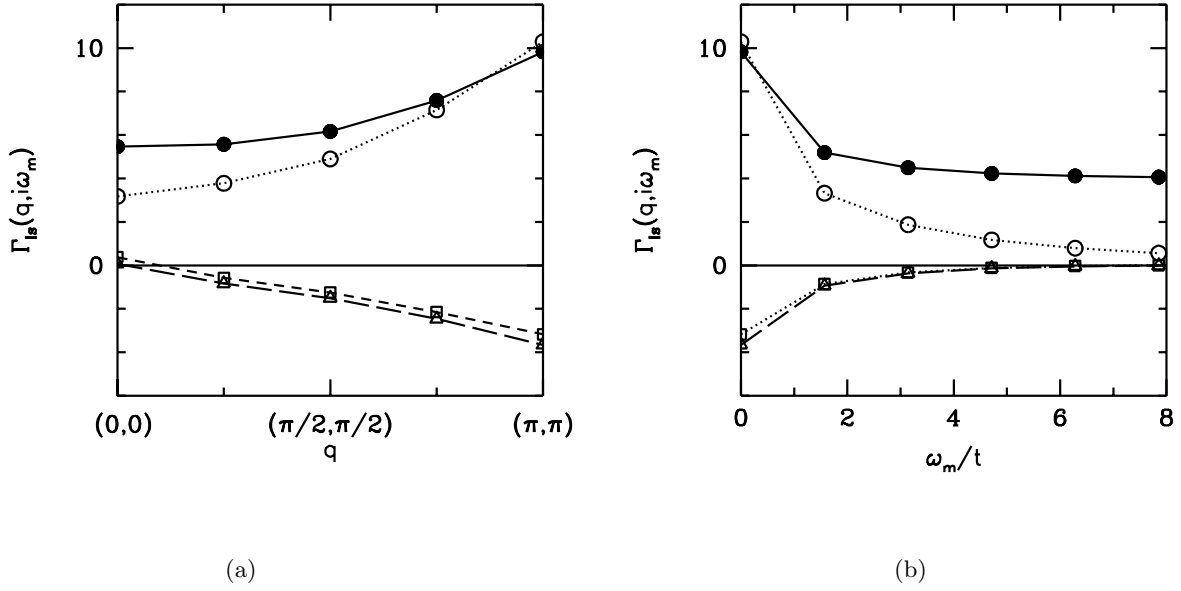
Figure 6.17: Various diagrams contributing to the irreducible particle-particle interaction $\Gamma_{Is}(\mathbf{q}, i\omega_m)$ through third order in $U$. In (a) the momentum dependence is shown for $\omega_m = 0$, and in (b) the frequency dependence is shown for $\mathbf{q} = (\pi, \pi)$. Here, the filled circles represent the contribution of the bare $U$ and the longitudinal spin-fluctuation exchange (diagrams of type (a) and (h) in Fig. 6.16), the open circles represent the contribution of the transverse spin fluctuations (Fig. 6.16(b) and (e)), the open squares show the ordinary vertex corrections (Fig. 6.16(f) and (g)), and the open triangles show the Kanamori type of vertex corrections (Fig. 6.16(c) and (d)).

the average sign of the fermion determinants, $\langle \text{sign} \rangle$, which is defined in the Appendix, is plotted as a function of $T$ at $\langle n \rangle = 0.87$ for $U = 8t$ and $4t$. As the value of $\langle \text{sign} \rangle$ decreases below 1, the statistical error in the QMC data grows rapidly requiring exponentially long simulation times. In Fig. 6.19(b), the filling dependence of $\langle \text{sign} \rangle$ is shown for $U = 8t$ at $T = 0.5t$ and $0.33t$. These figures show the boundary of the parameter regime of the Hubbard model which cannot be probed because of the sign problem. However, the DMRG calculations [White 1992] are carried out at zero temperature, and they have provided valuable information about this regime in the 2-leg Hubbard ladder. The DMRG studies of the 2-leg Hubbard ladder will be reviewed in the next section.

# 7   2-leg Hubbard ladder

The 2-leg Hubbard ladder has been studied using various many-body techniques such as the DMRG [Noack *et al.* 1994, 1995, 1996 and 1997], the QMC [Dahm and Scalapino 1997], the exact diagonalization [Yamaji and Shimoi 1994], and the weak-coupling renormalization group [Balents and Fisher 1996]. The results of the DMRG and the QMC calculations will be reviewed here.

At half-filling, the ground state of this system does not have AF long-range order, rather it has a spin gap. Near half-filling, this model exhibits short-range AF correlations and power-law decaying $d_{x^2-y^2}$-like superconducting and "$4\mathbf{k}_F$" CDW correlations [Noack *et al.* 1994 and 1996]. The
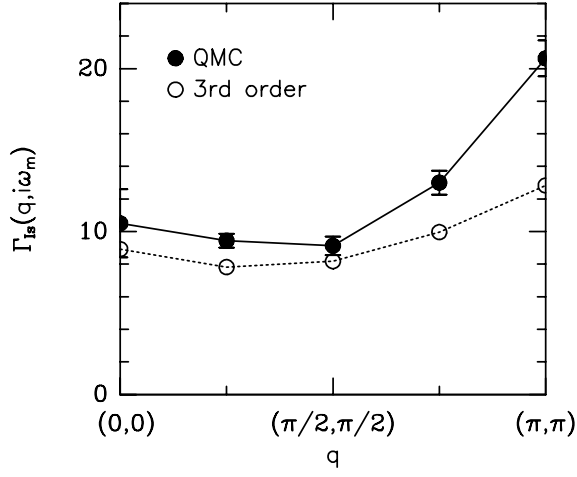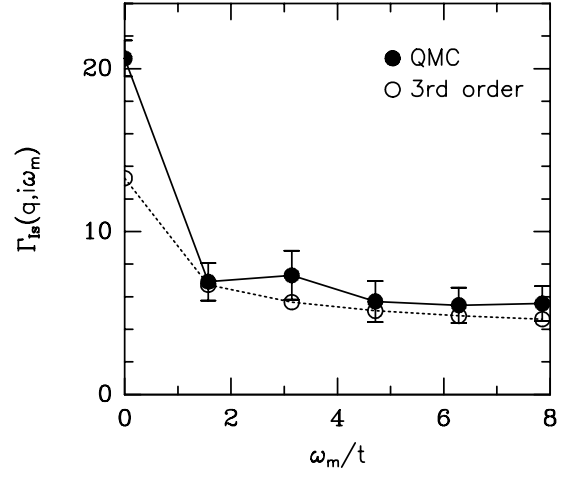
(a)                                                              (b)

Figure 6.18: Comparison of the perturbation theory results on $\Gamma_{Is}(\mathbf{q}, i\omega_m)$ through third order in $U$ with the QMC data. In (a) the momentum dependence is shown for $\omega_m = 0$, and in (b) the frequency dependence is shown for $\mathbf{q} = (\pi, \pi)$.
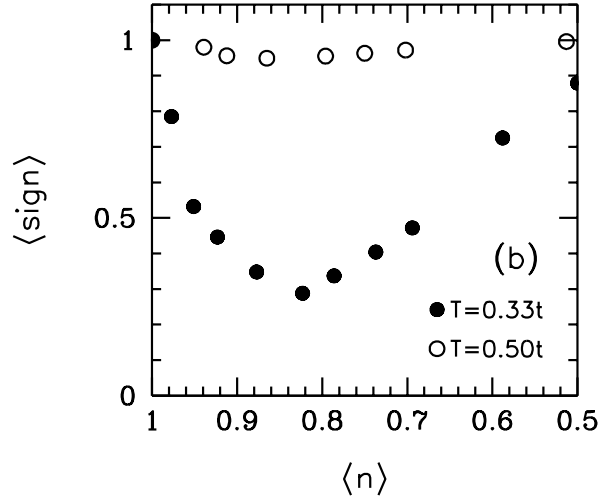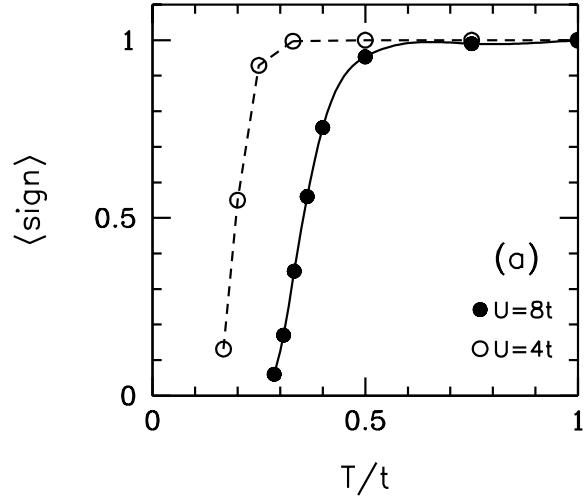


Figure 6.19: (a) Temperature and (b) the filling dependence of $\langle \text{sign} \rangle$. In (a), the results are shown for $U = 8t$ and $4t$ at $\langle n \rangle = 0.87$, and in (b) for $U = 8t$.

DMRG calculations have found that in the ground state of this system the pair-field correlations for the interacting system can get enhanced with respect to those of the noninteracting ($U = 0$) system for a range of the model parameters. This is the first time ever in an exact ground state calculation for a bulk system that by turning on an onsite Coulomb repulsion the superconducting correlations get enhanced. For this reason, the 2-leg Hubbard model is quite important.

Another reason for studying this model is that here it is possible to understand the mechanism mediating the $d_{x^2-y^2}$-like superconducting correlations by comparing the DMRG results with the QMC data obtained at relatively low temperatures. These comparisons indicate that it is the short-range AF fluctuations which mediate the pairing. Furthermore, the pairing is strongest when the model parameters are such that there is enhanced single-particle spectral weight near the $(\pi, 0)$ and the $(0, \pi)$ points of the Brillouin zone. For $U = 8t$ and $\langle n \rangle = 0.875$, this occurs when $t_\perp/t \sim 1.5$. In this case, the irreducible particle-particle vertex peaks at momentum transfers near $(\pi, \pi)$ creating optimum conditions for $d_{x^2-y^2}$ pairing.

It is also interesting to study the 2-leg Hubbard ladder because the half-filled insulating state is spin gapped while in the 2D case there is long-range AF order. In the cuprates, on the other hand, the undoped system has long-range AF order, and a spin gapped phase lies between the superconducting and the insulating phases. The 2-leg Hubbard model is a system where the relation between the spin gap and the superconducting correlations as well as the density correlations can be studied exactly.

In section 7.1 below, the DMRG results on the pair-field correlation function from Ref. [Noack *et al.* 1997] will be shown for various values of the model parameters. In order to understand these results better, in Section 7.2 the QMC results on the single-particle spectral weight from Ref. [Noack *et al.* 1997], the irreducible particle-particle interaction and the solution of the Bethe-Salpeter equation from Ref. [Dahm and Scalapino 1997] will be presented. In Section 7.3, the results on the 2-leg Hubbard ladder will be compared with those on the 2D case. Later, in Section 8.5.3, comparisons will be made with the superconducting correlations found in the 2-leg *t-J* ladder.

## 7.1   DMRG results

The DMRG calculations found that there are power-law decaying $d_{x^2-y^2}$-wave pair-field correlations in the ground state of the 2-leg Hubbard ladder. The $d_{x^2-y^2}$-like internal structure of the pairs can be seen by considering the pair-creation amplitude

$$\langle N_2|(c_{\mathbf{r}\uparrow}^\dagger c_{\mathbf{r'}\downarrow}^\dagger - c_{\mathbf{r}\downarrow}^\dagger c_{\mathbf{r'}\uparrow}^\dagger)|N_1\rangle \tag{7.1}$$

for adding a singlet pair on near-neighbor sites along and across the legs. Here, $|N_1\rangle$ is the ground state with four holes relative to the half-filled band and $|N_2\rangle$ is the ground state with two holes on a $2 \times 16$ ladder. The results on the pair amplitude are shown in Fig. 7.1 for $U/t = 8$ and $t_\perp/t = 1.5$. Note the $d_{x^2-y^2}$-like change in the sign of this matrix element.

Using the DMRG method it is possible to calculate the rung-rung correlation function

$$D(i, j) = \langle \Delta(i)\Delta^\dagger(j)\rangle \tag{7.2}$$

in the ground state of the 2-leg Hubbard ladder with the open boundary conditions. Here,

$$\Delta^\dagger(i) = c_{i1\uparrow}^\dagger c_{i2\downarrow}^\dagger - c_{i1\downarrow}^\dagger c_{i2\uparrow}^\dagger \tag{7.3}$$

creates a singlet pair across the $i$'th rung, and $c_{ik\sigma}^\dagger$ is the electron creation operator with spin $\sigma$ at the $i$'th site of the $k$'th leg of the 2-leg ladder. The fact that the matrix elements shown
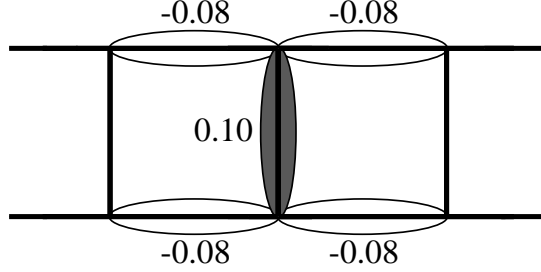
Figure 7.1: Schematic drawing of the pair-wave function showing the values of the off-diagonal matrix element $\langle N_2|(c^\dagger_{\mathbf{r}\uparrow}c^\dagger_{\mathbf{r}'\downarrow} - c^\dagger_{\mathbf{r}\downarrow}c^\dagger_{\mathbf{r}'\uparrow})|N_1\rangle$ for creating a singlet pair between near-neighbor sites. Here, it is seen that the matrix element for this process is negative when the singlet-pair is created along a chain, while it is positive across a rung. This shows the $d_{x^2-y^2}$-like nature of the pairing correlations in the 2-leg Hubbard ladder.

in Fig. 7.1 are finite means that this bare pair-creation operator, which is composed of the bare electron-creation operators $c^\dagger_{ik\sigma}$, has finite overlap with the true pair-creation eigen-operator for this system. In order to minimize the effects of the boundaries, here $D(i, j)$ is averaged over six $(i, j)$ pairs with $\ell = |i - j|$ fixed. This averaging starts with symmetrically placed $(i, j)$ values and then proceeds to shift these to the left and right of the center. By comparing results obtained on different size lattices, it is possible to control the finite size effects. In the following, $D(\ell)$ calculated on the $2 \times 32$ lattice for $\ell < 20$ will be shown. In this case, the finite size effects are negligible.

Figure 7.2 shows $D(\ell)$ versus $\ell$ for various values of $t_\perp/t$ with $U = 8t$ and $\langle n \rangle = 0.875$. The dashed and the dotted lines represent power-law decays of $\ell^{-2}$ and $\ell^{-1}$, respectively. In this figure, it is seen that $D(\ell)$ exhibits a power-law decay for $t_\perp/t < 1.6$. For $t_\perp/t = 1.0$, $D(\ell)$ decays as $\ell^{-2}$. When $t_\perp/t$ is increased from 1.0 to 1.4, the strength of $D(\ell)$ gets enhanced and it decays more slowly. For $t_\perp/t = 1.6$, $D(\ell)$ is reduced and it decays faster. Below in Section 7.1, it will be seen that when $t_\perp/t > 1.4$, the antibonding single-particle band becomes unoccupied, and the decrease in the strength of the pairing correlations is due to this effect. Using the data in Fig. 7.2 for $1 < \ell < 18$, $D(\ell)$ has been fitted to a form

$$D(\ell) = \frac{1}{\ell^\theta} \tag{7.4}$$

with a linear least-squares approximation. The resulting $\theta$ values are plotted as a function of $t_\perp/t$ for various fillings in Fig. 7.3. Here, it is seen that the minimum in $\theta$ versus $t_\perp/t$ depends on the filling, but it occurs for $t_\perp/t \sim 1.4$ near half-filling. For $t_\perp/t > 1.4$, the antibonding band is no longer occupied and the pairing correlations decrease rapidly. Thus the pairing correlations are enhanced near the point at which the antibonding band moves through the Fermi level [Noack *et al.* 1995 and 1997, Yamaji and Shimoi 1994].

Another measure of the strength of the pair-field correlations which can be used is the average
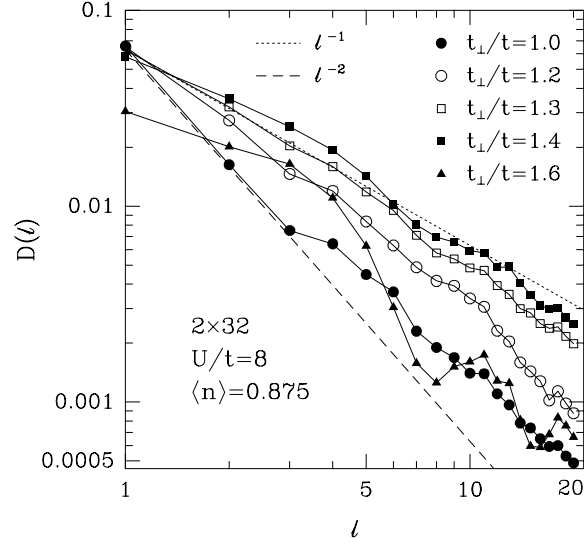
Figure 7.2: Pair-field correlation function $D(\ell)$ versus $\ell$ for various values of $t_\perp/t$ with $U = 8t$ and $\langle n \rangle = 0.875$.
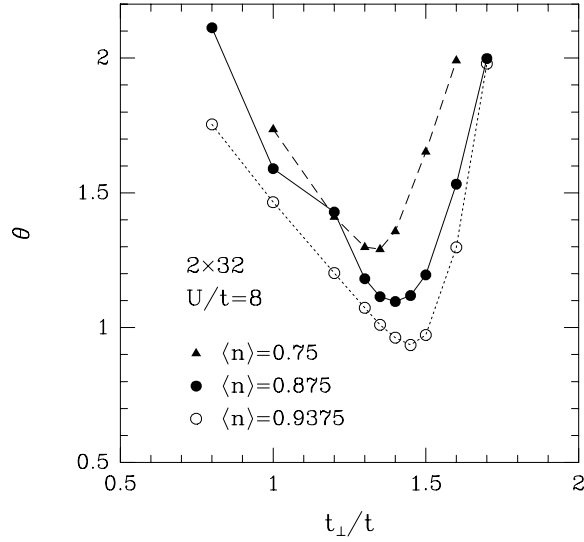


Figure 7.3: Exponent $\theta$ versus $t_\perp/t$ for $U/t = 8$ and various values of $\langle n \rangle$.

of $D(\ell)/D(1)$ for rung separations $\ell = 8$ to $12$:

$$\overline{D} = \frac{1}{5} \sum_{\ell=8}^{12} \frac{D(\ell)}{D(1)}. \tag{7.5}$$

Figure 7.4 shows $\overline{D}$ versus $t_\perp/t$ for $U = 8t$ at various fillings. This clearly shows how sensitively the pairing correlations depend on the value of $t_\perp/t$. Next, the variation of $\overline{D}$ with $U/t$ is shown

in Fig. 7.5. In this figure, the crosses represent the results for $U = 0$. Hence, the onsite Coulomb repulsion can significantly enhance the pairing correlations for a range of $t_\perp/t$ values. Here, one also observes that the enhancement of $\overline{D}$ is strongest for $U/t$ between 3 and 8, which is in the intermediate coupling regime. In addition, as $U/t$ increases the value of $t_\perp/t$ at which the peak in $\overline{D}$ occurs shifts towards smaller values. Hence, the strength of the pairing correlations is a sensitive function of $t_\perp/t$, $U/t$ and $\langle n \rangle$.
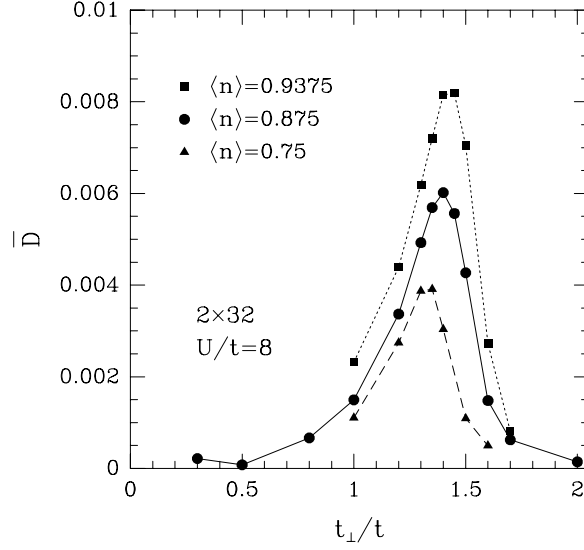


Figure 7.4: Averaged pair-field correlation function $\overline{D}$ versus $t_\perp/t$ for $U = 8t$ and various values of $\langle n \rangle$.

These DMRG results have a special place in many-body physics. They represent the first case in an exact ground-state calculation for a bulk system where the pair-field correlation function gets enhanced by turning on an onsite Coulomb repulsion. These calculations were carried out on ladders with up to 32 rungs resulting in negligible finite-size effects. As seen in Section 6.1, in the 2D Hubbard model, it was found that by turning on the Coulomb repulsion the $d_{x^2-y^2}$-wave pair-field susceptibility $P_d$ gets enhanced with respect to $\overline{P}_d$. However, $P_d$ was always found to be suppressed with respect to the pair-field susceptibility $P_d^0$ of the $U = 0$ system. This meant that, at these temperatures, the effective attractive interaction in the $d_{x^2-y^2}$-wave channel is not sufficiently strong to overcome the suppression of $P_d$ induced by the single-particle self-energy effects. Here, it is seen that for the 2-leg Hubbard ladder in the ground state, $\overline{D}$ can get enhanced over the $U = 0$ result for a set of the model parameters.

## 7.2 QMC results

In order to understand these DMRG results better, in this section QMC data on the 2-leg Hubbard ladder will be shown.

### 7.2.1 Single-particle spectral weight

The single-particle properties of the 2-leg Hubbard ladder at half-filling were studied in Ref. [Endres et al. 1996]. Here, the evolution of the single-particle spectral weight $A(\mathbf{k}, \omega)$ with $t_\perp/t$ will be
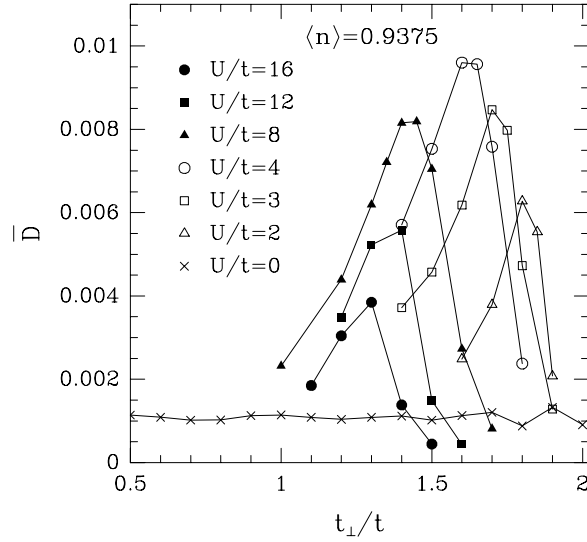
Figure 7.5: Averaged pair-field correlation function $\overline{D}$ versus $t_\perp/t$ for $\langle n \rangle = 0.9375$ and various values of $U/t$.

shown for the doped case. These data, which were obtained for a $2 \times 16$ ladder with periodic boundary conditions along the chains, are from Ref. [Noack *et al.* 1997]. The comparison of the results on $A(\mathbf{k}, \omega)$ and $D(\ell)$ will show that the pairing correlations are enhanced for $t_\perp/t$ such that the bottom of the antibonding band moves through the Fermi level.

The results on $A(\mathbf{k}, \omega)$ were obtained by the maximum-entropy analytic continuation of the Monte Carlo data. Figures 7.6 and 7.7 show data for $U/t = 2$ and 4, respectively. In these figures $\langle n \rangle = 0.94$ and $T = 0.125t$, and the results are given for various values of $t_\perp/t$. Here, $A(\mathbf{k}, \omega)$ is shown for both $k_\perp = 0$ (bonding) and $k_\perp = \pi$ (antibonding) bands as a contour plot in the $\omega$-$k$ plane where the intensity of the shading represents the magnitude of $A(\mathbf{k}, \omega)$ and $k$ is the momentum along the chains. In the $U = 0$ system, the quasiparticle dispersion consists of the bonding and the antibonding bands given by

$$\varepsilon_{\mathbf{k}} = -2t \cos k \pm 2t_\perp, \tag{7.6}$$

where $\mathbf{k} = (k, k_\perp)$. The dotted curves in Fig. 7.6 represent $\varepsilon_{\mathbf{k}}$ for $U = 0$. Here, it is seen that the dispersion obtained for $U/t = 2$ closely follows that of the $U = 0$ system. Note also that for $t_\perp/t = 1.8$ the bottom of the antibonding band is located right at the Fermi level while for $t_\perp/t = 2.0$ the antibonding band becomes unoccupied. In Fig. 7.5, it was seen that the pairing correlations for $U/t = 2$ are strongest when $t_\perp/t = 1.8$. This comparison suggests that it is the variation in the single-particle spectral weight with $t_\perp/t$ which controls the dependence of the pairing correlations on $t_\perp/t$.

Figure 7.7 shows similar data on $A(\mathbf{k}, \omega)$ for $U/t = 4$ and $t_\perp/t = 1.4$, 1.6 and 1.8. In this case, there are more differences between the QMC data and the $U = 0$ results denoted by the dotted curves. Here, the antibonding band becomes unoccupied for a smaller value of $t_\perp/t = 1.8$. One also notices that the top of the bonding and the bottom of the antibonding bands are flattened, especially for $t_\perp/t = 1.6$, increasing the amount of the single-particle spectral weight near the Fermi level. This behaviour is similar to the build up of spectral weight near $(\pi, 0)$ in the 2D Hubbard

Figure 7.6: Distribution of the single-particle spectral weight $A(\mathbf{k}, \omega)$ in the $\mathbf{k}$ and $\omega$ plane. The intensity of the shading indicates the amount of the spectral weight. These results are for $U = 2t$, $\langle n \rangle = 0.94$, $T = 0.125t$ and (a) $t_\perp/t = 1.6$, (b) 1.8 and (c) 2.0.

model as discussed in Section 5, and in the ARPES experiments on the high-$T_c$ cuprates which are reviewed by [Shen and Dessau 1995].

In the next section, it will be seen that for the 2-leg Hubbard ladder the irreducible particle-particle scattering vertex $\Gamma_I$ peaks at $(\pi, \pi)$ momentum transfer as for the 2D Hubbard model. These results suggest that the peaking of $\Gamma_I$ near $(\pi, \pi)$ momentum transfer along with the enhanced single-particle spectral weight enhances the pairing correlations, and this is the reason for the strong dependence of $\overline{D}$ on $t_\perp/t$ seen in Fig 7.4.

### 7.2.2 Irreducible particle-particle interaction

In the previous sections, it has been seen that the 2-leg Hubbard ladder has power-law $d_{x^2-y^2}$-wave pairing correlations in its ground state, and for a range of the model parameters the pairing correlations can get strong. It is useful to gain insight into the mechanism which leads to the $d_{x^2-y^2}$-wave pairing correlations in this model. For this reason, here the Monte Carlo results on the irreducible particle-particle interaction $\Gamma_I$ of the 2-leg Hubbard ladder will be reviewed. These are results from [Dahm and Scalapino 1997]. Comparisons with the magnetic susceptibility $\chi(\mathbf{q}, 0)$ will show that the short-range AF spin-fluctuations are responsible for the momentum structure in $\Gamma_I$ for $\mathbf{q}$ near $(\pi, \pi)$. Using the data on $\Gamma_I$ and the single-particle Green's function $G$, the Bethe-Salpeter equation will be solved in the particle-particle channel and the leading singlet pairing channel will be shown to have $d_{x^2-y^2}$-like symmetry.
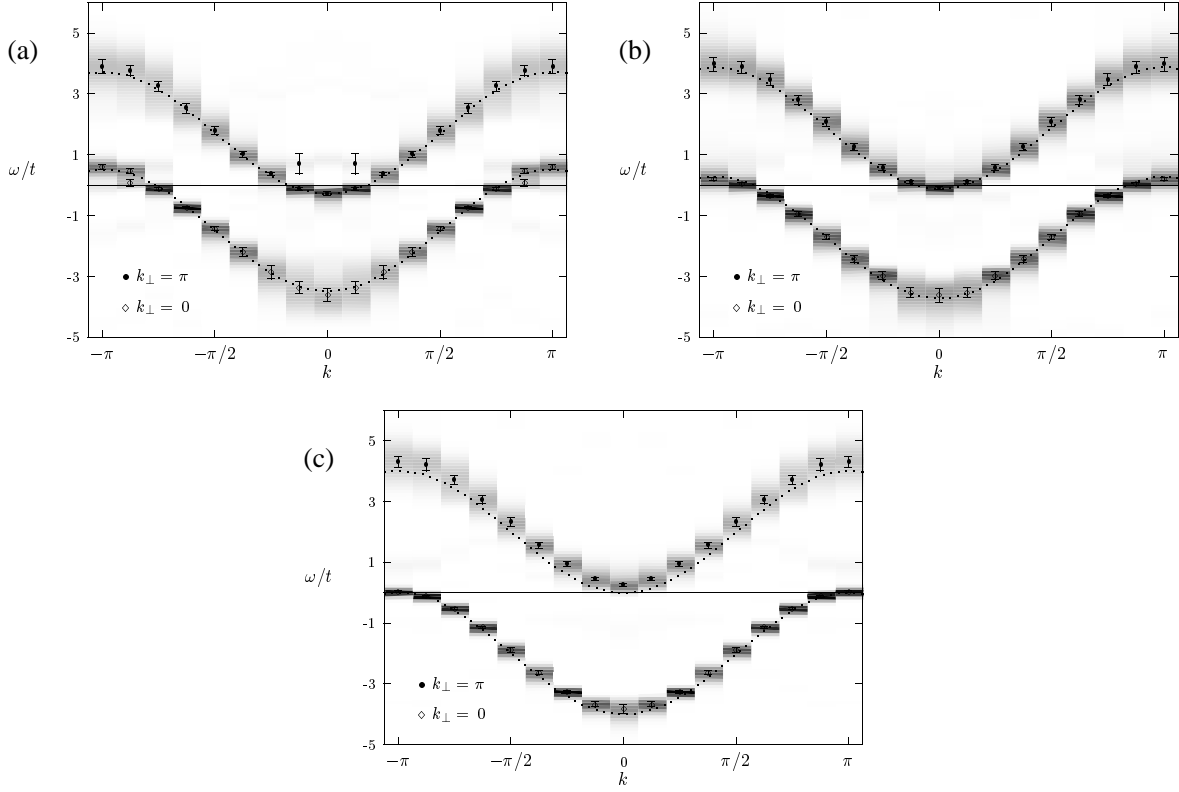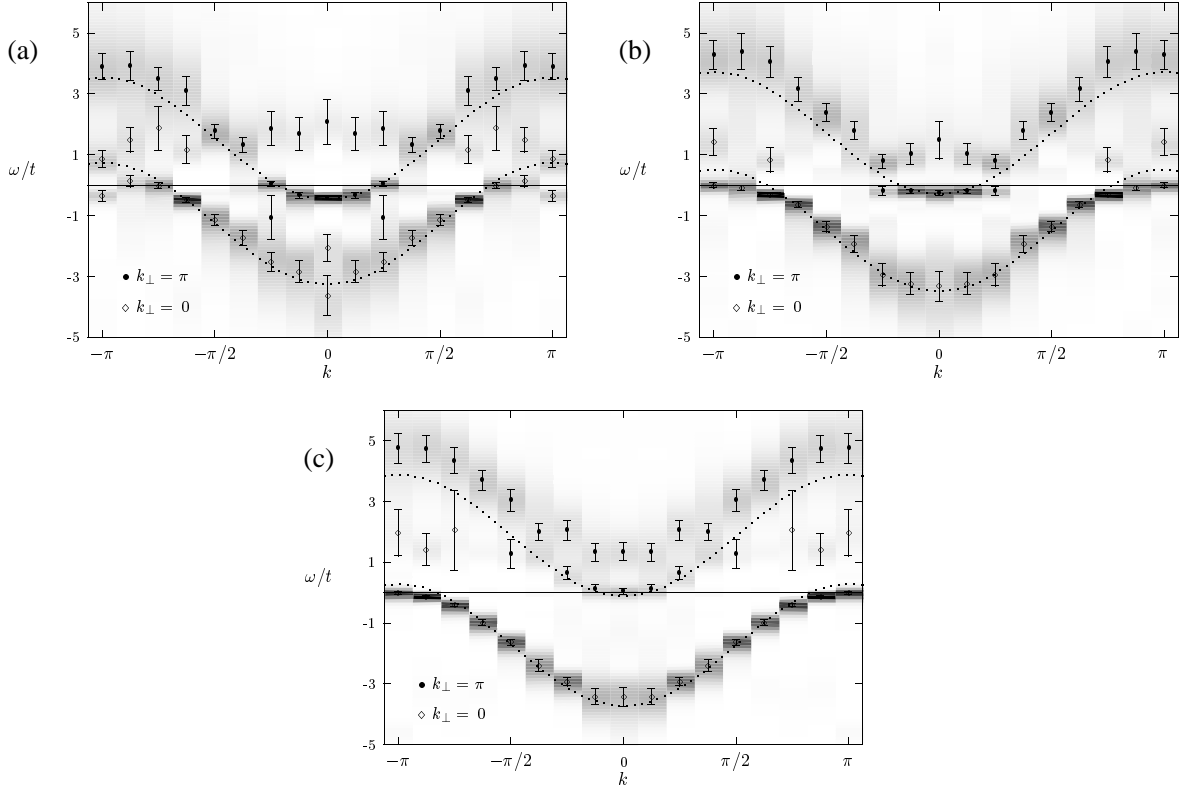
Figure 7.7: Distribution of the single-particle spectral weight $A(\mathbf{k}, \omega)$ in the $\mathbf{k}$ and $\omega$ plane. The intensity of the shading indicates the amount of the spectral weight. These results are for $U = 4t$, $\langle n \rangle = 0.94$, $T = 0.125t$ and (a) $t_\perp/t = 1.4$, (b) 1.6 and (c) 1.8.

Using Monte Carlo simulations, the singlet irreducible vertex $\Gamma_{Is}(\mathbf{q}, i\omega_m)$ has been calculated on a $2 \times 16$ lattice for $U/t = 4$ and $\langle n \rangle = 0.875$ in the same way as discussed in Section 6.2. In addition, here $t_\perp/t = 1.5$ was chosen so that the system has strong pairing correlations in the ground state. In Fig. 7.8(a), $\Gamma_{Is}(\mathbf{q}, i\omega_m = 0)$ is plotted as a function of $q$ where $\mathbf{q} = (q, \pi)$ at various temperatures. Here, as in Section 6, $\mathbf{q} = \mathbf{p} - \mathbf{p}'$ is the momentum transfer and $\mathbf{p}'$ is kept fixed at $(\pi, 0)$ while $\mathbf{p}$ is scanned. At high temperatures, $\Gamma_{Is}(\mathbf{q})$ is flat in momentum space with a magnitude varying between $8t$ and $10t$, and as $T$ is lowered to $0.25t$, $\Gamma_{Is}(\mathbf{q}, 0)$ develops significant amount of weight at $\mathbf{q} = (\pi, \pi)$ momentum transfer becoming of order $20t$. This behaviour is similar to what has been seen in Section 6 for the 2D Hubbard model.

Figure 7.8(b) shows the momentum dependence of the magnetic susceptibility $\chi(\mathbf{q}, 0)$ for the 2-leg Hubbard ladder for the same model parameters. Here, $\chi(\mathbf{q}, 0)$ is also plotted as a function of $q$ where $\mathbf{q} = (q, \pi)$. Comparing with Fig. 7.8(a), one observes that the evolution of $\Gamma_{Is}$ with temperature is closely related to that of $\chi(\mathbf{q}, 0)$, which implies that the short-range antiferromagnetic correlations are responsible for the momentum structure in $\Gamma_{Is}(\mathbf{q}, 0)$ for $\mathbf{q}$ near $(\pi, \pi)$.
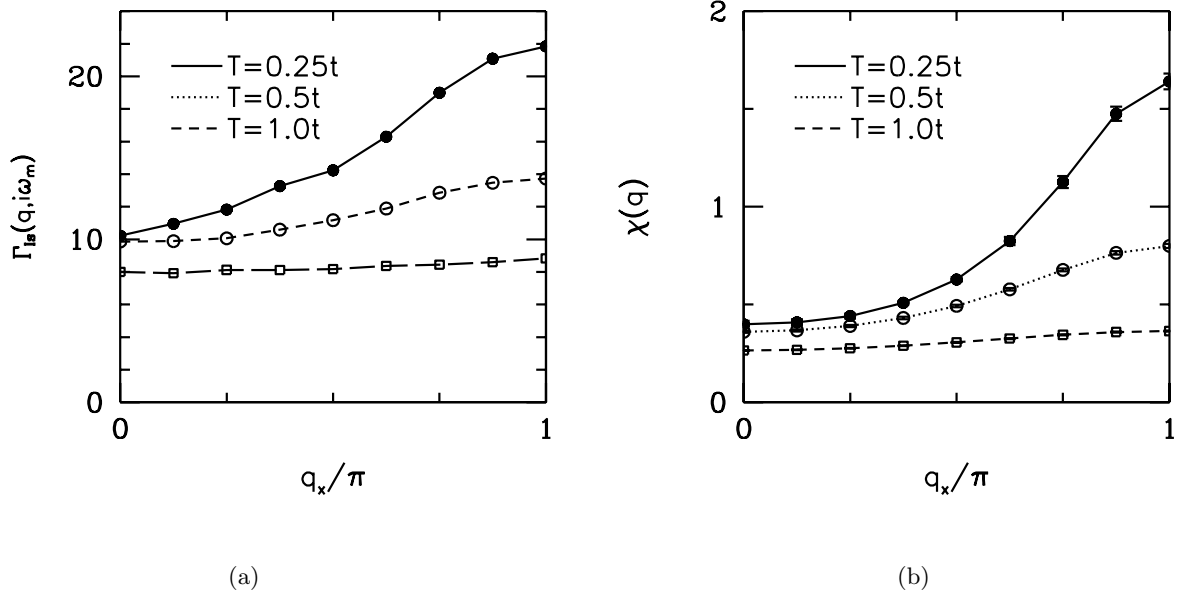
Figure 7.8: Monte Carlo results on the momentum dependence of (a) the irreducible particle-particle interaction in the singlet channel $\Gamma_{Is}(\mathbf{q}, i\omega_m = 0)$ and (b) the magnetic susceptibility $\chi(\mathbf{q}, i\omega_m = 0)$. These results were obtained on a $2 \times 16$ lattice for $U = 4t$, $T = 0.25t$, $\langle n \rangle = 0.87$ and $t_\perp = 1.5t$.
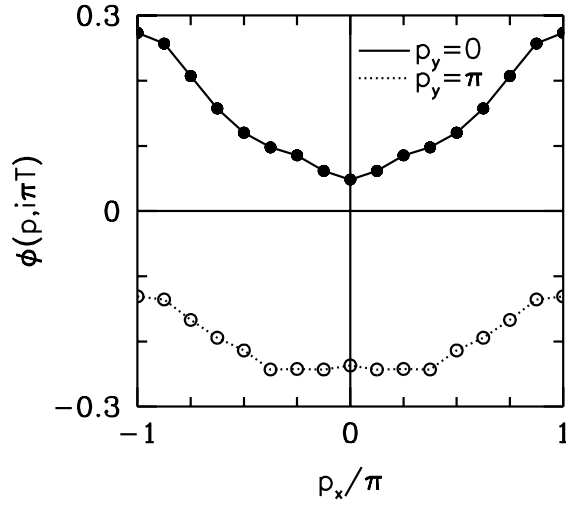


Figure 7.9: The leading singlet eigenfunction $\phi(\mathbf{p}, i\omega_n)$ versus $p_x$ where $\mathbf{p} = (p_x, p_y)$ and $\omega_n = \pi T$. These results were obtained on a $2 \times 16$ lattice for $U = 4t$, $T = 0.25t$, $\langle n \rangle = 0.87$ and $t_\perp = 1.5t$.

55
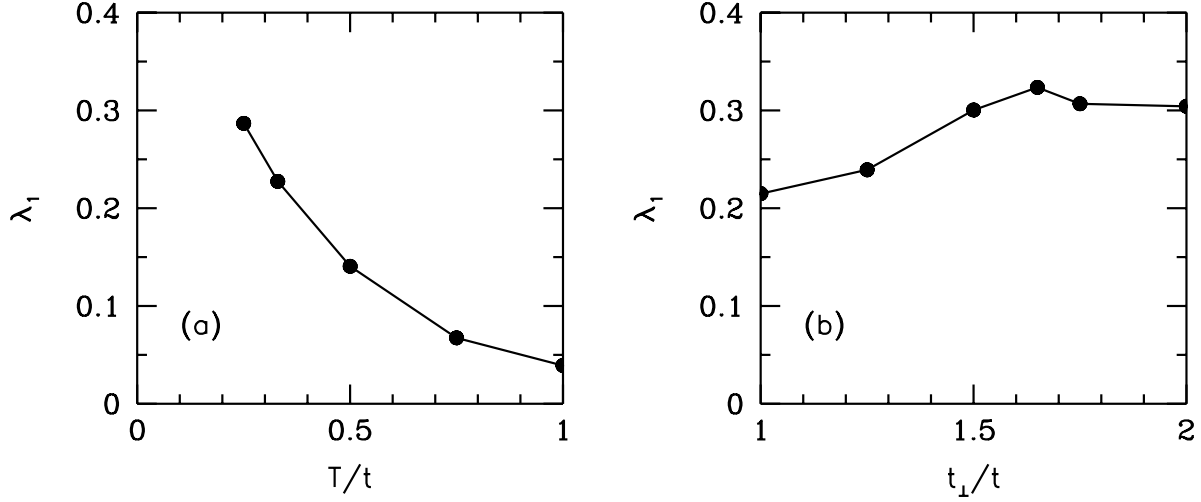
Figure 7.10: (a) Temperature and (b) $t_\perp/t$ dependence of the leading singlet eigenvalue $\lambda_1$. These results were obtained on a $2 \times 16$ lattice for $U = 4t$ and $\langle n \rangle = 0.87$. In (a) $t_\perp/t = 1.5$ and in (b) $T = 0.25t$ were used.

### 7.2.3 Bethe-Salpeter equation

In order to see what type of pairing state is favored by the irreducible particle-particle vertex seen in the previous section, here results from the solution of the Bethe-Salpeter equation

$$\lambda_\alpha \phi_\alpha(\mathbf{p}, i\omega_n) = -\frac{T}{N} \sum_{\mathbf{p}'} \Gamma_I(\mathbf{p} - \mathbf{p}', i\omega_n - i\omega_{n'})|G(\mathbf{p}', i\omega_n n')|^2 \phi_\alpha(\mathbf{p}', i\omega_{n'}) \tag{7.7}$$

from Ref. [Dahm and Scalapino 1997] will be shown. Figure 7.9 shows the momentum dependence of the leading eigenfunction $\phi(\mathbf{p}, i\omega_n)$ at $\omega_n = \pi T$ for $T = 0.25t$. Figures 7.10(a) and (b) show the dependence of the leading singlet eigenvalue $\lambda_1$ on $T/t$ and $t_\perp/t$, respectively. Note that $\phi(\mathbf{p}, i\pi T)$ peaks near $(\pi, 0)$ and $(0, \pi)$, and it changes sign between these two points. Hence, in this sense it is $d_{x^2-y^2}$-like, but it does not have a node since $\phi(\mathbf{p}, i\pi T)$ does not vanish near any of the four Fermi surface points. In the previous section, we have seen that for $t_\perp/t \sim 1.5$, the bonding band has spectral weight near the Fermi level for $\mathbf{p} \sim (\pi, 0)$, and the antibonding band has spectral weight near the Fermi level for $\mathbf{p} \sim (0, \pi)$. Hence, these Fermi points can be connected by scatterings involving $\mathbf{q} = (\pi, \pi)$ momentum transfer. Since $\Gamma_{Is}$ is large and repulsive for $\mathbf{q} \sim (\pi, \pi)$, the leading singlet eigenfunction $\phi$ of the Bethe-Salpeter equation has opposite signs for $\mathbf{p}$ near $(\pi, 0)$ and $(0, \pi)$.

In Fig. 7.10(a), it is seen that the eigenvalue of the $d_{x^2-y^2}$-like eigenfunction increases by about an order of magnitude as $T$ is lowered from $1t$ to $0.25t$. However, even at $T = 0.25t$, which is the lowest temperature where the Monte Carlo calculation of the Bethe-Salpeter eigenvalues can be carried out, the leading singlet eigenvalue is only about 0.3.

Figure 7.10(b) shows that at $T = 0.25t$ the leading singlet eigenvalue has in fact a weak dependence on $t_\perp/t$, and only a broad peak at $t_\perp/t = 1.6$ is seen. This is unexpected considering

the strong dependence of $\overline{D}$ on $t_\perp/t$ seen in the previous section. It means that at $T = 0.25t$ the pairing interaction has not reached its full strength and, in addition, the thermal smearing effects significantly weaken the pairing correlations which are observed in the ground state by the DMRG technique.

## 7.3 Comparison of the 2-leg and the 2D Hubbard models

It is interesting to compare these results on the 2-leg ladder with those on the 2D case seen in Section 6. In Fig. 7.10(b), one sees that at $T = 0.25t$, $U/t = 4$ and $t_\perp/t = 1.0$ the leading singlet eigenvalue is 0.22, which is slightly larger than $\lambda_d = 0.18$ at the same $U/t$, $\langle n \rangle$ and $T/t$ values for the 2D case. For $t_\perp/t = 1.0$, the DMRG calculations find that $D(\ell)$ varies approximately as $\ell^{-2}$ in the ground state and, hence, the pairing correlations are only as strong as in the $U = 0$ case. If one just uses this comparison of the eigenvalues for the 2-leg and the 2D cases, then one would expect weak pairing correlations in the ground state of the 2D Hubbard model. However, in 2D, $\lambda_d$ for $U = 8t$ is found to be higher than for $U = 4t$ at $T = 0.5t$. Furthermore, from the DMRG calculations one knows that when $t_\perp/t$ is tuned to the right value, in the 2-leg ladder strong pairing correlations can develop. A similar dependence on the model parameters, such as the second-nearest-neighbour hopping $t'$, could exist in the 2D Hubbard model.

It has been seen above that the QMC results on the irreducible particle-particle vertex of the 2-leg ladder are similar to those on the 2D Hubbard model. In the ground state of the 2-leg ladder, the DMRG calculations find enhanced $d_{x^2-y^2}$-wave pairing correlations in a certain range of the parameters. Both in the 2D and the 2-leg models, we have seen that, when doped with holes there are short-range AF correlations and that they strongly influence the low-energy single-particle properties. In both cases, short-range AF correlations cause $\Gamma_I(\mathbf{q}, 0)$ to peak at $(\pi, \pi)$ momentum transfer. It needs to be noted that the pairing correlations observed in these two models do not require a particularly sharp peak in $\Gamma_I(\mathbf{q}, 0)$ at $\mathbf{q} = (\pi, \pi)$, but rather simply weight at large momentum transfers.

Currently, it is not possible to determine whether the doped 2D Hubbard model has long-range $d_{x^2-y^2}$-wave superconducting order in its ground state, or, if it did, whether it would be sufficient to explain superconducting transition temperatures as high as those found in the cuprates. In spite of this, the results discussed above show that effects which increase the single-particle spectral weight near the $(\pi, 0)$ and $(0, \pi)$ points of the Brillouin zone as well as effects which increase the strength of the particle-particle interaction at $(\pi, \pi)$ momentum transfer will act to enhance $d_{x^2-y^2}$-wave pairing.

It is possible that the strength of the $d_{x^2-y^2}$ pairing correlations in the ground state of the 2D Hubbard model depends sensitively on the model parameters such as the second-near-neighbour hopping $t'$ in a way similar to what is seen for the 2-leg ladder in Section 7. In the 2-leg case, the pairing correlations are as weak as those of the $U = 0$ system when $t_\perp = t$. However, when $t_\perp/t$ is tuned so that the flat bands are located near the Fermi level, the system exhibits enhanced pairing correlations. It is possible that the 2D Hubbard model with only near-neighbour hopping similarly exhibits weak pairing correlations in the ground state, but there can be enhanced pairing when an additional parameter such as $t'$ is tuned. In the 2-leg ladder case, the value of $t_\perp/t$ for which the flat bands are near the Fermi level is renormalized by the Coulomb repulsion. Similarly, in the 2D case, the optimum value of $t'$ could be renormalized, and it is difficult to estimate it in advance. In a bilayer Hubbard model, the bilayer coupling could also play a role. These are issues which need to be resolved by exact techniques in the future.

Beyond these, one would expect that any additional contribution to the irreducible electron-

electron interaction which is repulsive for $\mathbf{q} \sim (\pi, \pi)$ momentum transfers or attractive for $\mathbf{q} \sim 0$ would act to enhance the $d_{x^2-y^2}$ pairing, when added to the 2D or the 2-leg Hubbard system. For instance, when a phonon mediated interaction which is most attractive for $\mathbf{q} \sim 0$ momentum transfers is added to an AF spin-fluctuation exchange interaction, it is found within the $t$-matrix approximation that the $d_{x^2-y^2}$ eigenvalue gets enhanced [Bulut and Scalapino 1996]. However, it is necessary to study such effects using exact techniques.

It could also be possible to design flat band dispersion near the Fermi level by controlling the lattice geometry and parameters [Imada and Kohno 2000]. Imada and Kohno have carried out exact diagonalization calculations for a 1D 16-site $t$-$J$ model with additional three-site terms and longer range hoppings. By tuning the longer-range hopping parameters, they have created flat band dispersion near the Fermi level and, in this case, they find an enhanced spin gap and an enhanced tendency for pairing. They have also proposed various multiband models which could exhibit flat bands near the Fermi level and enhanced pairing.

Even though for the 2D case the low-doping and the low-temperature regime where a spin gap could exist is beyond the reach of the exact techniques, in the 2-leg case the spin gap $\Delta_s$ can attain large values. In the doped 2-leg ladder, $\Delta_s$ is maximum when the bottom of the antibonding band is near the Fermi level [Noack $et\ al.$ 1996]. For instance, for $U = 8t$, $\langle n \rangle = 0.875$ and $t_\perp = 1.5t$, the spin gap has the value of $0.06t$, which corresponds to $\approx 300K$ for a $t$ of order 0.45 eV.

It is also useful to compare the density correlations seen in the 2-leg and the 2D Hubbard models. With the DMRG method [Noack $et\ al.$ 1996], the following density-density correlation function has been calculated for the $2 \times 32$ Hubbard ladder,

$$S(i, j, \lambda) = \langle n_{i\lambda} n_{j1} \rangle - \langle n_{i\lambda} \rangle \langle n_{j1} \rangle. \tag{7.8}$$

Here, $n_{i\lambda}$ is the electron occupation number at the $i$'th site of chain $\lambda$. By Fourier transforming, $S(\mathbf{q})$ has been obtained for $U = 8t$, $\langle n \rangle = 0.875$ and various values of $t_\perp/t$. No obvious feature is found in $S(\mathbf{q})$ at the "$2\mathbf{k}_F$" wave vector of the 2-leg Hubbard ladder, which is $\mathbf{q}^* = (q^*, \pi)$ with $q^* = \pi\langle n \rangle$. On the other hand, a feature is observed at the "$4\mathbf{k}_F$" wave vector, which corresponds to $(\pi/4, 0)$ for $\langle n \rangle = 0.875$. Especially for $t_\perp/t = 1.5$, this feature becomes more obvious. In order to isolate the "$4\mathbf{k}_F$" component of the density correlations, a correlation function $N(\mathbf{q})$ involving four density operators has been calculated. This correlation function exhibits a clear peak at $(\pi/4, 0)$ for both $t_\perp/t = 1.0$ and 1.5, and in real space it decays as power law, while $S(i, j, \lambda)$ decays exponentially.

The results on the 2-leg Hubbard ladder show that, when doped, this model exhibits simultaneously short-range AF correlations and power-law decaying $d_{x^2-y^2}$-like superconducting and "$4\mathbf{k}_F$" density correlations. For $t_\perp/t \sim 1.5$, the superconducting correlations decay more slowly than the "$4\mathbf{k}_F$" density correlations. The 2D Hubbard model also exhibits short-range AF and $d_{x^2-y^2}$ superconducting correlations. In addition, the QMC data on the 2D case seen in Section 4 imply that the features found in the density susceptibility $\Pi(\mathbf{q}, i\omega_m = 0)$ might be related to the "$4\mathbf{k}_F$" wave vectors rather than "$2\mathbf{k}_F$" for large $U/t$. Hence, the 2-leg and the 2D Hubbard models, when doped, appear to have similar magnetic, superconducting and density properties. Furthermore, in both cases, the single-particle dispersion near the $(\pi, 0)$ and $(0, \pi)$ points get flattened by the many-body effects. These flat bands also seem to play a key role in determining the strength of the pairing correlations in both models. At this point, it is necessary to note that in order to compare the 2-leg Hubbard model with the 2D case, one should not use isotropic hopping, $t_\perp/t = 1.0$, since in this case the Fermi surface points are not connected by scatterings involving $\mathbf{Q} \sim (\pi, \pi)$ momentum transfers. Instead, anisotropic hopping, where the bonding and the antibonding Fermi surface points can be connected by $(\pi, \pi)$ scatterings, need to be used.

Finally, an important question is whether the 2D Hubbard model exhibits spin-charge separation as in the 1D case [Kivelson *et al.* 1987, Anderson *et al.* 1987]. While the 2D case cannot be resolved currently, in the 2-leg Hubbard ladder no indications of spin-charge separation as in the 1D Hubbard model have been found [Noack *et al.* 1996].

# 8   Discussion

The numerical results discussed above point out that the short-range AF spin fluctuations are responsible for the $d_{x^2-y^2}$-wave superconducting correlations. The relation of the AF spin fluctuations to the $d_{x^2-y^2}$-wave superconductivity has been studied using various diagrammatic approaches. Perhaps, the most commonly used of these approaches is the fluctuation exchange (FLEX) approximation [Bickers *et al.* 1989], which self-consistently treats the fluctuations in the magnetic, density and the pairing channels. The FLEX technique has been used for obtaining possible phase diagrams and the estimates of the superconducting transition temperatures. In Section 8.1 below, a comparison of the QMC data with the results of the FLEX approach to the 2D Hubbard model will be carried out for the single-particle and the pairing properties. The purpose of this comparison is to have an idea for the range of applicability of the FLEX approximation, and see how it should be extended further. Another reason for carrying out such a comparison is because the Eliashberg type of calculations of the $T_c$'s using the spin fluctuations for the cuprates [Monthoux and Pines 1992] or the similar self-consistent spin-fluctuation exchange calculations [Moriya *et al.* 1990] are basically at the same level with the FLEX approximation. Hence, it is of interest to compare with the exact QMC calculations.

It will be seen that for $U = 4t$, the FLEX provides results in excellent agreement with the QMC data on the density of states $N(\omega)$ and the Bethe-Salpeter eigenvalues in the pairing channel at the temperatures where the QMC calculations are carried out, as found earlier [Bickers *et al.* 1989]. For stronger coupling $U = 8t$, there are differences between the FLEX and the QMC results. The correlated metallic band which develops by doping the AF Mott-Hubbard insulator is not obtained within FLEX and this affects the strength of the $d_{x^2-y^2}$-wave pairing correlations.

Following this, in Section 8.2, other types of Monte Carlo approaches to the Hubbard model, in particular the variational and the projector Monte Carlo algorithms, will be briefly discussed. In Section 8.3, the results of the recent dynamical-cluster approximation and the one-loop RG calculations for $d_{x^2-y^2}$ pairing in the 2D Hubbard model will be discussed. There is also much interest in understanding the unusual normal state properties of the cuprates in the pseudogap regime. The origin and the implications of the pseudogap are important issues in this field. In Section 8.4, various calculations on the low-doping regime of the 2D Hubbard model will be discussed briefly and their results will be compared with the pseudogap seen in the cuprates.

The $t$-$J$ model which is closely related to the Hubbard model has also drawn broad attention. It is useful to compare the QMC and the DMRG results on the Hubbard model with the numerical studies of the $t$-$J$ model. Below, in Section 8.5, such a comparison will be given. Here, the attention will be concentrated on the density and the pairing properties since that is where there are unresolved issues. A question of interest is whether in the ground state of the doped 2D Hubbard model there are special density correlations as seen in the $t$-$J$ model, for instance, phase separation or stripes, and, if so, whether they would suppress the $d_{x^2-y^2}$-wave pairing correlations observed at higher temperatures with the QMC simulations.

In Section 8.6, what these numerical studies of the Hubbard model imply for the mechanism of the $d_{x^2-y^2}$-wave superconductivity seen in the high-$T_c$ cuprates will be discussed. The issue which will be addressed here is whether the 2D Hubbard model, or some variation of it, is sufficient for

explaining why the values of the $T_c$'s found in the cuprates are so high.

## 8.1 Comparisons with the fluctuation-exchange approach to the 2D Hubbard model

The FLEX approximation was used first by Bickers *et al.* to study $d_{x^2-y^2}$-wave superconductivity in the 2D Hubbard model [Bickers *et al.* 1989, Bickers and White 1991]. This approach self-consistently incorporates the fluctuations in the magnetic, density and the pairing channels. It is an approximation around the band limit, and it is conserving in the sense that the microscopic conservation laws for the particle number, energy, and momentum are obeyed. Within FLEX, it is found that the $d_{x^2-y^2}$ pairing correlations are mediated by the AF spin fluctuations. The phase diagram of the $U = 4t$ Hubbard model within the FLEX approximation is shown in Fig. 8.1. The FLEX calculations find a finite mean-field Neel temperature at half-filling and at small dopings up to 6%. Neighboring the SDW phase is a $d_{x^2-y^2}$-wave superconducting phase which is stabilized for dopings between 6% and 20%. Note that in the 2D Hubbard model, a finite Neel temperature is not possible and only a Kosterlitz-Thouless type of superconducting transition can occur. Hence, the finite transition temperatures seen in Fig. 8.1 represent transitions to regimes where the $d_{x^2-y^2}$ correlations have a power law decay at finite $T$. In order to induce true long-range order at finite temperature, three dimensional couplings would be required.
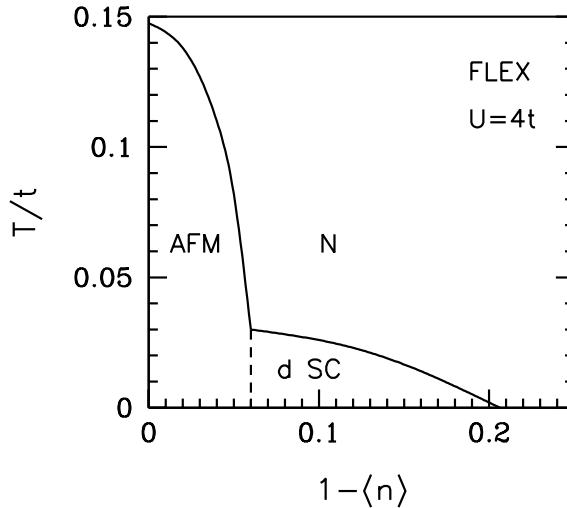


Figure 8.1: Sketch of the phase diagram of the 2D Hubbard model within the FLEX approximation for $U = 4t$. From [Bickers *et al.* 1989, Bickers and White 1991].

In addition, using the FLEX approximation the effects of the nearest-neighbor hopping $t'$ has been investigated for the 2D Hubbard model [Monthoux and Scalapino 1994, Dahm and Tewordt 1995]. This approach has been also used for studying a three-band $CuO_2$ model which has nearest neighbor copper-oxygen hopping and an onsite Coulomb repulsion at the Cu sites [Luo and Bickers 1993]. The solutions of the FLEX equations in the $d_{x^2-y^2}$-wave superconducting state were also obtained [Pao and Bickers 1994 and 1995, Monthoux and Scalapino 1994, Dahm and Tewordt 1995]. In the following, a comparison of the FLEX results with the QMC data will be carried out using

results from Ref. [Dahm and Bulut 1996]. First the single-particle properties and then the pairing correlations will be discussed. Figure 8.2 compares the QMC data on the density of states $N(\omega)$ with the FLEX results for various values of $U/t$ at $\langle n \rangle = 0.87$. While for $U = 4t$, the results from the two different approaches are similar at these temperatures, there are qualitative differences for $U = 8t$ and $12t$. The Fermi level within FLEX moves slower with the doping at large $U/t$. The correlated metallic band at the Fermi level as well as the lower and the upper Hubbard bands and the Mott-Hubbard pseudogap are not obtained within the FLEX approximation. For $U = 4t$ and $T = 0.33t$, the FLEX and the QMC results have similar qualitative features. However, at lower temperatures $N(\omega)$ could develop a pseudogap for $U = 4t$ also. Figure 8.3 shows the temperature evolution of $N(\omega)$ for $U = 8t$ and $\langle n \rangle = 0.87$ within the FLEX approximation. Comparing this with Fig. 5.3, one sees that the differences with the QMC data continue to exist as $T$ is lowered. In Fig. 8.4, the QMC and the FLEX results on $N(\omega)$ are compared at half-filling for $U = 8t$ and $T = 0.5t$. Here, it is seen that the development of the Mott-Hubbard gap at half-filling is not obtained within FLEX.
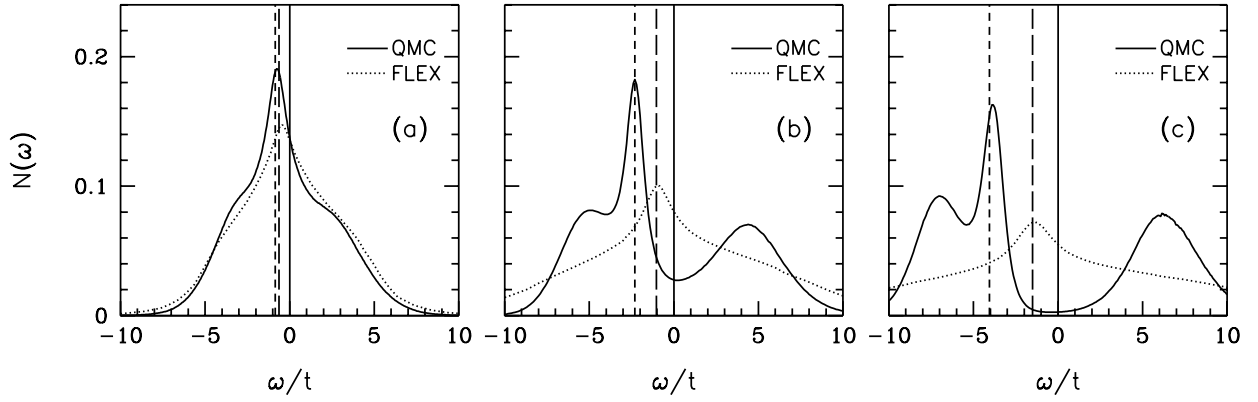


Figure 8.2: Comparison of the FLEX and the QMC results on $N(\omega)$ versus $\omega$ at $\langle n \rangle = 0.875$ for (a) $U = 4t$, (b) $U = 8t$, and (c) $U = 12t$. In (a) and (b) $T = 0.33t$ was used and in (c) $T = 0.5t$. Here, the vertical long-dashed and the short-dashed lines denote the chemical potential for the FLEX and the QMC calculations, respectively.

Next, the FLEX results on the $d_{x^2-y^2}$-wave eigenvalue $\lambda_d$ of the Bethe-Salpeter equation in the particle-particle channel will be shown. In Fig. 8.5, $\lambda_d$ is plotted as a function of $T/t$ for $U/t = 4$ and 8 in the temperature regime where the QMC data exist. Here, it is seen that as $U/t$ increases from 4 to 8, $\lambda_d$ changes by a small amount. For $U = 4t$, the FLEX results on $\lambda_d$ versus $T/t$ are in good agreement with the QMC data. However, for $U = 8t$ the FLEX approximation underestimates $\lambda_d$ by about a factor of two. This is the major difference between the QMC and the FLEX results on $\lambda_d$. Within FLEX the effective pairing interaction is also attractive in the odd-frequency $s$ and $p$-wave channels, in addition to the even-frequency $d$-wave channel.

Comparing Fig. 5.3 with Fig. 8.3, one sees that the density of states at the Fermi level is also underestimated by about a factor of two within FLEX. From the simple spin-fluctuation exchange form of Eq. (2.1), one expects that the $d_{x^2-y^2}$-wave pairing interaction increases with $U/t$. As discussed in Section 6.2, the QMC data also shows that the reducible vertex $\Gamma_s$ gets enhanced as $U/t$ is increased from 4 to 8, even though the irreducible vertex $\Gamma_{Is}$ could not be obtained for this value of $U/t$. Hence, it must be that the FLEX approach underestimates the amount of the
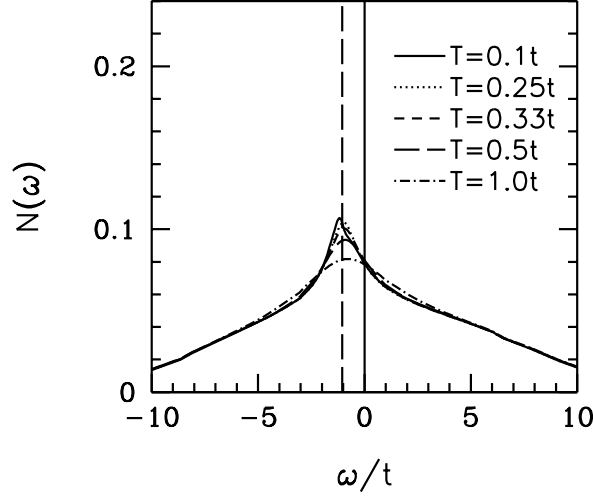
Figure 8.3: Temperature evolution of $N(\omega)$ versus $\omega$ within the FLEX approximation for $U = 8t$ and $\langle n \rangle = 0.875$. Here, the vertical long-dashed line denotes the chemical potential.
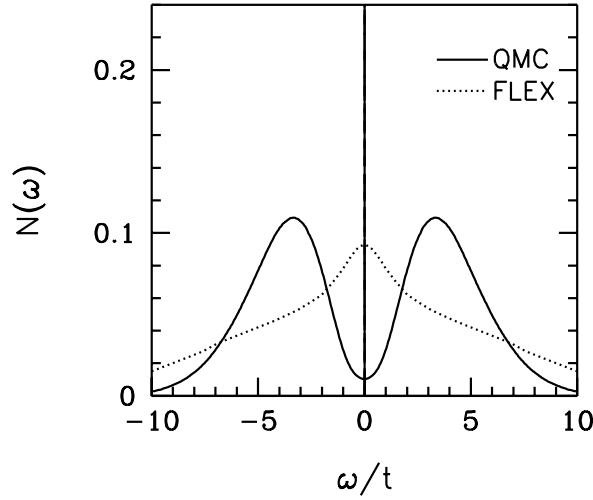


Figure 8.4: Comparison of the FLEX and the QMC results on $N(\omega)$ versus $\omega$ at half-filling for $U = 8t$ and $T = 0.5t$.

single-particle spectral weight at the Fermi level, and this causes the $d_{x^2-y^2}$-wave eigenvalue to be smaller with respect to the QMC value.

Here, it is seen that the correlated metallic band which forms upon doping the AF Mott-Hubbard insulator is not obtained within FLEX, which appears to cause why the FLEX underestimates $\lambda_d$ for $U = 8t$. Whether similar effects could take place when a CDW insulator is doped is an interesting
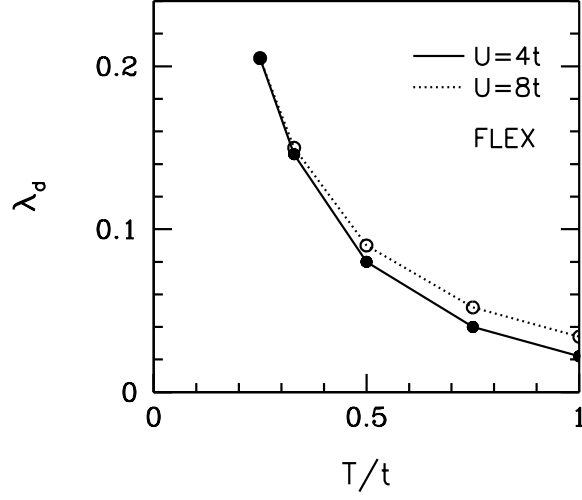
Figure 8.5: Temperature dependence of the $d_{x^2-y^2}$-wave eigenvalue within the FLEX approximation at $\langle n \rangle = 0.875$ for $U = 4t$ and $8t$.

problem.
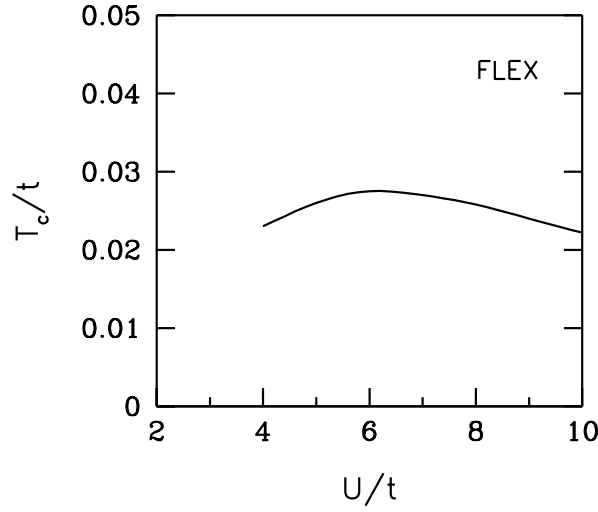


Figure 8.6: Superconducting transition temperature $T_c$ versus $U/t$ within the FLEX approximation for $\langle n \rangle = 0.875$. From [Pao and Bickers 1994].

Above, it has been seen that within FLEX $\lambda_d$ has a weak dependence on $U/t$ at temperatures between $0.25t$ and $1.0t$. Related to this is Fig. 8.6 which shows the transition temperature $T_c$ obtained within FLEX as a function of $U/t$. Here, it is seen that $T_c$ has a broad peak at $U \sim 6t$. In this section, it has been seen that the FLEX underestimates the strength of the $d_{x^2-y^2}$-wave

pairing when $U$ is of order $8t$. An important question raised by these comparisons is whether for $U \sim 8t$ the $T_c$ should be higher than $0.025t$. There is a chance that the maximum possible $T_c$ in the 2D Hubbard model is higher than the FLEX estimate. However, note that these values for $T_c$ are just estimates for a possible Kosterlitz-Thouless transition. In fact, the ground state of the doped 2D Hubbard model is not known, and it is currently beyond the reach of the exact many-body calculations.

## 8.2 Other Monte Carlo results on the 2D Hubbard model

The QMC data presented in the previous sections were obtained with the determinantal Monte Carlo technique [White $et\ al.$ 1989b]. Variational and projector Monte Carlo algorithms were also used for studying the 2D Hubbard model. However, these approaches have arrived at different conclusions about the possibility of the $d_{x^2-y^2}$-wave pairing. In this section, some of these calculations will be reviewed briefly.

In order to see whether superconducting long-range order develops in the ground state of the doped 2D Hubbard model, zero temperature projector Monte Carlo calculations have been carried out [Imada 1991, Furukawa and Imada 1992]. In these calculations, an optimised initial state was used as a guiding function, mitigating the sign problem but making the calculation variational rather than exact. With this technique, the equal-time pair-field correlation functions were calculated for the $s$, extended $s$ and the $d_{x^2-y^2}$-wave singlet pairing channels. However, no size dependence was found in the data, which implies that there is no long-range superconducting order with these symmetries in the ground state.

The constrained-path Monte Carlo (CPMC) algorithm developed in Ref. [Zhang $et\ al.$ 1995] is a variational method which starts from a trial wave function $|\Psi_T\rangle$ and uses the same $|\Psi_T\rangle$ as a constraining wave function as the simulation is carried out in the space of the Slater determinants. In calculations on up to $16 \times 16$ lattices, free-electron and unrestricted Hartree-Fock wave functions were used as $|\Psi_T\rangle$, however no $d_{x^2-y^2}$-wave superconducting long-range order was found [Zhang $et\ al.$ 1997]. The CPMC method has been extended by using as the constraining function a $d_{x^2-y^2}$-wave BCS wave function [Guerrero $et\ al.$ 1999]. Superconducting long-range order was not found in this case either. An important issue is how well the constraining function describes the correlations in the Hubbard model. In fact, a comparison of the CPMC and the DMRG results, which will be discussed later in Section 8.5.1, has been carried out for the magnetic and the density correlations in the $12 \times 3$ Hubbard model [Bonca $et\ al.$ 2000]. This comparison has found that the CPMC results depend sensitively on the constraining wave function especially for large $U/t \sim 8$. In this respect, it would be useful to test how well the CPMC method describes the $d_{x^2-y^2}$-like superconducting correlations found in the 2-leg Hubbard ladder. For instance, it is known from the DMRG calculations that in the 2-leg Hubbard ladder for $U/t = 8$, $t_\perp/t \sim 1.5$ and near half-filling the pair-field correlation function $D(\ell)$ decays as $\ell^{-\theta}$, where $\theta \lesssim 1.0$. It would be useful to see whether the CPMC method describes the power-law pairing correlations which exist in the 2-leg Hubbard ladder.

Another variational Monte Carlo approach uses as the trial wave function [Nakanishi $et\ al.$ 1997, Yamaji $et\ al.$ 1998]

$$|\Psi_T\rangle = P_N P_G |\Psi_{BCS}\rangle, \qquad (8.1)$$

where

$$|\Psi_{BCS}\rangle = \Pi_{\mathbf{k}}(u_{\mathbf{k}} + v_{\mathbf{k}} c^\dagger_{\mathbf{k}\uparrow} c^\dagger_{-\mathbf{k}\downarrow})|0\rangle \qquad (8.2)$$

is the usual $d_{x^2-y^2}$-wave BCS wave function,

$$P_G = \Pi_i[1 - (1 - g)n_{i\uparrow}n_{i\downarrow}], \tag{8.3}$$

is the Gutzwiller projection operator, and $P_N$ is an operator which projects out states with electron number $N$. In this method, the magnitude of the $d_{x^2-y^2}$-wave gap function entering the usual BCS coefficients $u_{\mathbf{k}}$ and $v_{\mathbf{k}}$, the parameter $g$, and the chemical potential $\mu$ are used as variational parameters, and their values are determined by minimising the ground state energy with a Monte Carlo simulation. With this method it is found that, for fillings between 0.84 and 0.68, the $d_{x^2-y^2}$-wave state has the lowest energy, and for $\langle n \rangle \gtrsim 0.84$ an SDW state is favored. In addition, when a next-near-neighbor hopping term $t'$ is turned on, the superconducting condensation energy gets enhanced. For instance, for $U = 8t$ this enhancement is maximum when $t' \approx -0.1t$. It should be noted that this method was also applied to the 2-leg Hubbard ladder [Koike *et al.* 2000]. In this case, the gap function was assumed to take momentum-independent values $\Delta_1$ and $\Delta_2$ on the bonding and the antibonding bands. Treating $\Delta_1$ and $\Delta_2$ as variational parameters, it was found that a superconducting state with $d_{x^2-y^2}$-like symmetry is stabilized when the bottom of the antibonding band is near the Fermi level, which is in agreement with the exact-diagonalization [Yamaji and Shimoi 1994] and the DMRG [Noack *et al.* 1995 and 1997] calculations.

Next, a projector Monte Carlo approach [Husslein *et al.* 1996] will be discussed where the ground state wave function of the 2D Hubbard model is estimated from

$$|\Psi_g\rangle = e^{\theta H}|\Psi_0\rangle. \tag{8.4}$$

Here, $|\Psi_0\rangle$ is the ground state of the noninteracting electrons and the parameter $\theta$ is taken to be about 8 on a $12 \times 12$ lattice. This approach has been used to calculate the $d_{x^2-y^2}$-wave pair-field correlation function in the weak-coupling regime, $0.5t < U < 3t$, near half-filling. It is found that the system has long-range $d_{x^2-y^2}$-wave pairing correlations for negative values of $t'$, for instance, at $t' = -0.3t$ for $U = 2t$.

In this section, it was seen that various approaches arrive at different conclusions about $d_{x^2-y^2}$-wave pairing in the 2D Hubbard model. This emphasises the importance of the choice of the trial wave functions and points out at the need for carrying out calculations without introducing approximations.

## 8.3 Dynamical cluster approximation and RG calculations for $d_{x^2-y^2}$ pairing in the 2D Hubbard model

Recently, the dynamical cluster approximation [Maier *et al.* 2000] and the one-loop renormalization-group method employing a 2D Fermi surface [Zanchi and Schulz 2000, Halboth and Metzner 2000, Honerkamp *et al.* 2001] were used for studying $d_{x^2-y^2}$ pairing in the 2D Hubbard model. In this section, the findings of these studies will be discussed briefly.

When the infinite dimensions limit of the Hubbard model is taken with proper scaling, the many-body problem becomes local [Metzner and Vollhardt 1989, Müller-Hartman 1989], and it can be mapped to an Anderson impurity problem, which can then be solved with various many-body techniques [Pruschke *et al.* 1995, Georges *et al.* 1996]. This is called the dynamical mean-field approximation (DMFA). The DMFA is interesting because it is a strong coupling technique. For instance, for large $U/t$ and off of half-filling, the DMFA yields a narrow peak in $N(\omega)$ near the Fermi level [Jarrell 1992], which is also seen in the 2D QMC data. However, the DMFA does not incorporate the non-local correlations, and hence it is not possible to study $d_{x^2-y^2}$ pairing with it. The DCA incorporates the non-local corrections to DMFA by mapping the lattice problem

onto an embedded cluster of size $N_c$, rather than onto an impurity problem. In DCA calculations, the dynamical correlation length is restricted to $L = \sqrt{N_c}$, and the DCA would become exact for $N_c \to \infty$, while it reduces to DMFA for $N_c = 1$. With this approach, the mean-field $d_{x^2-y^2}$ superconducting $T_c$'s were calculated for $N_c = 4$ by using the non-crossing approximation to solve the cluster problem [Maier *et al.* 2000]. For $U = 12t$, it is found that $T_c$ has the maximum value of $\approx 0.05t$ for about 20% doping. It is also found that $T_c$ increases for positive values of the second-nearest-neighbour hopping $t'$, and decreases for negative values of $t'$. This result agrees with the DMRG calculations on the $t$-$J$ model which find $d_{x^2-y^2}$ pairing for $t' > 0$ [White and Scalapino 1998a]. With DCA, the low doping regime of the 2D Hubbard model was also studied, and these results will be discussed in Section 8.4.

After the discovery of the high $T_c$ cuprates, the one-loop RG approach was extended from 1D to 2D in order to study this problem [Dzyaloshinskii 1987, Schulz 1987, Lederer *et al.* 1987]. The RG calculations are interesting, because with this technique the particle-particle and the particle-hole channels are treated on equal footing. These studies focused on the scattering processes between the Fermi surface regions near the van Hove singularities. For the 2D Hubbard model, the AF SDW state at half-filling and the $d_{x^2-y^2}$ superconducting state induced by AF fluctuations away from half-filling were found [Schulz 1987, Lederer *et al.* 1987]. The scatterings involving the full 2D Fermi surface were taken into account with the work of Zanchi and Schulz, who studied the RG flows using a 32-patch discretization of the 2D Fermi surface for $t' = 0$ [Zanchi and Schulz 2000]. These calculations found two different regimes, one dominated by the AF correlations and the other by the $d_{x^2-y^2}$ pairing. The 2D RG calculations were also extended to the $t' \neq 0$ case [Halboth and Metzner 2000]. In the calculations for $t' \neq 0$ by Honerkamp *et al.*, an intermediate regime is found between the two regimes dominated by the AF correlations and $d_{x^2-y^2}$ pairing [Honerkamp *et al.* 2001]. In this intermediate regime, there are competing AF and $d_{x^2-y^2}$ superconducting correlations. This regime exists only for sizeable $t' < 0$ and it exhibits features which are similar to those seen in the pseudogap regime of the cuprates, which will be discussed in the following section. Honerkamp *et al.* extracted a temperature versus doping phase diagram from the 2D RG flows for the 2D Hubbard model with $t' < 0$, which is similar to that of the cuprates.

In spite of these interesting results it has to be kept in mind that the dynamical correlation length in DCA is cut-off by the size of the cluster and the one-loop RG is a weak-coupling approach. In addition, in RG calculations the single-particle self-energy corrections are not included at the one-loop level. In Section 8.1, it was seen that the single-particle self-energy corrections could play an important role in determining the strength of pairing. It should also be noted that, while the RG finds that the regime with $t' < 0$ is favored, in the DCA calculations the mean-field $T_c$'s are higher for $t' > 0$. These are some of the reasons for why exact results are necessary in order to reach a final conclusion.

## 8.4 Low-doping regime of the 2D Hubbard model

In the normal state of the underdoped cuprates, a pseudogap is seen in the excitation spectrum below a temperature $T^*$ which depends on the doping. The nature of the pseudogap is an important problem in this field and there exist a wide range of ideas about its origin and its implications [M$^2$S-HTSC VI proceedings 2000]. In this section, various calculations which have been carried out for exploring whether there is a pseudogap regime in the 2D Hubbard model will be discussed. In Ref. [Jaklic and Prelovsek 2000], a review of the numerical calculations on the $t$-$J$ model at finite temperatures is given and the results of these calculations are compared with the anomalous normal-state properties of the cuprates including the pseudogap.

The normal state pseudogap, while exhibiting dependence on the material properties, is seen in the uniform magnetic susceptibility, the low-frequency optical conductivity, the ARPES spectrum and various other measurements of the electronic properties. An interesting feature of the normal state pseudogap observed in the ARPES spectrum is that it is anisotropic on the Fermi surface: the pseudogap has maximum amplitude near the $(\pi, 0)$ and $(0, \pi)$ points of the Brillouin zone and it is minimum for wave vectors near $(\pi/2, \pi/2)$ [Ding *et al.* 1996, Ronning *et al.* 1998].

Kampf and Schrieffer first discussed the possibility of a pseudogap within the spin-bag approach for the 2D Hubbard model [Kampf and Schrieffer 1990a and 1990b]. They showed how a pseudogap could develop because of the AF fluctuations already at the one-loop level for the single-particle self-energy as the AF instability is approached. In the FLEX calculations, it was also found that a pseudogap opens in the density of states when the strength of the short-range AF fluctuations increases [Dahm and Tewordt 1995].

In spite of the sign problem, there are QMC data on $A(\mathbf{p}, \omega)$ at temperatures as low as $0.25t$ in the underdoped regime [Preuss *et al.* 1997]. These data show indications that a pseudogap opens in $A(\mathbf{p}, \omega)$ as $T$ decreases. In particular, for $\langle n \rangle \simeq 0.95$, it is seen that spectral weight above the Fermi level for $\mathbf{p}$ between $(\pi, 0)$ and $(\pi, \pi)$ decreases gradually as $T$ decreases from $0.5t$ to $0.25t$. In these calculations, the pseudogap has been attributed to the AF spin correlations, which are becoming larger than a lattice spacing for $T < 0.3t$ in the underdoped regime. However, in order to be able to make direct comparisons with the experimental data on the pseudogap, it would be necessary to reach temperatures below $0.1t$.

In recent one-loop RG calculations for the Hubbard model with $t' < 0$, a saddle-point regime is found between the AF ordered and the $d_{x^2-y^2}$ superconducting regimes [Honerkamp *et al.* 2001]. This regime exhibits features similar to those seen in the pseudogap regime of the cuprates. Here, the uniform magnetic and charge susceptibilities flow to zero because of the pairing and the umklapp-scattering processes, respectively. The possible existence of an umklapp-gapped spin-liquid phase was suggested in earlier RG calculations where a two-patch discretization of the Brillouin zone was used [Furukawa *et al.* 1998]. The similarity of this regime to the spin-gapped phase in the 2-leg Hubbard ladder was also noted. Because of the umklapp scatterings, in this regime, the sections of the Fermi surface which are near the $(\pi, 0)$ and $(0, \pi)$ points are truncated while at wave vectors near $(\pi/2, \pi/2)$ gapless single-particle excitations remain. Clearly, these results are useful for interpreting a number of experimental data on the underdoped cuprates and, in particular, the ARPES data.

The DCA calculations have also found interesting results about this subject [Huscroft *et al.* 2001]. Using this method, the low-doping and the low-temperature regime of the 2D Hubbard model was studied. Here, QMC simulations were used to solve the embedded lattice problem with $N_c = 8$. It was found that, as $T$ is lowered, an anisotropic pseudogap develops in $A(\mathbf{p}, \omega)$ and, in addition, the uniform magnetic susceptibility $\chi(T)$ gets suppressed. In particular, for $\langle n \rangle = 0.95$, $U = 6t$ and $T = 0.06t$, a pseudogap is found in $A(\mathbf{p}, \omega)$ for $\mathbf{p} = (\pi, 0)$ and $(0, \pi)$ and not for $(\pi/2, \pi/2)$. For these values of $U/t$ and $\langle n \rangle$, a mean-field $d_{x^2-y^2}$ superconducting transition temperature of $T_c \simeq 0.04t$ is obtained with the DCA. In addition, a sharp drop in $\chi(T)$ is observed near the temperature where the pseudogap in $A(\mathbf{p}, \omega)$ opens. In these calculations, the downturn in $\chi(T)$ has been attributed to the development of the AF correlations.

These results support the idea that perhaps the normal state pseudogap seen in the cuprates could be understood within a 2D Hubbard framework. However, there still exist a wide range of ideas about the origin of the pseudogap, and it is one of the important unresolved issues in this field.

## 8.5 Comparisons with the t-J model

In the large $U/t$ limit, the Hubbard model reduces to [Hirsch 1985]

$$H = -t \sum_{\langle i,j \rangle, \sigma} (c_{i,\sigma}^\dagger c_{j,\sigma} + c_{j,\sigma}^\dagger c_{i,\sigma}) + J \sum_{\langle i,j \rangle} (\mathbf{S_i} \cdot \mathbf{S_j} - \frac{1}{4} n_i n_j)$$

$$-\frac{J}{4} \sum_{i,\sigma} \sum_{\delta \neq \delta'} (c_{i+\delta,\sigma}^\dagger c_{i,-\sigma}^\dagger c_{i,-\sigma} c_{i+\delta',\sigma} - c_{i+\delta,-\sigma}^\dagger c_{i,\sigma}^\dagger c_{i,-\sigma} c_{i+\delta',\sigma}), \tag{8.5}$$

where $J = 4t^2/U$, and the double occupancy of a site is not allowed. In Eq. (8.5), $i + \delta$ and $i + \delta'$ sum over the nearest neighbors of site $i$. The last sum in this expression, which involves operators acting at three different sites, is dropped and what is remaining is called the t-J model. Clearly, the t-J and the Hubbard models have differences. The numerical studies of the t-J model have produced valuable information about the magnetic, density and the superconducting correlations in this system. Reviews of these studies can be found in Refs. [Dagotto 1994, Jaklic and Prelovsek 2000]. In this section, the density and the pairing correlations in the t-J and the Hubbard models will be compared.

In Section 8.5.1, the results on the phase separation and the density correlations in the 2D t-J model obtained with various numerical techniques will be discussed. These data will be compared with the CPMC and the DMRG calculations for the $12 \times 3$ Hubbard lattice. In Section 8.5.2, the nature of the pairing correlations seen in the 2D t-J model will be compared with those in the 2D Hubbard model. The results on the 2-leg t-J and Hubbard ladders will be compared in Section 8.5.3.

### 8.5.1 Comparisons with the density correlations in the 2D t-J model

The QMC simulations [Moreo and Scalapino 1991] and the exact-diagonalization [Dagotto *et al.* 1992b] calculations on the 2D Hubbard model did not find any indication of phase separation of the system into hole-rich and hole-poor regions. The 2-leg Hubbard ladder does not show any evidence for phase separation either [Noack *et al.* 1994]. In contrast to the Hubbard model, the 2D t-J model phase separates at any electron filling for sufficiently large values of the interaction strength $J/t$. Various techniques including the variational and the exact-diagonalization calculations [Emery *et al.* 1990], the high-temperature series expansions [Putikka *et al.* 1992], and the exact-diagonalization calculations [Dagotto 1994] were used for studying phase separation in the t-J model. Recently, the Green's function Monte Carlo (GFMC) [Hellberg and Manousakis 1997, 1999 and 2000, Calandra *et al.* 1998] and the DMRG [White and Scalapino 1998a, Rommer *et al.* 2000] were used for obtaining the phase-separation boundary in the t-J model. Currently, where the true phase-separation boundary lies is controversial, since the approaches noted above arrive at different conclusions.

Emery *et al.* suggested that the 2D t-J model phase separates at all interaction strengths [Emery *et al.* 1990]. Subsequent calculations found that the phase separation occurs only for $J \gtrsim t$, as indicated by the solid curve in Fig. 8.7 [Putikka *et al.* 1992]. However, recently, the GFMC calculations [Calandra *et al.* 1998] suggested that the phase-separation boundary might occur at lower $J/t$ values near half-filling. This is indicated by the empty circles in Fig. 8.7. In these calculations, next to the phase-separation boundary lies the regime where the doped holes form $d_{x^2-y^2}$-wave pairs. The recent GFMC calculations by Hellberg and Manousakis, on the other hand, find that the critical value of $J/t$ for phase separation extrapolates to zero at low dopings as shown by the dashed curve in Fig. 8.7 [Hellberg and Manousakis 1997, 1999 and 2000]. In these
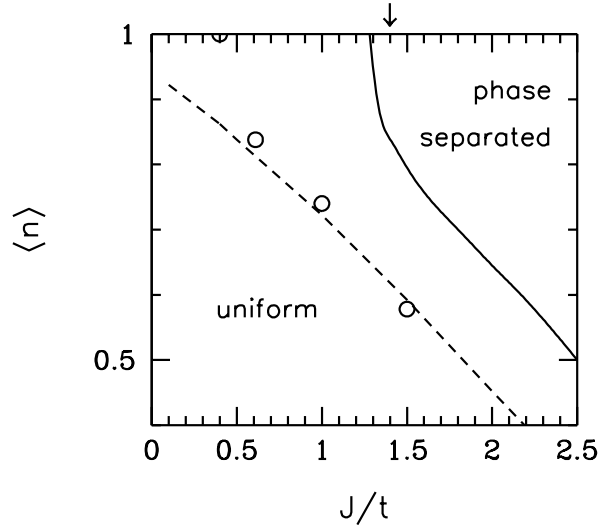
Figure 8.7: Sketch of the phase-separation boundary for the 2D $t$-$J$ model obtained from various calculations. The solid line represents the phase-separation boundary obtained by the high-temperature series expansion [Putikka *et al.* 1992]. The open circles represent the results of the GFMC calculations from Ref. [Calandra *et al.* 1998]. The dashed line is from Ref. [Hellberg and Manousakis 1997], which was also obtained by the GFMC. The arrow indicates the DMRG result for the critical value of $J/t$ for phase separation on a six-leg $t$-$J$ ladder in the limit of zero doping [Rommer *et al.* 2000].

calculations, the $t$-$J$ model phase separates in the parameter regime appropriate for the cuprates. For instance, at 15% hole doping the critical value of $J/t$ is about 0.4. The DMRG calculations find that, in the physically relevant regime, the ground state of the $t$-$J$ model is striped and not phase separated [White and Scalapino 1998a, 2000]. The DMRG calculations are carried out on large lattices with periodic boundary conditions at the long edges and open boundary conditions at the short edges. In these calculations the phase separation occurs for $J > t$. For instance, in the six-leg Hubbard ladder, the critical value of $J/t$ is $\sim 1.4$ as the doping approaches zero, which is indicated by the arrow in Fig. 8.7.

The stripes observed in the DMRG calculations are a domain wall of holes across which there is a $\pi$-phase shift in the AF background. According to the DMRG calculations, the stripe formation represents an instability of the system where pairs of bound holes combine to form domain walls. In particular, through the stripe correlations the system reduces the frustration of the AF background and lowers the kinetic energy of the holes. However, the issue of the phase separation versus the stripe formation in the 2D $t$-$J$ model remains controversial. The role of the open boundary conditions in producing the static stripes was questioned [Hellberg and Manousakis 2000], and the need to have more than one pair of holes in order to see the stripe correlations was noted [White and Scalapino 2000]. The calculation of the dynamical spin and charge susceptibilities for sufficiently large $t$-$J$ systems would resolve these issues.

The possibility of stripe formation in strongly correlated systems were noted in mean-field calculations of the 2D Hubbard model soon after the discovery of the cuprates [Zaanen and Gunnarson 1989, Poilblanc and Rice 1989, Schulz 1989, Machida 1989]. There has been a surge of interest

in this field since the observation of static stripe ordering in the neutron scattering experiments on $La_{1.6-x}Nd_{0.4}Sr_xCuO_4$ [Tranquada *et al.* 1995]. Beyond mean-field, the nature of the stripe correlations in the Hubbard model were studied with the DMRG and the CPMC techniques for the 3-leg Hubbard ladder [Bonca *et al.* 2000]. The findings of these calculations are important and they will be briefly described here.

The CPMC is an approximate method which projects the ground state from a trial state as has been discussed in Section 8.2. Both the DMRG and the CPMC calculations find that for $U \gtrsim 6t$ there are static stripes in the ground state of a $12 \times 3$ Hubbard lattice doped with six holes when open boundary conditions are used. In Figures 8.8 and 8.9, the rung magnetization

$$S^z(i) = \sum_{j=1}^{3} \langle S^z(i,j) \rangle \tag{8.6}$$

and the rung hole density

$$\rho(i) = \sum_{j=1}^{3} \langle \rho(i,j) \rangle \tag{8.7}$$

are plotted as a function of the rung location $i$ at $U = 8t$. Here, $S^z(i,j)$ and $\rho(i,j)$ are the spin and hole-density operators at the $j$'th site of the $i$'th rung. In Fig. 8.8, it is seen that between rungs 3 and 4 the spins are ferromagnetically coupled, causing a $\pi$-phase shift, and the magnetisation density is small. The same occurs at rungs 9 and 10. In Fig. 8.9, it is seen that at these sites the holes form domain walls. In these figures the results of the unrestricted Hartree-Fock (UHF) calculations are also shown. The UHF approximation produces results in agreement with the CPMC and the DMRG calculations when the reduced value of $U = 3t$ is used. This behavior is similar in spirit to using a reduced Coulomb repulsion within RPA for the spin susceptibility as discussed in Section 3.3. It is important to note that the structure of the stripes seen in these calculations for $U \gtrsim 6t$ is quite similar to those found in the three-leg $t$-$J$ ladder [White and Scalapino 1998b]. However, for $U < 6t$ these features disappear and no evidence is found for static stripes in the ground state. In this regime, only some evidence for low-lying states with stripes are found. At weak $U/t$, the density of virtual holes due to the double occupancy increases, and, it has been noted that this might weaken the stripe correlations. At this point, it is of interest to explore whether there is a relation between the stripe patterns which are observed within the presence of the open boundary conditions and any possible "$4\mathbf{k}_F$" CDW correlations. It should also be noted that the CPMC method does not show evidence for stripe correlations even at large $U/t$ when the free-electron trial wave function is used instead of the UHF wave function. Hence, caution is necessary in choosing a trial wave function which is suitable for the ground state.

These results were found using open boundary conditions. The DMRG calculations are not carried out with periodic boundary conditions, but the CPMC calculations can be. When carried out with the periodic boundary conditions on square lattices, the CPMC calculations do not find stripes in the hole and spin densities and in the hole and spin correlation functions. This indicates that the static stripe pattern seen in the ground state results from the open boundary conditions breaking the translational symmetry. With the periodic boundary conditions, there might be low-lying states with stripe patterns but it might be difficult to detect them numerically. Hence, whether static stripes exist in the ground state of the 2D Hubbard model with periodic boundary conditions remains as an important open question. Here and in Section 4, it has been seen that there are similarities in the density correlations of the $t$-$J$ model and the Hubbard model with large $U/t$. But, there are differences as well.
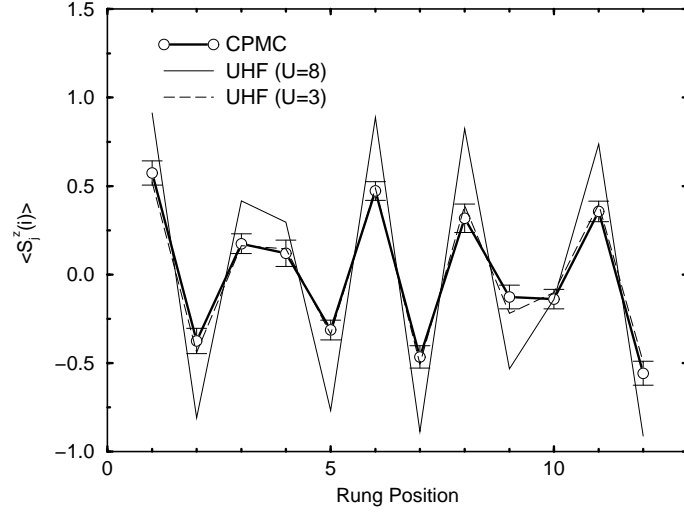
Figure 8.8: Rung-magnetisation versus the rung location for the $12 \times 3$ Hubbard lattice doped with six holes. From [Bonca *et al.* 2000].
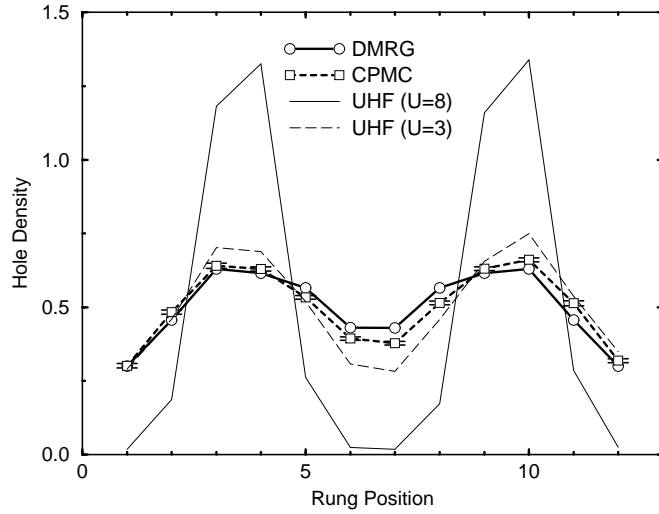


Figure 8.9: Rung-hole density versus the rung location for the $12 \times 3$ Hubbard lattice doped with six holes. From [Bonca *et al.* 2000].

### 8.5.2  Comparisons with the superconducting correlations in the 2D $t$-$J$ model

When two-holes are doped into the half-filled $t$-$J$ model, they form a $d_{x^2-y^2}$-wave bound pair for interaction strengths relevant to the high-$T_c$ cuprates, $J/t \sim 0.35$ [Poilblanc 1993, Dagotto 1994]. However, much controversy exists over what happens when more than one pair of holes is doped. The GFMC calculations by Calandra *et al.* find that they form a $d_{x^2-y^2}$-wave superconducting ground state for $J/t \sim 0.35$ and dopings relevant to the high-$T_c$ cuprates [Calandra *et al.* 1998]. However, the GFMC calculations by Hellberg and Manousakis find that this parameter regime lies right at the boundary for the phase separation of holes [Hellberg and Manousakis 1997 and 1999].

The DMRG calculations find that in the same regime the ground state has static stripes, and the system does not have $d_{x^2-y^2}$-wave superconducting long-range order [White and Scalapino 1998a, 1999]. The fact that the static stripes compete with the superconductivity is an important result of these calculations. However, when the static stripe patterns are broken by a second-near-neighbor hopping $t' > 0$, it is seen that the system develops long-range $d_{x^2-y^2}$-wave superconducting order, and in this regime the low-lying stripe correlations coexist with the long-range superconducting order.

Both the $t$-$J$ and the Hubbard models exhibit $d_{x^2-y^2}$-wave pairing correlations due to the AF spin fluctuations. However, there are differences between these models, one of them being the no-double-occupancy constraint in the $t$-$J$ model. It is possible that this constraint is more favorable of the stripe correlations and, because of this, the one-band Hubbard or a three-band $CuO_2$ model might have weaker tendency for stripe formation than the $t$-$J$ model [Daul *et al.* 2000, Jeckelmann *et al.* 1998].

Whether the doped 2D Hubbard model develops static stripe patterns in the ground state is an important issue. In the previous section, we have seen from the QMC data that the doped 2D Hubbard model has $d_{x^2-y^2}$-wave pairing correlations which develop as the temperature is lowered and they are not weak correlations. However, if indeed a static striped phase is more favored in the ground state then this could suppress the growth of the superconducting correlations at a temperature lower than where the QMC simulations are carried out. In this respect, the comparison of the CPMC and the DMRG calculations for the $12 \times 3$ Hubbard lattice are useful [Bonca *et al.* 2000]. However, further study is necessary before reaching conclusions about the ground state of the doped 2D Hubbard model.

The results shown here emphasize the interplay of the magnetic, density and the pairing correlations in the Hubbard and $t$-$J$ models. In the cuprates, the substitution of nonmagnetic impurities gives useful information about the interplay of these correlations in these materials. It is known that, when substituted in place of planar Cu, nonmagnetic impurities strongly suppress the superconducting $T_c$ [Xiao *et al.* 1990] and locally enhance the AF correlations [Mahajan *et al.* 1994 and 2000]. To the extend that a nonmagnetic impurity can be considered as a pure potential scatterer, these experimental data give information about the magnetic and pairing response of these materials when perturbed in the density channel.

### 8.5.3  Comparisons with the 2-leg $t$-$J$ ladder

The Lanczos calculations on the 2-leg $t$-$J$ ladder showed that this system, which has a spin gap in the insulating state, can exhibit superconducting correlations upon doping [Dagotto *et al.* 1992a]. The mean-field calculations noted the $d_{x^2-y^2}$-like structure of the superconducting pairs in the $t$-$J$ ladder [Gopalan *et al.* 1994]. The DMRG calculations on long $t$-$J$ ladders established that in the ground state there are power-law decaying superconducting correlations [Hayward *et al.* 1995]. In Ref. [Dagotto and Rice 1996], the properties of $n$-leg spin-1/2 ladders are reviewed and comparisons

are made with various ladder compounds.

There are differences in the nature of the $d_{x^2-y^2}$-like superconducting correlations seen in the $t$-$J$ and the Hubbard ladders. For instance, in the Hubbard ladder for $t_\perp/t \sim 1.0$, the superconducting correlations are weak, and the pair-field correlation function $D(\ell)$ decays as $\ell^{-2}$, which is like the $U = 0$ case [Noack *et al.* 1994]. Only when the distribution of the single-particle spectral weight is such that it can make use of the momentum structure in $\Gamma_I$, does the system exhibit strong pairing correlations. On the other hand, in the isotropic $t$-$J$ ladder, the system has strong pairing correlations. For instance, $D(\ell)$ decays approximately as $\ell^{-1}$ for $\langle n \rangle = 0.8$ and $J/t = 1$ [Hayward *et al.* 1995]. In addition, Schulz has shown that $D(\ell)$ decays as $\ell^{-1/2}$ in the limit $\langle n \rangle \to 1$ [Schulz 1999]. Hence, for isotropic hopping the $t$-$J$ ladder has stronger pairing correlations compared to the Hubbard ladder. Probably, this is related to the fact that in the $t$-$J$ model the exchange term $J$, which is an effective attractive interaction between the nearest-neighbor antiparallel spins, is introduced by hand. On the other hand, in the Hubbard model, the effective attractive interaction which is responsible for the pairing is generated by the onsite Coulomb repulsion through higher-order many-body processes only when the system has the suitable conditions.

## 8.6   Implications for $d_{x^2-y^2}$-wave pairing in the cuprates

The presence of $d_{x^2-y^2}$ pairing correlations in the Hubbard model and the nature of the effective interaction mediating it are issues which are of interest for studying high temperature superconductivity in the cuprates. This is so especially after it became clear that the superconducting gap function in the high $T_c$ cuprates is of the $d_{x^2-y^2}$-wave type. Within this context, enormous amount of research has been carried out on this model.

In this article, the numerical studies of $d_{x^2-y^2}$-wave pairing in the Hubbard model have been reviewed. The Monte Carlo simulations have shown the presence of the $d_{x^2-y^2}$-wave pairing correlations in the Hubbard model, even though sufficiently low temperatures, where long-range order could establish, have not been reached. For $U/t = 4$ and at the temperatures where the simulations are carried out, the values of the $d_{x^2-y^2}$-wave eigenvalues of the particle-particle Bethe-Salpeter equation are in agreement with the FLEX calculations. When carried out at low temperatures, the FLEX calculations find $T_c$'s of order $0.025t$. Since $t$ is estimated to be about 0.45 eV for a single-band model of the cuprates [Hybertson *et al.* 1990], this value of the $T_c$ corresponds to $\sim 130$ K. This is a high value reflecting the electronic energy scales of the model. Furthermore, the comparison of the FLEX and the QMC data suggests that the pairing could be stronger for $U = 8t$. However, these are only mean-field estimates for a possible Kosterlitz-Thouless transition and, in fact, the ground state of the doped 2D Hubbard model is not known. It might be that an additional parameter needs to be tuned in order to create optimum conditions for $d_{x^2-y^2}$-wave superconductivity in two dimensions. For instance, in the 2-leg ladder case, it was necessary to tune $t_\perp/t$. In this respect, the second-nearest-neighbour hopping $t'$ may play a role for the enhancement of the $d_{x^2-y^2}$ pairing in the 2D system like $t_\perp$ does for the 2-leg ladder. It is also possible that a three-band $CuO_2$ model with an onsite Coulomb repulsion at the Cu sites offers additional degrees of freedom for creating more favourable conditions for pairing.

The QMC results reviewed here show that the short-range AF correlations are responsible for the $d_{x^2-y^2}$ pairing correlations in the 2D Hubbard model. These results also suggest that effects which enhance the magnitude of $\Gamma_{Is}(\mathbf{q} \sim (\pi, \pi), i\omega_m = 0)$ and the single-particle spectral weight near the $(\pi, 0)$ and the $(0, \pi)$ points of the Brillouin zone act to enhance the $d_{x^2-y^2}$-wave superconducting correlations. Clearly, other effects which enhance $d_{x^2-y^2}$-wave pairing can exist. Exploring these possibilities is an active research field.

# 9 Summary and conclusions

In this paper, the numerical studies of the 2D and the 2-leg Hubbard models have been reviewed. For the 2D Hubbard model, data from the QMC simulations have been shown. These data represent what has been obtained over the years in the parameter regime allowed by the sign problem. For the 2-leg Hubbard ladder, the QMC results at finite temperatures and the DMRG data on the ground state have been shown.

Here, the emphasis has been placed on the $d_{x^2-y^2}$-wave superconducting correlations observed in the Hubbard model. In order to develop an understanding of the origin of these correlations, results on the spin, charge and the single-particle excitations have been shown along with the data on the particle-particle and the particle-hole interactions. The observation of the short-range AF fluctuations by the NMR and the neutron scattering experiments, and the unusual single-particle spectrum seen in the ARPES data are properties which support using a Hubbard framework for studying the pairing correlations of the cuprates.

In the 2D Hubbard model, upon hole doping the long-range AF order is destroyed and the system exhibits short-range AF correlations. The maximum-entropy analysis of the QMC data shows that the AF and the Coulomb correlations strongly affect the single-particle properties. In particular, it has been seen that, as the strength of $U/t$ increases, significant amount of single-particle weight remains pinned near the Fermi level at the $(\pi, 0)$ and $(0, \pi)$ points of the Brillouin zone. These generate phase space for scatterings in the $d_{x^2-y^2}$-wave BCS channel. The results on the particle-particle and the particle-hole irreducible interactions have been also presented. It has been seen that, for $U = 4t$, a properly-renormalized single spin-fluctuation exchange interaction can describe the momentum, the Matsubara-frequency and the temperature dependence of the effective-particle-particle interaction. This means that, for these values of $U/t$ and $T/t$, the attraction in the $d_{x^2-y^2}$ channel is mediated by the AF spin fluctuations.

The DMRG results on the 2-leg ladder, which have been presented in Section 7 are important. These calculations represent the first example where a purely repulsive onsite interaction leads to superconducting correlations which are enhanced over the noninteracting ($U = 0$) case in the ground state of a bulk system. For certain values of $t_\perp/t$ and in the intermediate coupling regime, this model exhibits enhanced power-law $d_{x^2-y^2}$-like superconducting correlations. The QMC simulations for this system show that the effective particle-particle interaction $\Gamma_I$ peaks at $(\pi, \pi)$ momentum transfer and, in addition, the $d_{x^2-y^2}$ pairing correlations are strongest when there is significant amount of single-particle spectral weight near the Fermi level at the $(\pi, 0)$ and $(0, \pi)$ points in the Brillouin zone. This way the system makes optimum use of the momentum structure in $\Gamma_I$ for $d_{x^2-y^2}$-wave pairing.

These data were also compared with various other approaches to the Hubbard model, such as the diagrammatic FLEX approximation, the variational and the projector Monte Carlo simulations, the dynamical cluster approximation and the one-loop RG calculations. In addition, the similarities and the differences with the $t$-$J$ model were briefly discussed. The implications for the $d_{x^2-y^2}$-wave superconductivity seen in the cuprates were also noted.

It is difficult to reach conclusions about the strongly correlated systems. Nevertheless, here, the following conclusions are given:

(1) An onsite Coulomb repulsion can lead to superconducting correlations which are enhanced with respect to the noninteracting ($U = 0$) case in the ground state of a bulk system. This is proven for the case of the 2-leg Hubbard ladder.

(2) The 2D Hubbard model exhibits $d_{x^2-y^2}$-wave pairing correlations which grow as the temperature is lowered in the parameter regime where the QMC simulations are carried out. The fastest

growing pairing correlations occur in the singlet $d_{x^2-y^2}$-wave channel. These correlations are not weak.

(3) The QMC simulations also find that the effective pairing interaction in the 2D and the 2-leg Hubbard models in the intermediate coupling regime and at temperatures greater or of order $J/2$ is consistent with the spin-fluctuation exchange approximation.

(4) Two factors which create optimum conditions for $d_{x^2-y^2}$ pairing in the Hubbard model are enhanced single-particle spectral weight at the Fermi level near the $(\pi, 0)$ and $(0, \pi)$ points in the Brillouin zone and large weight in the effective pairing interaction $\Gamma_I$ at large momentum transfers. Clearly, there can be other ways of enhancing the $d_{x^2-y^2}$ pairing correlations.

### Acknowledgments

Most of the numerical data presented here are from various calculations carried out with T. Dahm, R.M. Noack, D.J. Scalapino and S.R. White. The QMC data shown here were obtained at the San Diego Supercomputer Center.

## 10   Appendix

The results shown in Sections 3 through 7 of this review were obtained with the determinantal QMC and the DMRG techniques. Here, these two approaches to the many-body problem will be described briefly.

### 10.1   Determinantal QMC technique

The determinantal QMC algorithm used in obtaining the QMC data shown here is described in Ref. [White *et al.* 1989b]. Reviews of this technique can be found in Refs. [Scalapino 1993, Muramatsu 1999]. The basic idea of this approach is due to Blankenbecler, Scalapino and Sugar [Blankenbecler *et al.* 1981]. Here, the purpose is to calculate the expectation value of an operator $O$ at finite temperature $T$ in the grand canonical ensemble,

$$\langle O \rangle = \frac{1}{Z} \text{Tr}\, O e^{-\beta H} \tag{10.1}$$

where

$$Z = \text{Tr}\, e^{-\beta H}. \tag{10.2}$$

It is convenient to take the Hubbard hamiltonian as $H = K + V$ where

$$K = -t \sum_{\langle ij \rangle, \sigma} (c_{i\sigma}^\dagger c_{j\sigma} + h.c.) - \mu \sum_i (n_{i\uparrow} + n_{i\downarrow}) \tag{10.3}$$

and

$$V = U \sum_i (n_{i\uparrow} - \frac{1}{2})(n_{i\downarrow} - \frac{1}{2}). \tag{10.4}$$

After discretizing the inverse temperature into $L$ time slices, $\beta = L\Delta\tau$, the Trotter approximation is used to rewrite the partition function as

$$Z = \text{Tr}\, e^{-L\Delta\tau H} \cong \text{Tr}\, (e^{-\Delta\tau V} e^{-\Delta\tau K})^L. \tag{10.5}$$

Next, the interaction term $V$, which is quartic in the fermion operators, is reduced to a bilinear form with the Hubbard-Stratonovich transformation

$$e^{-\Delta\tau U(n_{i\uparrow}-1/2)(n_{i\downarrow}-1/2)} = \frac{e^{-\Delta\tau U/4}}{2} \sum_{S_{i\ell}=\pm 1} e^{-\Delta\tau S_{i\ell}\lambda(n_{i\uparrow}-n_{i\downarrow})} \tag{10.6}$$

where $\cosh(\lambda\Delta\tau) = \exp(U\Delta\tau/2)$. Here, at each lattice site $i$ and for each time slice $\ell$, an Ising spin $S_{i\ell} = \pm 1$ is used for the decoupling. This form of the Hubbard-Stratonovich decoupling was introduced by Hirsch [Hirsch 1985]. After integrating out the fermion degrees of freedom, the partition function is given by

$$Z = \sum_{\{S_{i\ell}\}} \det M^{\uparrow}(\{S_{i\ell}\}) \det M^{\downarrow}(\{S_{i\ell}\}) \tag{10.7}$$

where

$$M^{\sigma}(\{S_{i\ell}\}) = I + B_L^{\sigma} B_{L-1}^{\sigma} ... B_1^{\sigma} \tag{10.8}$$

and

$$B_{\ell}^{\sigma} = e^{-\sigma\Delta\tau\nu(\ell)} e^{-\Delta\tau k} \tag{10.9}$$

with electron spin $\sigma = \pm 1$. Here, the summation is over all configurations $\{S_{i\ell}\}$ of the Ising fields, $I$ is the $N \times N$ unit matrix, $B_{\ell}^{\sigma}$'s are $N \times N$ matrices where $\nu(\ell)_{ij} = \delta_{ij}S_{i\ell}$ and $k$ is the matrix representation of the kinetic energy operator, Eq. (10.3). Similar expressions can be obtained for the expectation value $\langle O \rangle$. For instance, the equal-time single-particle correlation function $\langle c_{j\sigma}c_{j'\sigma}^{\dagger} \rangle$ can be expressed as

$$\langle c_{j\sigma}c_{j'\sigma}^{\dagger} \rangle = \frac{1}{Z} \sum_{\{S_{i\ell}\}} G_{\sigma}(j,j';\{S_{i\ell}\}) \det M^{\uparrow}(\{S_{i\ell}\}) \det M^{\downarrow}(\{S_{i\ell}\}) \tag{10.10}$$

where

$$G_{\sigma}(j,j';\{S_{i\ell}\}) = \left[ (I + B_L^{\sigma} B_{L-1}^{\sigma} ... B_1^{\sigma})^{-1} \right]_{jj'}. \tag{10.11}$$

The summation over the Ising spin variables in Eq. (10.10) is evaluated using Monte Carlo sampling techniques. In this way, Eq. (10.10) becomes

$$\langle c_{j\sigma}c_{j'\sigma}^{\dagger} \rangle = \langle G_{\sigma}(j,j';\{S_{i\ell}\}) \rangle_P \tag{10.12}$$

where $\langle ... \rangle_P$ is evaluated by averaging over spin configurations $\{S_{i\ell}\}$ generated with the probability distribution

$$P(\{S_{i\ell}\}) = \frac{1}{Z} \det M^{\uparrow}(\{S_{i\ell}\}) \det M^{\downarrow}(\{S_{i\ell}\}). \tag{10.13}$$

Similarly, the time-dependent single-particle Green's function $\langle c_{j\sigma}(\tau)c_{j'\sigma}(\tau') \rangle$ is calculated by averaging $G_{\sigma}(j,\tau;j',\tau';\{S_{i\ell}\})$, which can also be expressed in terms of $B_{\ell}^{\sigma}$'s.

The Hubbard-Stratonovich transformation maps the interacting fermion problem on the 2D lattice to that of non-interacting fermions in a random Ising field on a 3D lattice, the third dimension being the imaginary time axis $\tau$. At this stage, for a given spin configuration $\{S_{i\ell}\}$, the Wick's theorem applies to the higher order correlation functions. Hence, the higher-order correlation functions can be obtained by averaging over the products of the single-particle propagators in random Ising fields. For instance, the two-particle correlation function

$$\langle T\, c_{\uparrow}(i_4,\tau_4)c_{\downarrow}(i_3,\tau_3)c_{\downarrow}^{\dagger}(i_2,\tau_2)c_{\uparrow}^{\dagger}(i_1,\tau_1) \rangle, \tag{10.14}$$

which is used in extracting the particle-particle reducible interaction $\Gamma$ in Section 6, can be obtained from

$$\langle G_\uparrow(i_4, \tau_4; i_1, \tau_1; \{S_{i\ell}\}) G_\downarrow(i_3, \tau_3; i_2, \tau_2; \{S_{i\ell}\})\rangle_P. \tag{10.15}$$

For $\langle n \rangle = 1$, the product of the fermion determinants, $\det M^\uparrow(\{S_{i\ell}\}) \det M^\downarrow(\{S_{i\ell}\})$, is positive. However, away from half-filling and for $U > 0$, this product is not positive for all configurations $\{S_{i\ell}\}$. In this case, one can use the probability distribution

$$\tilde{P}(\{S_{i\ell}\}) = \frac{|\det M^\uparrow(\{S_{i\ell}\}) \det M^\downarrow(\{S_{i\ell}\})|}{\sum_{\{S_{i\ell}\}} |\det M^\uparrow(\{S_{i\ell}\}) \det M^\downarrow(\{S_{i\ell}\})|}, \tag{10.16}$$

in order to calculate the expectation value $\langle O \rangle$ with

$$\langle O \rangle = \frac{\langle O(\{S_{i\ell}\})\mathrm{sign}(\{S_{i\ell}\})\rangle_{\tilde{P}}}{\langle \mathrm{sign}(\{S_{i\ell}\})\rangle_{\tilde{P}}}. \tag{10.17}$$

Here, $\mathrm{sign}(\{S_{i\ell}\})$ is the sign of $\det M^\uparrow(\{S_{i\ell}\}) \det M^\downarrow(\{S_{i\ell}\})$ and the average $\langle ... \rangle_{\tilde{P}}$ is calculated with the probability distribution $\tilde{P}$. The denominator in Eq. (10.17),

$$\langle \mathrm{sign} \rangle \equiv \langle \mathrm{sign}(\{S_{i\ell}\})\rangle_{\tilde{P}}, \tag{10.18}$$

becomes small when the number of configurations with positive signs is close to that with the negative signs. It has been shown that away from half-filling $\langle \mathrm{sign} \rangle$ decreases exponentially as $T$ decreases [Loh *et al.* 1990]. This causes large statistical errors in $\langle O \rangle$ and it is the cause of the sign problem. The temperature and the doping regime of the 2D Hubbard model which cannot be studied with QMC because of the sign problem is shown at the end of Section 6. In spite of the sign problem, useful information has been extracted from the 2D and the 2-leg Hubbard models with QMC simulations. Currently, the search for ways of removing the sign problem is an important field of study. Improvements in the sign problem which decreases the temperatures accessible to QMC simulations by even a factor of two would be valuable.

## 10.2 DMRG technique

The DMRG technique which was invented by White represents a significant development in the application of the renormalization group ideas to interacting lattice models [White 1992 and 1993]. Currently, it is the numerical method of choice for studying the ground state properties of quasi-1D interacting systems. The brief discussion of this technique given here follows closely that of Ref. [White 1993]. For simplicity, the following discussion will be for a 1D lattice.

One of the differences between the DMRG and the standard real-space RG approach is in the treatment of the boundary conditions in the basic blocking procedure. In the standard approach for a finite 1D system, the chain is broken into finite blocks $B_\ell$ of $\ell$ sites. Here, first the Hamiltonian for two identical blocks is diagonalized and then the lowest eigenstates are kept to form a new approximate Hamiltonian describing a larger block $B'_{2\ell}$ with $2\ell$ sites. This procedure is illustrated in Fig. 10.1(a). White and Noack have shown that this was of blocking introduces large errors for a model of a free particle on a 1D lattice because of the way the boundary conditions are treated during the blocking [White and Noack 1992]. In the standard RG scheme, neglecting the connection of the two blocks to the neighboring blocks corresponds to setting the wave function of the particle to 0 outside of the blocks. Consequently, the low lying states from the previous iteration cause a 'kink' in the wave function in the middle of the enlarged block $B'_{2\ell}$. Hence, in order to accurately
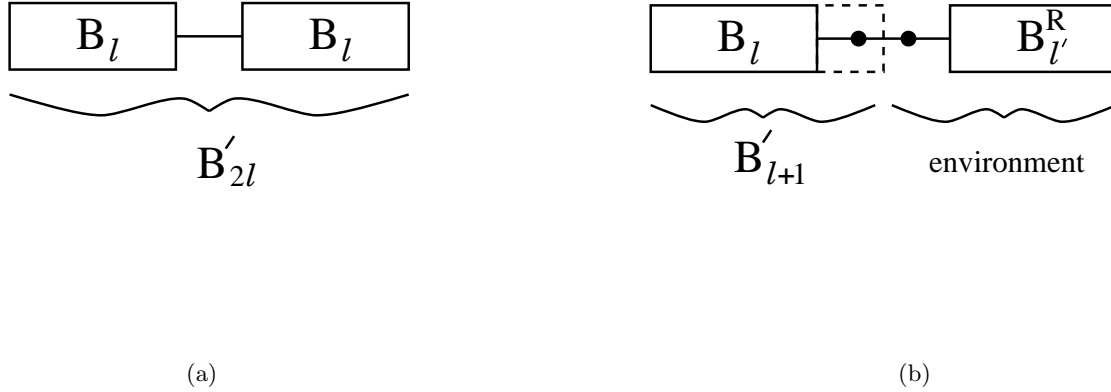
Figure 10.1: (a) Standard blocking scheme used for real-space RG for a 1D system. Here, the Hamiltonian for two blocks $B_\ell$ each with $\ell$ sites is diagonalized and truncated to form an approximate Hamiltonian for the new block $B'_{2\ell}$ with $2\ell$ sites. (b) DMRG blocking scheme for a finite 1D system using a superblock which is composed of blocks $B_\ell$ and $B^R_{\ell'}$, and two additional sites in between. Here, first the Hamiltonian for the superblock is diagonalized and the density matrix is formed for the enlarged block $B'_{\ell+1}$. The Hamiltonian for block $B'_{\ell+1}$ is then expressed in a reduced basis composed of the leading eigenstates of this density matrix. In the next iteration, the block $B'_{\ell+1}$ replaces $B_\ell$.

represent the states of block $B'_{2\ell}$, it is necessary to use almost all of the states of block $B_\ell$, and any truncation of these states introduces large errors in the RG process. White and Noack have noted that using a combination of boundary conditions during the blocking fixes this deficiency for a free particle on a 1D lattice. They have also shown that an alternative approach is to use a superblock which is composed of more than two blocks. In this way, two of the blocks in the superblock are used to form a larger block for the next iteration while the effect of the other blocks is to apply a variety of boundary conditions. The DMRG technique uses a superblock during the RG iteration, which is illustrated in Fig. 10.1(b) for a 1D lattice of $L$ sites. This superblock is composed of two blocks with $\ell$ and $\ell' = L - \ell - 2$ sites and two additional sites in the middle, which can be considered as additional blocks. The block $B_\ell$ and its neighboring lattice site are called the 'system', while the rest of the superblock is called the 'environment'. With each iteration, the system block gets enlarged by one lattice site.

Another novel feature of the DMRG technique is the use of the density matrices to choose the states which are to be kept during the iteration [White 1992 and 1993]. In the standard RG approach, the lowest $m$ eigenstates of the Hamiltonian for two blocks is used in forming the truncated Hamiltonian for the larger block, as illustrated in Fig. 10.1(a). This would be a reasonable approximation for a model where the coupling between the blocks is weak. However, for an interacting system such as the Hubbard model, each block is strongly coupled to its environment. In this case, White has shown that it is better to use during the truncation the eigenstates of the density matrix of the system, and, in fact, the optimal states to be kept are the eigenvectors of the density matrix of the system with the largest eigenvalues. The use of the superblock and the density matrix formulation are the important new ideas used by the DMRG technique.

At this point, the DMRG algorithm for a finite 1D lattice can be summarized as follows: (1) The first step is to diagonalize the Hamiltonian for the superblock, which is illustrated in Fig. 10.1(b), using exact diagonalization techniques in order to find the ground state $\psi_{ij}$. Here, the index $i$ refers to the system part of the lattice and $j$ refers to the environment. (2) Next, the reduced density matrix for block $B'_{\ell+1}$ is calculated by tracing over the environment,

$$\rho_{ii'} = \sum_j \psi_{ij} \psi^*_{i'j}, \tag{10.19}$$

and then $\rho$ is diagonalized. (3) At this stage, the Hamiltonian for $B'_{\ell+1}$ can be transformed to a reduced basis which consists of the $m$ leading eigenstates of $\rho$. Typically a few hundred eigenstates of $\rho$ are kept. (4) In the next iteration, this approximate Hamiltonian for $B'_{\ell+1}$ is used in place of the Hamiltonian for $B_\ell$.

With this procedure, the system block is built up by adding one lattice site at a time as the iteration continues form one end of the lattice to the other end. With each sweep through the lattice, a better approximation is obtained for the Hamiltonian of the block $B_\ell$. In addition, during the sweeps, the Hamiltonians of the system blocks from the previous sweep are used as the Hamiltonians for the environment blocks. For 1D lattices, reflections of $B_\ell$ can be used in place of $B^R_{\ell'}$ in order to build up the superblock to the proper size during the first sweep. In order to extend this algorithm to 2D, a row of neighboring sites can be added to the system block at each iteration, or a single site can be added using a connected 1D path through the 2D lattice. For higher dimensional lattices, an empty environment block $B^R_{\ell'}$ is used in the first sweep.

The DMRG technique is more accurate when the number of connections between the system and the environment blocks is minimized. Hence, usually open boundary conditions are employed. When periodic boundary conditions are used, the accuracy decreases. For 2D lattices, the accuracy of DMRG also decreases as a function of the width of the lattice. However, if a larger number of the eigenstates of $\rho$ are kept during the truncation, the accuracy of the algorithm increases. Finally, the DMRG is most accurate for large $U$ and least accurate for $U = 0$.

With this technique, various equal-time correlation functions for the 2-leg Hubbard ladder have been calculated on lattices up to $2 \times 32$ in size [Noack *et al.* 1996]. For the 3-leg Hubbard ladder there are DMRG data for a $3 \times 12$ lattice [Bonca *et al.* 2000]. For the *t-J* model, larger systems can be studied with this technique. In this case, 2D clusters up to $28 \times 8$ in size have been studied using cylindrical boundary conditions [White and Scalapino 1998a]. Currently, the DMRG technique is used in a wide variety of fields, and the efforts to develop new algorithms to study larger clusters continues. In addition, there is continuing work to extend the DMRG technique in order to calculate the dynamical correlation functions.

# 11 References

* E-mail: nbulut@ku.edu.tr

ABRAHAMS, E., BALATSKY, A., SCHRIEFFER, J. R., and ALLEN, P. B., 1993, *Phys. Rev. B*, **47**, 513.

ABRAHAMS, E., BALATSKY, A., SCALAPINO, D. J., and SCHRIEFFER, J. R., 1995, *Phys. Rev. B*, **52**, 1271.

AEBI, P., OSTERWALDER, J., SCHWALLER, P., SCHLAPBACH, L., SHIMODA, M., MOCHIKU, T., and KADOWAKI, K., 1994, *Phys. Rev. Lett.*, **72**, 2757.

ANDERSON, P. W., 1987, *Science*, **235**, 1196.

ANDERSON, P. W., 1997, *Adv. Phys.*, **46**, 3.

ANDERSON, P. W., BASKARAN, G., ZOU, Z., and HSU, T., 1987, *Phys. Rev. Lett.*, **58**, 2790.

ANDERSON, P. W., and ZOU, Z., 1988, *Phys. Rev. Lett.*, **60**, 132.

BALATSKY, A. V., and ABRAHAMS, E., 1992, *Phys. Rev. B*, **45**, 13125.

BALENTS, L., and FISHER, M. P. A., 1996, *Phys. Rev. B*, **53**, 12133.

BECCA, F., CAPONE, M., and SORELLA, S., 2000, *Phys. Rev. B*, **62**, 12700.

BEDNORZ, J. G., and MÜLLER, K. A., 1986, *Z. Phys. B*, **64**, 189.

BEENEN, J., and EDWARDS, D. M., 1995, *J. Low Temp. Phys.*, **99**, 403; *Phys. Rev. B*, **52**, 13636.

BEREZINSKII, V. L., 1974, *Pisma Zh. Eksp. Teor. Fiz.*, **20**, 628 [1974, *JETP Lett.*, **20**, 287].

BERK, N. F., and SCHRIEFFER, J. R., 1966, *Phys. Rev. Lett.*, **17**, 433.

BICKERS, N. E., SCALAPINO, D. J., and SCALETTAR, R. T., 1987, *Int. J. Mod. Phys. B*, **1**, 687.

BICKERS, N. E., SCALAPINO, D. J., and WHITE, S. R., 1989, *Phys. Rev. Lett.*, **62**, 961.

BICKERS, N. E., and WHITE, S. R., 1991, *Phys. Rev. B*, **43**, 8044.

BIRGENEAU, R. J., 1990, in *Physical Properties of High Temperature Superconductors II*, edited by D. M. Ginsberg (World Scientific, Singapore).

BLANKENBECLER, R., SCALAPINO, D. J., and SUGAR, R. L., 1981, *Phys. Rev. D*, **24**, 2278.

BONCA, J., GUBERNATIS, J. E., GUERRERO, M., JECKELMANN, E., and WHITE, S. R., 2000, *Phys. Rev. B*, **61**, 3251.

BULUT, N., HONE, D., SCALAPINO, D. J., and BICKERS, N. E., 1990, *Phys. Rev. B*, **41**, 1797.

BULUT, N., 1990, in *Dynamics of Magnetic Fluctuations in High-Temperature Superconductors*, edited by G. Reiter, P. Horsch, and G.C. Psaltakis (Plenum).

BULUT, N., and SCALAPINO, D. J., 1991, *Phys. Rev. Lett.*, **67**, 2898.

BULUT, N., and SCALAPINO, D. J., 1992, *Phys. Rev. Lett.*, **68**, 706.

BULUT, N., SCALAPINO, D. J., and WHITE, S. R., 1993, *Phys. Rev. B*, **47**, 2742; *Phys. Rev. B*, **47**, 6157; *Phys. Rev. B*, **47**, 14599.

BULUT, N., SCALAPINO, D. J., and WHITE, S. R., 1994a, *Phys. Rev. Lett.*, **72**, 705; *Phys. Rev. B*, **50**, 7215; *Phys. Rev. Lett.*, **73**, 748.

BULUT, N., SCALAPINO, D. J., and WHITE, S. R., 1994b, *Phys. Rev. B*, **50**, 9623.

BULUT, N., SCALAPINO, D. J., and WHITE, S. R., 1995, *Physica C*, **246**, 85.

BULUT, N., and SCALAPINO, D. J., 1995, *J. Phys. Chem. Solids*, **56**, 1597.

BULUT, N., 1996, *Tr. J. Phys.*, **20**, 548.

BULUT, N., and SCALAPINO, D. J., 1996, *Phys. Rev. B*, **54**, 14971.

CALANDRA, M., BECCA, F., and SORELLA, S., 1998, *Phys. Rev. Lett.*, **81**, 5185.

CHEN, L., BOURBONNAIS, C., LI, T., and TREMBLAY, A.-M. S. 1991, *Phys. Rev. Lett.*, **66**, 369.

CHEN, Y. C., MOREO, A., ORTOLANI, F., DAGOTTO, E., and LEE, T. K., 1994, *Phys. Rev. B*, **50**, 655.

CYROT, M., 1986, *Solid State Commun.*, **60**, 253.

DAGOTTO, E., ORTOLANI, F., and SCALAPINO, D. J., 1991, *Phys. Rev. B*, **46**, 3183; DAGOTTO, E., MOREO, A., ORTOLANI, F., RIERA, J., and SCALAPINO, D. J., 1991, *Phys. Rev. Lett.*, **67**, 1918.

DAGOTTO, E., RIERA, J., and SCALAPINO, D. J., 1992a, *Phys. Rev. B*, **45**, 5744.

DAGOTTO, E., MOREO, A., ORTOLANI, F., POILBLANC, D., and RIERA, J., 1992b, *Phys. Rev. B*, **45**, 10741.

DAGOTTO, E., MOREO, A., ORTOLANI, F., RIERA, J., and SCALAPINO, D. J., 1992c, *Phys. Rev. B*, **45**, 10107.

DAGOTTO, E., 1994, *Rev. Mod. Phys.*, **66**, 763.

DAGOTTO, E., and NAZARENKO, A., and BONINSEGNI, M., 1994, *Phys. Rev. Lett.*, **73**, 728.

DAGOTTO, E., and RICE, T. M., 1996, *Science*, **271**, 618.

DAHM, T., and TEWORDT, L., 1995, *Physica* C, **246**, 61; 1995, *Phys. Rev. B*, **52**, 1297; 1995, *Phys. Rev. Lett.*, **74**, 793.

DAHM, T., and BULUT, N., 1996, unpublished.

DAHM, T., and SCALAPINO, D. J., 1997, *Physica* C, **288**, 33.

DAMASCELLI, A., LU, D. H., and SHEN, Z.-X., 2001, *J. Electron Spectr. Relat. Phenom.*, **117-118**, 165.

DAUL, S., SCALAPINO, D. J., and WHITE, S. R., 2000, *Phys. Rev. Lett.*, **84**, 4188.

DESSAU, D., S., *et al.*, 1993, *Phys. Rev. Lett.*, **71**, 2781.

DING, H. *et al.*, 1996, *Nature*, **382**, 51.

DONIACH, S., and ENGELSBERG, S., 1966, *Phys. Rev. Lett.*, **17**, 750.

DOPF, G., MURAMATSU, A., and HANKE, W., 1992a, *Phys. Rev. Lett.*, **68**, 353.

DOPF, G., WAGNER, J., DIETERICH, P., MURAMATSU, A., and HANKE, W., 1992b, *Phys. Rev. Lett.*, **68**, 2082.

DORNEICH, A., ZACHER, M. G., GRÖBER, C., and EDER, R., 2000, *Phys. Rev. B*, **61**, 12816.

DUFFY, D., and MOREO, A., 1995, *Phys. Rev. B*, **51**, 11882.

DZYALOSHINSKII, I., 1987, *Zh. Eksp. Teor. Fiz.* **93** 1487 [*Sov. Phys. JETP* **66**, 848 (1987)].

EMERY, V. J., 1986, *Synth. Metals*, **13**, 21.

EMERY, V. J., KIVELSON, S. A., and LIN, H. Q., 1990, *Phys. Rev. Lett.*, **64**, 475.

ENDRES, H., NOACK, R. M., HANKE, W., POILBLANC, D., and SCALAPINO, D. J., 1996, *Phys. Rev. B*, **53**, 5530.

FURUKAWA, N., and IMADA, M., 1991, *J. Phys. Soc. Jpn.*, **60**, 3604.

FURUKAWA, N., and IMADA, M., 1992, *J. Phys. Soc. Jpn.*, **61**, 3331.

FURUKAWA, N., RICE, T. M., and SALMHOFER, M., 1998, *Phys. Rev. Lett.*, **81**, 3195.

GEORGES, A., KOTLIAR, G., KRAUTH, W., and ROZENBERG, M.J., 1996, *Rev. Mod. Phys.* **68**, 13.

GOFRON, K., *et al.*, 1993, *J. Phys. Chem. Solids*, **54**, 1193.

GOPALAN, S., RICE, T. M., and SIGRIST, M., 1994, *Phys. Rev. B*, **49**, 8901.

GRÖBER, C., EDER, R., and HANKE, W., 2000, *Phys. Rev. B*, **62**, 4336.

GUERRERO, M., ORTIZ, G., and GUBERNATIS, J. E., 1999, *Phys. Rev. B*, **59**, 1706.

HALBOTH, C. J. and METZNER, W., 2000, *Phys. Rev. B*, **61**, 7364.

HARDY, W. N., BONN, D. A., MORGAN, D. C., LIANG, R., and ZHANG, K., 1993, *Phys. Rev. Lett.* **70**, 3999.

HAAS, S., MOREO, A., and DAGOTTO, E., 1995, *Phys. Rev. Lett.*, **74**, 4281.

HAYWARD, C. A., POILBLANC, D., NOACK, R. M., SCALAPINO, D. J., and HANKE, W., 1995, *Phys. Rev. Lett.*, **75**, 926.

HELLBERG, C. S., and MANOUSAKIS, E., 1997, *Phys. Rev. Lett.*, **78**, 4609.

HELLBERG, C. S., and MANOUSAKIS, E., 1999, *Phys. Rev. Lett.*, **83**, 132.

HELLBERG, C. S., and MANOUSAKIS, E., 2000, *Phys. Rev. B*, **61**, 11787.

HIRSCH, J. E., 1985, *Phys. Rev. Lett.*, **54**, 1317; 1985, *Phys. Rev. B*, **31**, 4403.

HIRSCH, J. E., and TANG, S., 1989, *Phys. Rev. Lett.*, **62**, 591.

HONERKAMP, C. SALMHOFER, M., FURUKAWA, N., and RICE, T.M., 2001, *Phys. Rev. B*, **63**, 035109.

HUBBARD, J., 1963, *Proc. Roy. Soc. A*, **276**, 238.

HUSCROFT, C., JARRELL, M., MAIER, Th., MOUKOURI, S., and TAHVILDARZADEH, A. N., 2001, *Phys. Rev. Lett.*, **86**, 139.

HUSSLEIN, T., MORGENSTERN, I., NEWNS, D. M., PATTNAIK, P. C., SINGER, J. M., and MATUTTIS, H. G., 1996, *Phys. Rev. B*, **54**, 16179.

HYBERTSEN, M. S., STECHEL, E. B., SCHLÜTER, M., and JENNISON, D. R., 1990, *Phys. Rev. B*, **41**, 11068.

IMADA, M., 1991, *J. Phys. Soc. Jpn.*, **60**, 2740.

IMADA, M., and KOHNO, M., 2000, *Phys. Rev. Lett.*, **84**, 143.

IMAI, T., SLICHTER, C. P., YOSHIMURA, K., and KOSUGE, K., 1993, *Phys. Rev. Lett.*, **70**, 1002.

ITOH, Y., YASUOKA, H., FUJIWARA, Y., UEDA, Y., MACHI, T., TOMENO, I., TAI, K., KOSHIZUKA, N., and TANAKA, S., 1992, *J. Phys. Soc. Jpn.*, **61**, 1287.

JAKLIC, J., and PRELOVSEK, P., 2000, *Adv. Phys.*, **49**, 1.

JARRELL, M., 1992, *Phys. Rev. Lett.*, **69**, 168.

JARRELL, M., and GUBERNATIS, J. E., 1996, *Phys. Rep.*, **269**, 134.

JECKELMANN, E., SCALAPINO, D. J., and WHITE, S. R., 1998, *Phys. Rev. B*, **58**, 9492.

KAMPF, A. P., and SCHRIEFFER, J. R., 1990a, *Phys. Rev. B*, **41**, 6399.

KAMPF, A. P., and SCHRIEFFER, J. R., 1990b, *Phys. Rev. B*, **42**, 7967.

KANAMORI, J., 1963, *Prog. Theor. Phys.*, **30**, 275.

KIVELSON, S. A., ROKHSAR, D. S., and SETHNA, J. P., 1987, *Phys. Rev. B*, **35**, 8865.

KOIKE, S., YAMAJI, K., and YANAGISAWA, T., 2000, *Physica B*, **284**, 417.

LEDERER, P. MONTHAMBAUX, G., and POILBLANC, D., 1987, *J. Phys.* **48**, 1613.

LEGGETT, A., J., 1975, *Rev. Mod. Phys.*, **47**, 331.

LIU, Z., and MANOUSAKIS, E., 1992, *Phys. Rev. B*, **44**, 2414.

LOH, E. Y, GUBERNATIS, J. E., SCALETTAR, R. T., WHITE, S. R., SCALAPINO, D. J., and SUGAR, R. L., 1990, *Phys. Rev.*, B, **41**, 9301.

LUO, J., and BICKERS, N. E., 1993, *Phys. Rev. B*, **47**, 12153.

M$^2$S-HTSC VI, 2000, *Proceedings of the International Conference on Materials and Mechanisms of Superconductivity and High Temperature Superconductors*, edited by K. Salama, W.K. Chu and P.W.C. Chu, *Physica C*, **341-348**.

MACHIDA, K., 1989, *Physica C*, **158**, 192.

MAHAN, G. D., 1981, "Many-particle Physics", (Plenum, New York).

MAHAJAN, A. V., ALLOUL, H., COLLIN, G., MARUCCO, J. F., 1994, *Phys. Rev. Lett.*, **72**, 3100.

MAHAJAN, A. V., ALLOUL, H., COLLIN, G., MARUCCO, J. F., 2000, *Euro. Phys. J. B*, **13**, 457.

MAIER, Th., JARRELL, M., PRUSCHKE, T., and KELLER, J., 2000, *Phys. Rev. Lett.*, **85**, 1524.

MARTINDALE, J. A., BARRETT, S. E., KLUG, C. A., O'HARA, K. E., DESOTO, S. M., SLICHTER, C. P., FRIEDMAN, T. A., and GINSBERG, D. M., 1992, *Phys. Rev. Lett.*, **68**, 702.

METZNER, W. and VOLLHARDT, D., 1989, *Phys. Rev. Lett.*, **62**, 324.

MILA, F., and RICE, T. M., 1989, *Physica* C, **157**, 561.

MILLIS, A. J., MONIEN, H., and PINES, D., 1990, *Phys. Rev.* B, **42**, 167.

MIYAKE, K., SCHMITT-RINK, S., and VARMA, C. M., 1986, *Phys. Rev.* B, **34**, 6554.

MONTHOUX, P., BALATSKY, A. V., and PINES, D., 1991, *Phys. Rev. Lett.*, **67**, 3448; *Phys. Rev.* B, **46**, 14803.

MONTHOUX, P., and PINES, D., 1992, *Phys. Rev. Lett.*, **69**, 961; *Phys. Rev.* B, **50**, 16015.

MONTHOUX, P., and SCALAPINO, D. J., 1994, *Phys. Rev. Lett.*, **72**, 1874.

MOREO, A., and SCALAPINO, D. J., 1991, *Phys. Rev.* B, **43**, 8211.

MOREO, A., and SCALAPINO, D. J., and DAGOTTO, E., 1991, *Phys. Rev.* B, **43**, 11442.

MOREO, A., 1992, *Phys. Rev.* B, **45**, 5059.

MOREO, A., HAAS, S., SANDVIK, A. W., and DAGOTTO, E., 1995, *Phys. Rev.* B, **51**, 12045.

MORIYA, T., TAKAHASHI, Y., and UEDA, K., 1990, *J. Phys. Soc. Jpn.*, **59**, 2905.

MORIYA, T., and UEDA, K., 2000, *Adv. Phys.*, **49**, 555.

MÜLLER-HARTMANN, E., 1989, *Z. Phys.* B, **74**, 507.

MURAMATSU, A., 1999, in *Quantum Monte Carlo Methods in Physics and Chemistry*, edited by M.P. Nightingale and C.J. Umrigar (Kluwer Academic).

NAKANISHI, T., YAMAJI, K., and YANAGISAWA, T., 1997, *J. Phys. Soc. Jpn.*, **66**, 294.

NEWNS, D. M., TSUEI, C. C., HUEBENER, R. P., VAN BENTUM, P. J. M., PATTNAIK, P. C., and CHI, C. C., 1994, *Phys. Rev. Lett.*, **73**, 1695.

NOACK, R. M., WHITE, S. R., and SCALAPINO, D. J., 1994, *Phys. Rev. Lett.*, **73**, 882.

NOACK, R. M., WHITE, S. R., and SCALAPINO, D. J., 1995, *Europhys. Lett.*, **30**, 163.

NOACK, R. M., WHITE, S. R., and SCALAPINO, D. J., 1996, *Physica* C, **270**, 281.

NOACK, R. M., BULUT, N., SCALAPINO, D. J., and ZACHER, M.G., 1997, *Phys. Rev.* B, **56**, 7162.

PAO, C. H., and BICKERS, N. E., 1994, *Phys. Rev. Lett.*, **72**, 1870.

PAO, C.-H., and BICKERS, N. E., 1995, *Phys. Rev.* B, **51**, 16310.

PENNINGTON, C. H., and SLICHTER, C. P., 1990, in *Physical Properties of High Temperature Superconductors II*, edited by D. M. Ginsberg (World Scientific, Singapore).

PENNINGTON, C. H., and SLICHTER, C. P., 1991 *Phys. Rev. Lett.*, **66**, 381.

POILBLANC, D. and RICE, T. M., 1989, *Phys. Rev.* B, **39**, 9749.

POILBLANC, D., 1993, *Phys. Rev.* B, **48**, 3368; 1994, *Phys. Rev.* B, **49**, 1477.

PREUSS, R., MURAMATSU, A., von der LINDEN, W., DIETRICH, P., ASSAAD, F. F., and HANKE, W., 1994, *Phys. Rev. Lett.*, **73**, 732.

PREUSS, R., HANKE, W., and von der LINDEN, W., 1995, *Phys. Rev. Lett.*, **75**, 1344.

PREUSS, R., HANKE, W., GRÖBER, C., and EVERTZ, H. G., 1997, *Phys. Rev. Lett.*, **79**, 1122.

PRUSCHKE, T., JARRELL, M., and FREERICKS, J. K., 1995, *Adv. Phys.*, **42**, 187.

PUTIKKA, W. O., LUCHINI, M. U., and RICE, T. M., 1992, *Phys. Rev. Lett.*, **68**, 538.

PUTIKKA, W. O., GLENISTER, R. L., SINGH, R. R. P., and TSUNETSUGU, H., 1994, *Phys. Rev. Lett.*, **73**, 170.

ROMMER, S., WHITE, S. R., and SCALAPINO, D. J., 2000, *Phys. Rev.* B, **61**, 13424.

RONNING, F. *et al.*, 1998, *Science*, **282**, 2067.

SCALAPINO, D. J., 1993, in *Proceedings of the Summer School on Modern Perspectives in Many-Body Physics*, Canberra (World Scientific, Singapore).

SCALAPINO, D. J., 1995, *Phys. Rep.*, **250**, 330.

SCALAPINO, D. J., LOH, E. Jr., and HIRSCH, J. E., 1986, *Phys. Rev.* B, **34**, 8190.

SCALAPINO, D. J., WHITE, S. R., and ZHANG, S. C., 1992, *Phys. Rev. Lett.*, **68**, 2830.

SCALAPINO, D. J., WHITE, S. R., and ZHANG, S. C., 1993, *Phys. Rev.* B, **47**, 7995.

SCALETTAR, R. T., SCALAPINO, D. J., SUGAR, R. L., and WHITE, S. R., 1991, *Phys. Rev.* B, **44**, 770.

SCHRIEFFER, J. R., WEN, X. G., and ZHANG, S. C., 1988, *Phys. Rev. Lett.*, **60**, 944.

SCHRIEFFER, J. R., WEN, X. G., and ZHANG, S. C., 1989, *Phys. Rev.* B, **39**, 11663.

SCHRIEFFER, J. R., 1994, *Solid State Commun.*, **92**, 129.

SCHRIEFFER, J. R., 1995, *J. Low Temp. Phys.*, **99**, 397.

SCHULZ, H. J., 1987, *Europhys. Lett.* **4**, 609.

SCHULZ, H. J., 1989, *J. Physique*, **50**, 2833.

SCHULZ, H. J., 1999, *Phys. Rev.* B, **59**, R2471.

SHEN, Z.-X., DESSAU, D. S., WELLS, B. O., KING, D. M., SPEICER, W. E., ARKO, A. J., MARSHALL, D., LOMBARDO, L. W., KAPITULNIK, A., DICKINSON, P., DONIACH, S., DICARLO, J., LOESER, T., and PARK, C. H., 1993, *Phys. Rev. Lett.*, **70**, 1553.

SHEN, Z.-X., and DESSAU, D. S., 1995, *Phys. Rep.*, **253**, 1.

SILVER, R., N., SILVIA, D., S., and GUBERNATIS, J. E., 1990, *Phys. Rev.* B, **41**, 2380.

TAKIGAWA, M., 1990, in *Dynamics of Magnetic Fluctuations in High-Temperature Superconductors*, edited by G. Reiter, P. Horsch, and G.C. Psaltakis (Plenum).

TAKIGAWA, M., SMITH, J. L., and HULTS, W. L., 1991, *Physica* C, **185**, 1105; *Phys. Rev.* B, **44**, 7764.

TRANQUADA, J. M., STERNLIEB, B. J., AXE, J. D., NAKAMURA, Y., and UCHIDA, S., 1995, *Nature*, **375**, 561.

TSUEI, C. C., CHI, C. C., NEWNS, D. M., PATTNAIK, P. C., and DAUMLING, M., 1992, *Phys. Rev. Lett.*, **69**, 2134.

TSUEI, C. C., KIRTLEY, J. R., CHI, C. C., YU-JAHNES, L. S., GUPTA, A., SHAW, T., SUN, J. Z., and KETCHEN, M. B., 1994, *Phys. Rev. Lett.*, **73**, 593.

TSUEI, C. C., and KIRTLEY, 2000, *Rev. Mod. Phys.*, **72**, 969.

VAN HARLINGEN, D., 1995, *Rev. Mod. Phys.*, **67**, 515.

VARMA, C. M., LITTLEWOOD, P. B., SCHMITT-RINK, S., ABRAHAMS, E., and RUCKEN-STEIN, A. E., 1989, *Phys. Rev. Lett.*, **63**, 1996.

VEKIC, M., and WHITE, S. R., 1993, *Phys. Rev.* B, **47**, 1160.

WHITE, S. R., SCALAPINO, D. J., SUGAR, R. L., BICKERS, N. E., and SCALETTAR, R. T., 1989a, *Phys. Rev.* B, **39**, 839.

WHITE, S. R., SCALAPINO, D. J., SUGAR, R. L., LOH, E. Y., GUBERNATIS, J. E., and SCALETTAR, R. T., 1989b, *Phys. Rev.* B, **40**, 506.

WHITE, S. R., SCALAPINO, D. J., SUGAR, R. L., and BICKERS, N. E., 1989c, *Phys. Rev. Lett.*, **63**, 1523.

WHITE, S. R., 1991, *Phys. Rev.* B, **44**, 4670; 1992, *Phys. Rev.* B, **46**, 5678.

WHITE, S. R., 1992, *Phys. Rev. Lett.*, **69**, 2863.

WHITE, S. R., 1993, *Phys. Rev.* B, **48**, 10345.

WHITE, S. R., and NOACK, R. M., 1992, *Phys. Rev. Lett.*, **68**, 3487.

WHITE, S. R., and SCALAPINO, D., 1998a, *Phys. Rev. Lett.*, **80**, 1272; *Phys. Rev. Lett.*, **81**, 3227.

WHITE, S. R., and SCALAPINO, D., 1998b, *Phys. Rev.* B, **57**, 3031.

WHITE, S. R., and SCALAPINO, D., 1999, *Phys. Rev.* B, **60**, 753.

WHITE, S. R., and SCALAPINO, D., 2000, *Phys. Rev.* B, **61**, 6320.

WOLLMAN, D. A., VAN HARLINGEN, D. J., LEE, W. C., GINSBERG, D. M., and LEGGETT, A. J., 1993, *Phys. Rev. Lett.*, **71**, 2134.

XIAO, G., CIEPLAK, M. Z., XIAO, J. Q., CHIEN, C. L., 1990, *Phys. Rev.* B, **42**, 8752.

YAMAJI, K., and SHIMOI, Y., 1994, *Physica* C, **222**, 349.

YAMAJI, K., and YANAGISAWA, T., NAKANISHI, T., and KOIKE, S., 1998, *Physica* C, **340**, 225.

ZAANEN, J., and GUNNARSON, O., 1989, *Phys. Rev.* B, **40**, 7391.

ZACHER, M. G., ARRIGONI, E. HANKE, W., and SCHRIEFFER, J. R., 1998, *Phys. Rev.* B, **57**, 6370.

ZANCHI, D. and SCHULZ, H.J., 2000, *Phys. Rev.* B, **61**, 13609.

ZHANG, S., CARLSON, J., and GUBERNATIS, J. E., 1995, *Phys. Rev. Lett.*, **74**, 3652.

ZHANG, S., CARLSON, J., and GUBERNATIS, J. E., 1997, *Phys. Rev. Lett.*, **78**, 4486.